ABSTRACT

Title of dissertation: DEVELOPMENT OF LINEAR AND NONLINEAR COMPONENTS FOR INTEGRATED OPTICAL SIGNAL PROCESSING

Shuo-Yen Tseng, Doctor of Philosophy, 2006

Dissertation directed by: Professor Julius Goldhar
Department of Electrical and Computer Engineering

Optical processors have potentially a major advantage over electronic processors because of their tremendous bandwidth. Massive parallelism is another inherent advantage of optical processors. However, it is traditionally demonstrated with free space components and seldom used for integrated optical signal processing. In this thesis, we consider spatial domain signal processing in guided wave structures, which brings a new dimension to the existing serial signal processing architecture and takes advantage of the parallelism in optics. A novel class of devices using holograms in multimode channel waveguides is developed in this work.

Linear optical signal processing using multimode waveguide holograms (MWHs) is analyzed. We focus on discrete unitary transformations to take advantage of the discrete nature of modes in multimode waveguides. We prove that arbitrary unitary transformations can be performed using holograms in multimode waveguides. A model using the wide-angle beam propagation method (WA-BPM) is developed to simulate the devices and shows good agreement with the theory. The design princi-

ple of MWH devices is introduced. Based on the design principle, BPM models are used to design several devices including a mode-order converter, a Hadamard transformer, and an optical pattern generator/correlator. Optical pattern generators are fabricated to verify the theory and the model. Also, the bandwidth and fabrication tolerance of MWH devices are also analyzed.

Also, we examine the nonlinear optical switches which allow the integration of MWHs into modern optical communication networks. A simple optical setup using an imaged 2-D phase grating is developed for characterization of the complex third-order nonlinearity $\chi^{(3)}$ to identify suitable nonlinear materials for integrated optical switches. This technique provides a reliable way to characterize $\chi^{(3)}$ as new materials are constantly being developed.

Finally, we demonstrate the concept of optical switching using XPM in segmented semiconductor optical amplifiers (SOA) based on the proven technology of semiconductor waveguides. Segmented SOA switches allow the counter-propagation of control and signal pulses in the switch and avoid the problem of parasitic oscillations encountered in high gain SOA switches. A prototype device is experimentally characterized to demonstrate the concept, and a model is developed to obtain optimal parameters for future devices.

DEVELOPMENT OF LINEAR AND NONLINEAR COMPONENTS FOR INTEGRATED OPTICAL SIGNAL PROCESSING

by

Shuo-Yen Tseng

Dissertation submitted to the Faculty of the Graduate School of the
University of Maryland, College Park in partial fulfillment
of the requirements for the degree of
Doctor of Philosophy
2006

Advisory Committee:

Professor Julius Goldhar, Chair/Advisor
Dr. Christopher J. K. Richardson/Co-advisor
Professor Christopher Davis
Professor Robert W. Gammon
Professor Thomas E. Murphy

DEDICATION

To my parents.

ACKNOWLEDGMENTS

First of all, I would like to thank my advisor, Professor Julius Goldhar for his guidance and encouragement of my research. I benefited not only from his knowledge but also from his enthusiasm towards research. Not merely an academic advisor to me, his nice personality and the way he treats people also set examples for me to follow. I am extremely lucky to have the chance to work with and learn from him.

I would also like to thank Dr. Chris Richardson. I will never forget the late nights you spent teaching me Labview when I first joined this lab. I am grateful to all the advice you gave me when I needed it. Thank you for your encouragement when I was feeling down.

My advisory committee, Professor Christopher Davis, Professor Robert Gammon, and Professor Thomas Murphy gave me a lot of suggestions. I am very grateful for their comments.

My colleagues in the Laboratory for Physical Sciences also helped me in many ways and enriched my life. I would like to thank Dr. Warren Herman and Professor Chi Lee for giving me the opportunity to work on nonlinear polymer characterization. I was able to gain a lot of experience and knowledge from working on this project and discussing it with them. I would like to thank Younggu Kim for fabricating the MWH devices and sharing his knowledge in fabrication and CAD design. I couldn't have asked for a better friend. Dr. Paul Petruzzi and Dr. Ehab Awad

helped me operate the equipment in the lab, and I benefited a great deal from their past work. Dyan Ali, Charlie Camp, and Lenin Jacome paved the way for device mounting. I was fortunate to be able to build my work upon their excellent efforts. Without Arun Mampazhy's long and hard working hours in the cleanroom, I would not have the SOAs for experiments. Dr. Yongzhang Leng and Victor Yun gave me a lot of useful advice and help both in work and life. Yi-Hsing Peng helped me a lot in the nonlinear polymer measurements, and I enjoyed the discussions with him. I also benefited from Dr. Weilou Cao's experience in experimental techniques. Dr. Kuldeep Amarnath shared his MatLab code for photomask design, which helped me start off the MWH design. Lisa Lucas helped me with wire bonding and made the 2-D grating for nonlinearity characterization. Greg Latini and Mark Thornton rescued the data from my computer. Without their help, it could have been a disaster. Ricardo Pizarro helped my with the solder dispenser and taught me to play tennis. I would also like to thank Glenn Hutchinson for being a great friend, and I met a lots of wonderful people through him.

My parents and sister are always supportive. I wouldn't be able to finish this thesis without their encouragement. Finally, I would like to thank Ping Sung for her support and encouragement.

TABLE OF CONTENTS

LIST OF TABLES

LIST OF FIGURES

Chapter 1

Introduction

1.1 Motivation

One major reason for considering optical signal processing is its bandwidth (speed) advantage over electronic processors. With the increase in the transmission speed in modern optical communication systems, the application of optical signal processing in optical communication systems has been an active area of research. An important class of operation involves efficient processing of optical patterns consisting of multiple bits (words). The ability to process optical patterns allows the realization of optical pattern recognition, and more general tasks such as matrix-vector multiplication. Matrix transformations such as the discrete Fourier, the Hadamard, and the Haar transformations are useful for spatial signal processing such as spectrum analyzing, filtering, coding and so on [1][2].

In optical communications, the signals are generally transmitted serially using guiding structures in the form of amplitude or phase encoded bits. Most of the current effort in optical pattern processing uses linear or nonlinear effects in single mode waveguide structures. A common approach for high speed processing is the time domain bit by bit logical operation using nonlinear optical gates [3] just like in electronic processors. Another approach for optical pattern recognition is the cross-correlation technique [4]-[8], using either a nonlinear holographic medium [4][5],

nonlinearity in semiconductor optical amplifiers [7][8], or linear delay line matched filters [6] to perform cross-correlation. However, the serial computation approach is inefficient when more complicated processing such as matrix-vector multiplication is needed.

The inefficiency of the serial computation approach for matrix-vector multiplication is illustrated by the following example. Matrix-vector multiplication can be viewed as multiple cross-correlations in which a vector is cross-correlated with the individual rows of a matrix. Consider multiplication of 8-bit words at 160 Gb/s (the word rate is thus 160/8=20 G/s) with an 8×8 matrix as an example, which involves 56 additions for calculating the 8 dot products using electronic processors. This would require a processor speed of 56×20 G = 1.12 T calculations per second. Even for 4-bit words, the electronic processor speed has to exceed 480 G calculations per second. Modern desktop computers typically run at a clock rate of 2 GHz. Only super computers consisting of multiple parallel processors or dedicated processing chips using parallel architecture can deliver the required processing, which leads us to explore the possibility of parallel optical signal processing using integrated optics.

1.2 Parallel processing using linear optics

In addition to speed, another advantage of optical signal processing is its massive parallelism (connectivity). With parallelism, it is possible to complete complicated computations in a single operation. For example, in image processing, an entire image can be processed all at once using optical systems, instead of sequential

processing of each pixel. This advantage is well known and has been explored mainly in the spatial domain signal processing, leading to the development of holography, spatial light modulators, optical neural networks, and many other interesting applications [1][2]. Traditionally, spatial domain optical signal processing is performed using free space optics [9][10], which involves bulky optics in contrast to the small guided wave components used in optical communications. As a result, parallelism is rarely utilized in guided wave optical signal processing. Until recently, little effort has gone into spatial domain signal processing in guided wave structures [11][12]. In this thesis, we consider spatial domain signal processing in guided wave structures, which brings a new dimension to the existing serial signal processing architecture and takes advantage of the parallelism in optics.

1.3 Nonlinear optical processing

There is a limit to the types of operations that can be performed with linear transformations. For many applications, we would also like to be able to implement Boolean algebra, thresholding, and gating functions, which require nonlinear optics. The thresholding function enables the digitization of signals. The gating function allows serial to parallel conversion of optical signals as explained in section 1.6. These applications have been demonstrated using nonlinearity in fibers and semiconductor waveguides [15][16] or using spectral holography with nonlinear optics [17].

The general requirement for these nonlinear operations is for the light to acquire a π phase shift in the processor. For integrated optical processors, strong

nonlinearities are required at short waveguides in order to obtain π phase shift. The development of semiconductor optical amplifier (SOA) [18] technology enables the realization of various integrated nonlinear optical processors. The main drawback of a SOA based switch is that extra power is required to maintain gain in the waveguides. No extra power would be required for materials with a sufficiently large third order nonlinearity, $\chi^{(3)}$ [19]. One class of promising materials for integrated nonlinear processors is nonlinear polymers with a fast refractive index nonlinearity. Unfortunately, we have no suitable nonlinear polymers for practical implementation at present. Instead, the focus is on characterizing the nonlinearity of new materials as they are constantly being developed through DARPA's super molecular photonics (MORPH) program. Also, new semiconductor materials grown by the molecular beam epitaxy (MBE) facility in the Laboratory for Physical Sciences are being tested.

1.4 Scope of this thesis

In order to utilize the parallelism of optics for signal processing in guided wave structures, it is natural to consider multimode waveguides. In chapter 2, linear optical signal processing using multimode waveguide holograms (MWHs) [13][14] is analyzed. The MWH consists of a multimode channel waveguide with a surface relief hologram fabricated on top on the waveguide. We focus on discrete unitary transformations to take advantage of the discrete nature of modes in multimode waveguides. We prove that arbitrary unitary transformations can be performed

using holograms in multimode waveguides. Different functionalities are explored, and the limitations of this class of devices are analyzed in chapter 3.

Also, we examine the nonlinear optical switches which allow the integration of MWHs into modern optical communication networks. We consider a simple switch configuration using cross-phase modulation (XPM) [20] in nonlinear waveguides. For integrated optics, strong nonlinearities are required in the waveguides. In chapter 4, a simple optical setup using an imaged 2-D phase grating [21] is developed for characterization of the complex third-order nonlinearity $\chi^{(3)}$ to identify suitable nonlinear materials for integrated optical switches. A nonlinear polymer is characterized using this technique.

Finally, we demonstrate the concept of optical switching using XPM in segmented semiconductor optical amplifiers (SOA) based on the proven technology of semiconductor waveguides in chapter 5. A prototype device is experimentally characterized to demonstrate the concept, and a model is developed to obtain optimal parameters for future devices.

The subsequent sections provide a brief review of past work relating to this thesis.

1.5 Discrete spatial optical signal processing in multimode waveguides using linear optics

We focus on processing of optical patterns using integrated optics. A particular important class of operation that includes correlation, discrete Fourier transforms

and Hadamard transforms involves multiplication of vectors by unitary matrices. Many of these operations have been demonstrated with coherent spatial signals using conventional free space holography, and this technology is described in various texts [1]-[10], [22]. Planar holographic techniques using slab waveguides combine both the advantages of traditional holography and integrated optics [23]. In this thesis, we develop the theory necessary for designing holograms within guided mode structures to create compact devices that perform unitary operations.

The discrete Fourier and the Hadamard transforms have been proposed using single-mode star networks [24] [25] as shown in Fig. 1.1 or multimode interference (MMI) waveguides [26]. Also, it has been shown that arbitrary unitary operation can be realized with combinations of beam splitters, phase shifters, and mirrors [27]. The holographic approach is another versatile technique for implementation of different transformations which can be readily implemented using integrated optics. Linear transformations using a holographic matrix-vector multiplier incorporating a slab waveguide with integrated 2-D lenses has been demonstrated in photorefractive waveguides under the assumption of undepleted inputs as shown in Fig. 1.2 [28].

In this thesis, we develop the theory for MWHs, which is described in chapter 2. By implementing holograms in a multimode channel waveguide, we take advantage of the discrete nature of the modes for efficient realization of discrete mathematical operations. Modeling, fabrication, and analysis of MWHs are presented in chapter 3. Unlike the previously described approach [28], our method does not require waveguide lenses and couples all of the input optical power to the output.

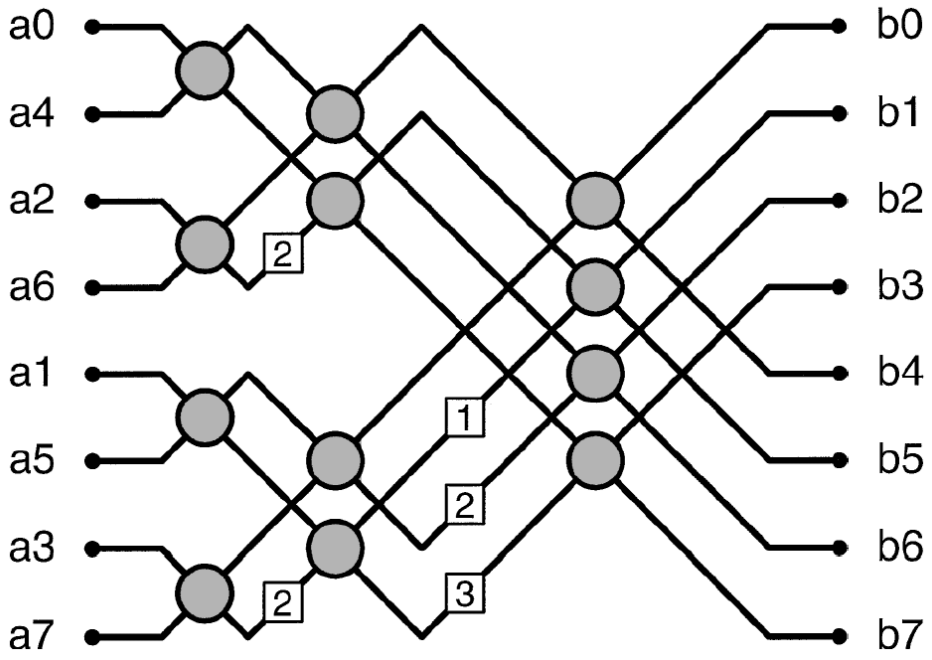

Figure 1.1: Star network that performs an eighth-order discrete Fourier transform. The circles represent 3 dB couplers; the boxes represent added phase shifts of value $-q2\pi/N$, where q is the integer shown in the box [25].

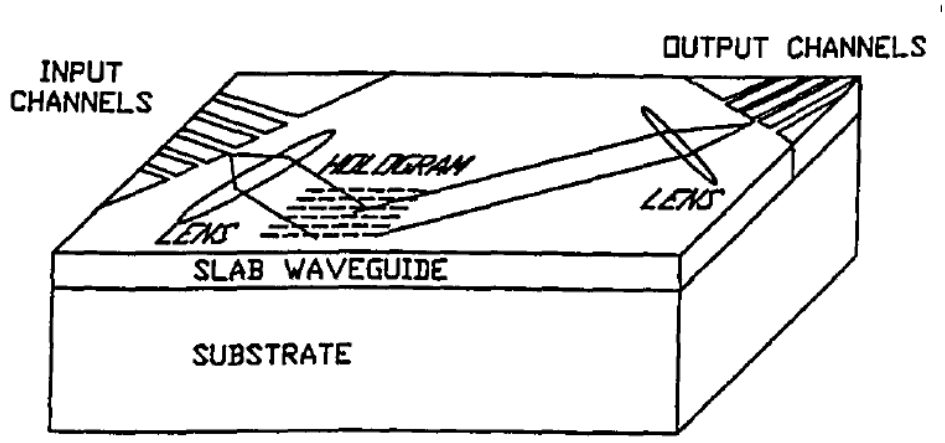

Figure 1.2: Architecture for a holographic integrated optical vector-matrix multiplier [28].

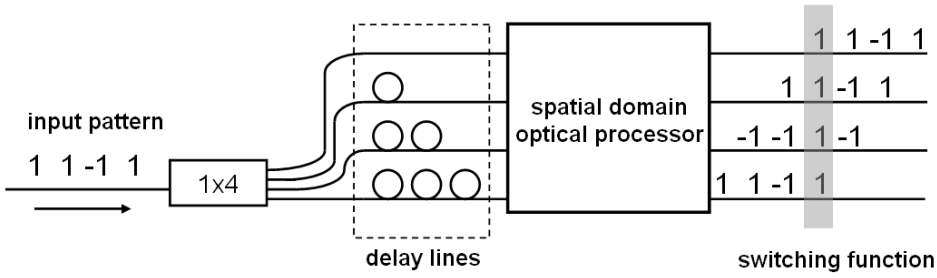

Figure 1.3: Schematic of an optical processor with serial to parallel conversion using splitter, delay lines, and fast optical switch.

1.6 Nonlinear optical switches using cross-phase modulation (XPM) in nonlinear waveguides

The parallel processing architecture considered in this thesis are different from the common serial architectures used in modern optical communication system. In order to utilize the spatial domain processors in traditional serial architectures, serial to parallel conversion and nonlinear switching functions are also needed [17]. A straightforward way of implementing serial to parallel conversion using splitter and delay lines is illustrated in Fig. 1.3. In this architecture, optical switches are needed to select the processed pulses for further optical or electrical processing.

A simple configuration to perform all optical switching is to use cross-phase modulation (XPM) [20] in nonlinear waveguide (NLWG) followed by a filter as illustrated in Fig. 1.4. The equations for pulse propagation in nonlinear waveguide are derived in chapter 5. It will be shown that the nonlinearity in refractive index is responsible for the switching function. In this thesis, we describe a simple method to identify materials for the NLWG and explore all optical switching using a segmented

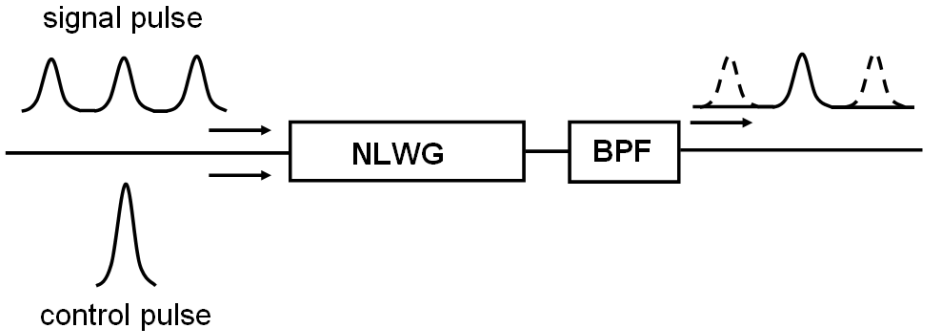

Figure 1.4: Schematic of an optical switch using XPM and optical filtering. NLWG: nonlinear waveguide.

semiconductor optical amplifier (SOA) as the NLWG.

1.6.1 Study of materials for ultrafast nonlinear switches

The requirement on the nonlinear switches is that the response has to be fast enough for operation in modern optical communication systems (typically < 10 ps). The ultrafast refractive nonlinearity in optical fibers has been used as the NLWG in Fig. 1.4 to demonstrate all optical demultiplexing [29] [30]. In these approaches, the signal spectrum is broadened by the pump induced frequency shift via XPM and then selected by appropriate filters. The main drawbacks of these schemes is that relatively long fibers are required. For example, 3.4 km of fiber was used in ref. [29], and 5 km of fiber was used in ref. [30]. Recently, 80 Gb/s demultiplexing using 2 m of highly nonlinear fiber was reported [31]. Although great length reduction is achieved by the development of highly nonlinear fibers, it is still desirable to perform the switching function using integrated optics.

For an integrated solution, materials with large nonlinear index coefficient need

to be identified. The nonlinear index coefficient, n_2, is proportional to the real part of the third order nonlinearity, $\chi^{(3)}_{1111}$ of materials; the imaginary part of $\chi^{(3)}_{1111}$ causes loss due to two photon absorption and limits the effective distance of the waveguide [20]. Degenerate four-wave mixing (DFWM) [32] is a sensitive technique for studies of the $\chi^{(3)}$ of nonlinear materials. Typically, the measured signal is proportional to $|\chi^{(3)}|^2$, but the phase of $\chi^{(3)}$ is not available. A simple optical arrangement for the measurement of the complex $\chi^{(3)}_{1111}$ [21] using DFWM with an imaged 2-D phase grating is developed and described in chapter 4.

1.6.2 Ultrafast optical switching using XPM in semiconductor optical amplifiers

The gain/loss and index dynamics in a semiconductor optical amplifier (SOA) make it a possible candidate for the NLWG in Fig. 1.4. However, the nature of the nonlinearity in SOAs is different from the ultrafast refractive nonlinearity in fibers. The fast nonlinearity associated with saturation is accompanied by slow relaxation [18] which limits its application in high speed operations. Spectral filtering can be used to mitigate the effect of slow relaxation [33]. A simple scheme [34] for ultrafast optical switching using nonlinearities in semiconductor waveguide has been recently demonstrated using the same configuration as in Fig. 1.4; and it was followed by reports from other groups [35] [36]. Similar to the optical switches based on refractive nonlinearity, this approach also uses a frequency shift induced by transient nonlinear phase shift; and a filter is used to select the signal with frequency shift

and to reject the signal without frequency shift. This technique allows ultrafast gate operation unrestricted by the slow nonlinearity relaxation. However, this technique also presents a number of issues. First of all, high gain is required in the amplifier, which can result in parasitic oscillation in the system. Second, strong control and weak signals co-propagate in the SOA. Their separation requires a very high contrast filter, which is difficult to implement in integrated optics. Also, for many applications that require cascaded gates, it is not desirable to operate at different wavelengths for the control and the signal.

The problem with co-propagating switches can be alleviated with a short loss section and a longer gain section as will be explained in chapter 5. In the same chapter, we describe the theory, modeling, and experiment of ultrafast optical switching using SOAs based on this general scheme. A improved design for using a segmented SOA with a long amplifier section and a short saturable absorber section is proposed. Optical sampling technique is used to test a prototype device for demonstration of the operating principle.

Chapter 2

Theoretical Analysis of Multimode Waveguide Holograms (MWHs)

2.1 Introduction

In this chapter, discrete unitary transformations using computer generated volume holograms in multimode channel waveguides are analyzed. The general case of mode transformations in Fig. 2.1 is considered first. The input can be considered as a linear combination of the waveguide modes. The amplitude of these modes can be expressed in vector form as $\mathbf{A}$. The multimode waveguide with multimode waveguide hologram (MWH) transforms the input mode amplitude vector $\mathbf{A}(0)$ to the output mode amplitude vector $\mathbf{A}(L)$ through the unitary matrix $\mathbf{H}$. We will use coupled mode theory [37] to show that arbitrary unitary mode transformations can be performed on coherent spatial signals using the MWHs.

Next, an architecture for optical matrix-vector multiplication as shown in Fig. 2.2 is discussed, where the amplitudes of light in the access waveguides represent the input and output vectors. In this case, the MWH transforms the input vector $\mathbf{P}(0)$ to the output vector $\mathbf{P}(L)$ through the unitary matrix $\mathbf{U}$. It is shown that arbitrary unitary matrix-vector multipliers can be implemented using MWHs in multimode interference (MMI) devices [38] without the need for waveguide lenses (see Fig. 1.2).

The general design approach of MWHs is discussed, and an intuitive design

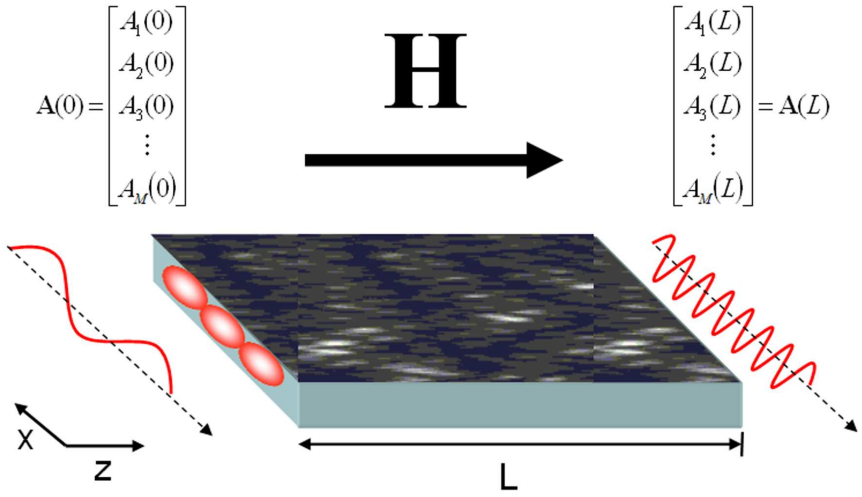

Figure 2.1: Schematic of unitary mode transformer using MWH. $A_i(0)$ and $A_i(L)$ are the amplitudes of the ith mode at the input and output, respectively. **H** is the unitary matrix representing the MWH.

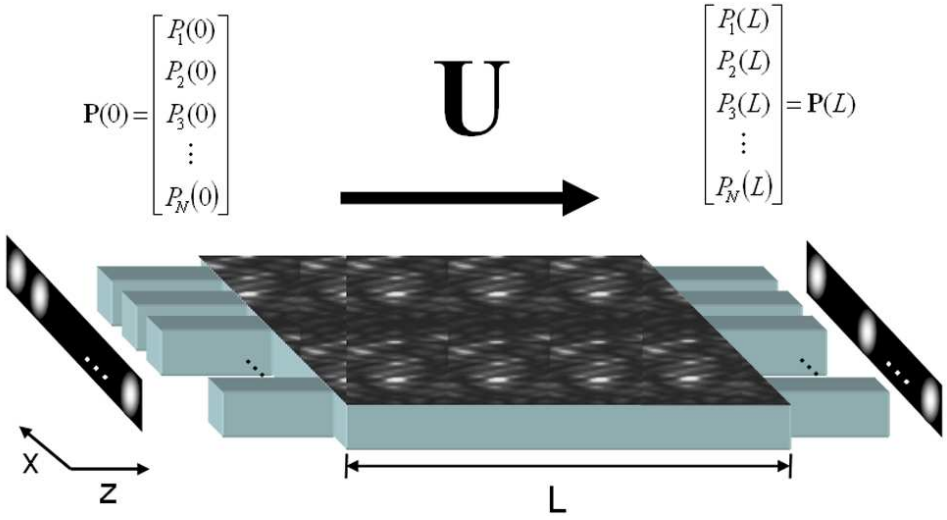

Figure 2.2: Schematic of matrix-vector multiplier using MWH. $P_i(0)$ and $P_i(L)$ are the amplitudes of the ith single mode access waveguide at the input and output, respectively. **U** is the unitary transform matrix of the device.

method for MWHs is outlined. For matrix-vector multipliers at imaging lengths [38] of the MMIs, it is shown that the imaging property of MMIs can be used to simplify the calculation of MWHs to perform the desired transformations. We also mathematically show the equivalency of these two design approaches.

2.2 Wave equation for electric field in optical waveguides

In this section, the fundamental equations describing electromagnetic wave propagation in dielectric optical waveguides are summarized.

The electromagnetic fields inside a optical waveguide satisfy Maxwell's equations: [39]

$$\nabla \times \mathbf{E} = -\mu_0 \frac{\partial \mathbf{H}}{\partial t}, \tag{2.1}$$

$$\nabla \times \mathbf{H} = (\epsilon_0 n^2) \frac{\partial \mathbf{E}}{\partial t}, \tag{2.2}$$

$$\nabla \cdot (\mathbf{H}) = 0, \tag{2.3}$$

$$\nabla \cdot (n^2 \mathbf{E}) = 0, \tag{2.4}$$

where $\mathbf{E}$ is the electric field, $\mathbf{H}$ is the magnetic field, ϵ_0 and μ_0 are the permittivity and permeability of vacuum, and n is the refractive index profile of the waveguide. In the above expressions, we assume that the waveguide has no current source or free charge ($\mathbf{J} = \rho = 0$).

Next, assuming the electromagnetic field oscillates at an angular frequency ω, we obtain the following phasor expressions for $\mathbf{E}$ and $\mathbf{H}$,

$$\mathbf{E}(\mathbf{r}, t) = \mathrm{Re}\{\bar{\mathbf{E}}(\mathbf{r}) \exp(j\omega t)\}, \tag{2.5}$$

$$\mathbf{H}(\mathbf{r},t) = \mathrm{Re}\{\bar{\mathbf{H}}(\mathbf{r})\exp(j\omega t)\}. \tag{2.6}$$

With these expressions, we can rewrite the Maxwell's equations (2.1)-(2.4) in terms of $\bar{\mathbf{E}}$ and $\bar{\mathbf{H}}$ as,

$$\nabla \times \bar{\mathbf{E}} = -j\omega\mu_0\bar{\mathbf{H}}, \tag{2.7}$$

$$\nabla \times \bar{\mathbf{H}} = j\omega(\epsilon_0 n^2)\bar{\mathbf{E}}, \tag{2.8}$$

$$\nabla \cdot (\bar{\mathbf{H}}) = 0, \tag{2.9}$$

$$\nabla \cdot (n^2\bar{\mathbf{E}}) = 0. \tag{2.10}$$

By computing the curl, $\nabla\times$, of (2.7) and using the vector identity, $\nabla \times (\nabla \times \bar{\mathbf{E}}) = \nabla(\nabla \cdot \bar{\mathbf{E}}) - \nabla^2\bar{\mathbf{E}}$, we obtain the vectorial wave equation for the electric field, $\bar{\mathbf{E}}$

$$\nabla^2\bar{\mathbf{E}} + \nabla\left(\frac{1}{n^2}\nabla(n^2)\cdot\bar{\mathbf{E}}\right) + k_0^2 n^2\bar{\mathbf{E}} = 0, \tag{2.11}$$

where k_0 is the wave number in vacuum and is related to the speed of light in vacuum, c, as

$$k_0 = \omega\sqrt{\epsilon_0\mu_0} = \frac{\omega}{c}. \tag{2.12}$$

When the index profile n is constant in the medium, or when the spatial variation of n is small over distances of the order of wavelength, the vectorial wave equation (2.11) can be reduced to the wave equation (Helmholtz equation) for $\bar{\mathbf{E}}$,

$$\nabla^2\bar{\mathbf{E}} + k_0^2 n^2\bar{\mathbf{E}} = 0. \tag{2.13}$$

This approximate form of the wave equation is used throughout the analysis in this thesis.

2.3 Waveguide modes

Now, we consider a waveguide whose structure is uniform in the z direction. Assuming the electric field has a particular polarization, say parallel to x, we can write,

$$\bar{\mathbf{E}} = \hat{\mathbf{x}}\phi(x, y)\exp(-j\beta z), \tag{2.14}$$

where β is the propagation constant to be determined. The exponential factor $\exp(-j\beta z)$ contains all the z dependence, so that $\phi(x, y)$ is z-independent. Substituting (2.14) into (2.13), we obtain,

$$\nabla_\perp^2\phi + (k_0^2 n^2 - \beta^2)\phi = 0, \tag{2.15}$$

where $\nabla_\perp^2$ is the Laplacian in the lateral directions and is expressed as

$$\nabla_\perp^2 = \frac{\partial^2}{\partial x^2} + \frac{\partial^2}{\partial y^2}. \tag{2.16}$$

The solutions to the eigenvalue equation (2.15) are the modes of the multimode waveguide, and the propagation constant, β can be calculated from the eigenvalue. The waveguide supports a finite number of guided modes, and the unconfined radiation modes are not considered in the subsequent analysis.

2.4 Two-dimensional representation of the multimode waveguides

The multimode waveguides considered in this thesis (refer to Fig. 2.1 and 2.2) are single-moded in the y direction, and the x dimensions are much larger than the y dimensions. It is justified to assume that the modes have the same y-axis behavior everywhere in the waveguides [38]. A 2-D representation is used to analyze the

multimode waveguides hereafter. The 2-D representation can obtained from the 3-D multimode waveguide by several methods. The effective index method (Appendix A) is used in our analysis.

In the 2-D representation, the guided modes $\phi(x)$'s are the solutions to the eigenvalue equation (2.15) with $(\partial/\partial y) = 0$. The scalar electric field in a M-mode multimode waveguide can thus be written as a superposition of the guided modes as

$$E(x, z, t) = \sum_{1}^{M} a_m \phi_m(x) \exp(-j\beta_m z + j\omega t), \tag{2.17}$$

where a_m represents the amplitude corresponding to the mth guided mode, and ω is the optical frequency. The guided modes are normalized with the following condition [37],

$$\int_{-\infty}^{+\infty} \phi_m \phi_n \mathrm{d}x = \frac{2\omega\mu}{|\beta_m|}\delta_{mn}, \tag{2.18}$$

such that the power carried by the mth mode is represented by $|a_m|^2$.

Consider a step index multimode waveguide of width W_m, ridge (effective) refractive index n_r , and cladding (effective) refractive index n_c as shown in Fig. 2.3. The waveguide supports M lateral modes with mode numbers $m = 1, 2, \cdots, M$ at wavelength λ. The lateral wavenumber k_m and the propagation constant β_m are related by the dispersion relation,

$$k_m^2 + \beta_m^2 = k_0^2 n_r^2, \tag{2.19}$$

with

$$k_0 = \frac{2\pi}{\lambda} \tag{2.20}$$

$$k_m = \frac{m\pi}{W_e}. \tag{2.21}$$

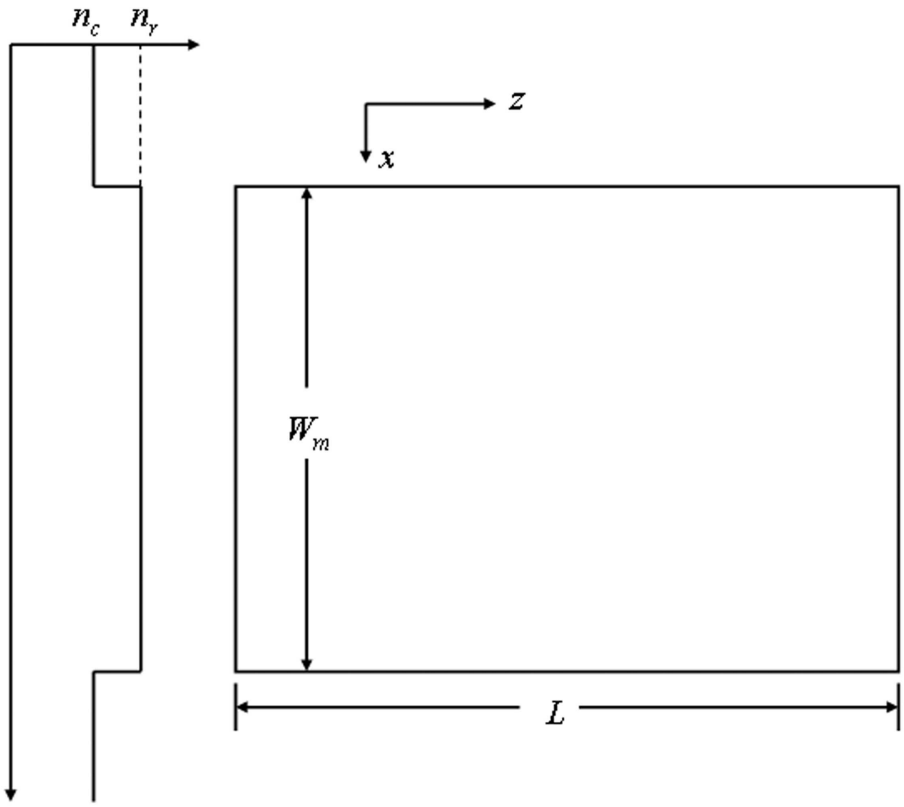

Figure 2.3: 2-D representation of a step-index multimode waveguide.

The approximation here is that the effective width W_e is the same for all the guided modes, which essentially treats the multimode waveguide as a planar-mirror waveguide [40]. This approximation is only used for explanation of the Talbot [41] or self-imaging effect described in the next section, and is not used for the hologram design described in the later sections.

The effective width W_e takes into account the lateral penetration depth of mode fields associated with the Goos-Hähnchen shifts at the boundaries. For high index contrast waveguides (after the effective index method is applied), the penetration depth is very small so that $W_e \simeq W_m$. The propagation constants β_m can

be calculated from (2.19)-(2.21),

$$\beta_m \simeq k_0 n_r - \frac{m^2 \pi \lambda}{4 n_r W_e^2}. \tag{2.22}$$

The propagation constants in a step-index multimode waveguide show a quadratic dependence with respect to the mode number m. We define L_π as the beat length between the fundamental and first-order modes and obtain,

$$L_\pi = \frac{\pi}{\beta_1 - \beta_2} \simeq \frac{4 n_r W_e^2}{3\lambda}. \tag{2.23}$$

The propagation constant spacing can be written as

$$(\beta_1 - \beta_m) \simeq \frac{(m-1)(m+1)\pi}{3 L_\pi}. \tag{2.24}$$

2.5 Self-imaging properties of multi-mode interference (MMI) devices

The multimode interference device consists of a central section of multimode waveguide to support a large number of modes, with single mode access waveguides attached at the input and output planes to couple light in and out of the device as shown in Fig. 2.4.

Consider an input field $\Psi(x, 0)$ at the input of the multimode waveguide, it can be decomposed into the guided modes as

$$\Psi(x, 0) = \sum_{1}^{M} a_m \phi_m(x), \tag{2.25}$$

where the excitation coefficients a_m can be evaluated by

$$a_m = \frac{\int \Psi(x, 0) \phi_m(x) \mathrm{d}x}{\sqrt{\phi_m^2(x) \mathrm{d}x}}. \tag{2.26}$$

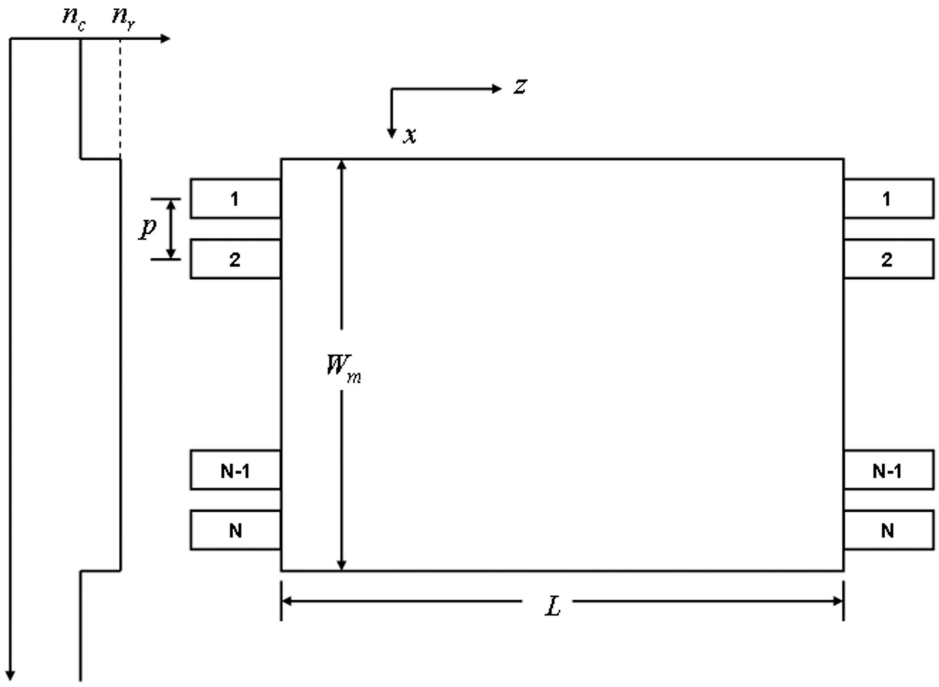

Figure 2.4: Schematics of a $N \times N$ MMI coupler.

The field at position z can thus be written as

$$\Psi(x, z, t) = \sum_{1}^{M} a_m \phi_m(x) \exp(-j\beta_m z + j\omega t). \tag{2.27}$$

Factoring out the phase of the fundamental mode and ignoring the time dependence $i\omega t$, the field becomes,

$$\Psi(x, z, t) = \sum_{1}^{M} a_m \phi_m(x) \exp[j(\beta_1 - \beta_m)z]. \tag{2.28}$$

At distance $z = L$, the following expression is obtained by substituting (2.24) into (2.28),

$$\Psi(x, z, t) = \sum_{1}^{M} a_m \phi_m(x) \exp\left[j\frac{(m-1)(m+1)\pi}{3L_\pi}L\right]. \tag{2.29}$$

Before imaging properties of MMI are analyzed, two useful properties are given

here:

$$(m-1)(m+1) = \begin{cases} \text{even for } m \text{ odd} \\ \\ \text{odd for } m \text{ even} \end{cases}, \tag{2.30}$$

$$\phi_m(-x) = \begin{cases} \phi_m(x) & \text{for } m \text{ odd} \\ \\ -\phi_m(x) & \text{for } m \text{ even} \end{cases}. \tag{2.31}$$

Equation (2.29) shows that the field at $z = L$ will be an image of the input field if

$$\exp\left[j\frac{(m-1)(m+1)\pi}{3L_\pi}L\right] = 1 \quad \text{or} \quad (-1)^m. \tag{2.32}$$

The first condition produces a direct replica of the input field [41]. Using relation (2.31), the second condition produces a mirror image of the input field with respect to $x = 0$. The conditions in (2.32) are fulfilled when

$$L = p(3L_\pi) \quad \text{with} \quad p = 0, 1, 2, \cdots \tag{2.33}$$

for p even (direct image) and p odd (mirror image), respectively.

From the analysis above, it can be seen that by designing the multimode waveguide section of MMI at specific imaging lengths, the direct or mirror image of the input electric field can be replicated at the output. Detailed analysis can be used to show that multiple images can also be obtained at distances other than the single image lengths with specific splitting ratios and phase relations [42]. As a result, MMI devices have found broad applications in beam splitters and couplers [43] [44].

The self-imaging effect comes from the quadratic dependence of the propagation constant to the mode number as approximated by (2.22). For the devices

simulated and fabricated in the subsequent sections of this thesis, we calculated the propagation constants of the guided modes of the full 3-D waveguide structure using a full-vectorial finite difference optical mode solver [45] and found excellent agreement with the approximation.

2.6 Unitary mode transformations using MWHs

The formalisms introduced in the preceding sections are used to develop the theory for multimode waveguide holograms (MWHs) in the remainder of this chapter.

The propagation of the electric field in an M-mode multimode channel waveguide with imbedded MWH in Fig. 2.1 is considered. The hologram is implemented as a weak perturbation to the effective index of refraction n_c of the core of the multimode waveguide. The electric field in the perturbed multimode waveguide can be written using the superposition of the unperturbed waveguide modes as

$$E(x,z,t) = \sum_{1}^{M} A_i(z)\phi_i(x)\exp(-j\beta_i z + j\omega t), \tag{2.34}$$

where A_i represents the amplitude. The hologram is chosen to be of the following form

$$\Delta n(x,z) = f_0(x) + \sum_{i\neq j} f_{ij}(x)\exp[-j(\beta_i - \beta_j)z]. \tag{2.35}$$

The first term adds different phase shifts to the modes depending on their overlap integrals, and the second term represents phase gratings that couple the modes. Each term of the series has an arbitrary amplitude profile and a phase that follows the beating between modes. For the index perturbation to be a real function (energy

conservation) and physically realizable, we also require f_0 to be a real function and $f_{ij} = (f_{ji})^*$. The coupled mode theory involves substituting (2.34)-(2.35) into the wave equation (2.15) and collecting the synchronous terms to obtain the following set of M coupled equations:

$$\frac{\mathrm{d}A_i}{\mathrm{d}z} = -j \sum \kappa_{ij} A_{ij}, \tag{2.36}$$

where the coupling coefficients are given by

$$\kappa_{ii} = \frac{\omega \epsilon_0 n_c}{2} \int f_0(x) \phi_i^2 \mathrm{d}x; \tag{2.37}$$

$$\kappa_{ij} = \frac{\omega \epsilon_0 n_c}{2} \int f_{ij}(x) \phi_i \phi_j \mathrm{d}x \quad (i \neq j). \tag{2.38}$$

The coupled mode equations in (2.36) can be expressed in matrix form as

$$\frac{\mathrm{d}\mathbf{A}}{\mathrm{d}z} = -j\mathbf{K}\mathbf{A}, \tag{2.39}$$

where the ith row and jth column of the $M \times M$ matrix $\mathbf{K}$ is κ_{ij}, and $\mathbf{A} = [A_1(z)A_2(z)...A_M(z)]^T$. The solution to (2.39) is

$$\mathbf{A}(z) = \exp(-j\mathbf{K}z)\mathbf{A}(0) = \mathbf{H}(z)\mathbf{A}(0). \tag{2.40}$$

The requirements imposed on f_0 and f_{ij} makes $\mathbf{K}$ an Hermitian matrix, that is $\mathbf{K}^\dagger = \mathbf{K}$. As a result, $\mathbf{H} = \exp(-j\mathbf{K}z)$ is a $M \times M$ unitary matrix. The operation in Fig. 2.1 can thus be described as a unitary matrix $\mathbf{H}$ transforming the input mode amplitude vector $\mathbf{A}(0)$ to the output mode amplitude vector $\mathbf{A}(L)$. Since each component of $\mathbf{K}$ corresponds to an independent grating, changing the shape and strength of the hologram through f_0 and f_{ij} allows us to generate arbitrary

unitary matrices. One specific approach for calculating f_0 and f_{ij} will be described in section 2.8.

The derivations above assume energy conservation in the waveguide (real index perturbation). Non-unitary transformations can be implemented by introducing either gain/loss or additional channels in the waveguide. It is beyond the scope of this thesis to analyze the non-unitary transformations, rather we focus on the analysis and design of arbitrary unitary transformations using MWHs.

2.7 Unitary matrix-vector multiplication using MWHs

Consider the matrix-vector multiplier using MWHs in Fig. 2.2. N symmetric single mode input and output waveguides are attached to the M-mode multimode waveguide of length L. This is similar to an $N \times N$ multimode interference (MMI) coupler except that the device incorporates a hologram and the self-imaging property is not required for the device to function.

The input and output vectors are represented by the amplitudes of the input and the output waveguides. First consider the multimode waveguide behavior of the device without the hologram. The fields at the input and the output waveguides can be decomposed into the guided modes of the multimode section as in (2.25). Since (2.25) can be interpreted as a discrete spatial Fourier transform [38] of the input/output vectors, the amplitudes of the waveguides $\mathbf{P}(0) = [P_1(0)P_2(0)...P_N(0)]^T$ and output waveguides $\mathbf{P}(L) = [P_1(L)P_2(L)...P_N(L)]^T$ can be related in matrix form

as

$$\mathbf{P}(L) = (\mathbf{V}\mathbf{B}\mathbf{V}^T)\mathbf{P}(0), \tag{2.41}$$

where

$$\mathbf{V}^T = \begin{bmatrix} \exp(-j\beta_1 L) & 0 & \cdots & 0 \\ 0 & \exp(-j\beta_2 L) & \cdots & 0 \\ \vdots & \vdots & \ddots & \vdots \\ 0 & 0 & \cdots & \exp(-j\beta_M L) \end{bmatrix}. \tag{2.42}$$

$\mathbf{B}$ is a $M \times M$ diagonal unitary matrix that describes the phase change resulting from the propagation of a distance of L of each guided mode, and $\mathbf{V}$ is a $M \times M$ unitary matrix that relates the vectors $\mathbf{P}$ at the input and output waveguides to mode amplitudes vectors. When the number of modes M in the multimode section is greater than the number of access waveguides N, the expressions for $\mathbf{P}(0)$ and $\mathbf{P}(L)$ can be zero padded to account for the "virtual" waveguides.

When a hologram is incorporated into the multimode waveguide, equation (2.41) is combined with (2.40) which describes the unitary mode transformation in Fig. 2.1 to yield,

$$\mathbf{P}(L) = (\mathbf{V}\mathbf{B}\mathbf{H}\mathbf{V}^T)\mathbf{P}(0) = \mathbf{U}\mathbf{P}(0). \tag{2.43}$$

This is a vector-matrix multiplication mapping an input vector $\mathbf{P}(0)$ to an output vector $\mathbf{P}(L)$ through a unitary matrix $\mathbf{U}$ determined by the MWH. To generate an arbitrary $\mathbf{U}$, $\mathbf{H}$ is found by

$$\mathbf{H} = \mathbf{B}^T\mathbf{V}^T\mathbf{U}\mathbf{V}. \tag{2.44}$$

2.8 Design of MWHs

From the previous derivations, the calculation of MWHs to perform the desired transformations involves determining the grating shapes, strengths, and periods in (2.35) such that the resulting MWH gives the desired matrix **H** in (2.40) for unitary mode transformation and in (2.44) for matrix-vector multiplication. Here, an intuitive design method in which the gratings are generated by the interference of propagating beams is discussed. This method involves using the interference patterns of the guided modes to calculate individual grating elements in (2.35). A special case of this method to design a matrix-vector multiplier using the imaging property of MMIs is also discussed.

2.8.1 MWHs calculated using the guided modes as the basis sets

By analogy to formation of a hologram by the interference of two waves, we consider the interference of guided modes i and j. The interference pattern that couples mode i and j can be described by

$$\phi_i \phi_j \exp[-j(\beta_i - \beta_j)z] + c.c.. \tag{2.45}$$

When the gratings in the hologram (2.35) are in the form of (2.45), that is, $f_{ij} = g_{ij}\phi_i\phi_j$, the coupling coefficients κ_{ij} are proportional to the grating strengths g_{ij}. By calculating the interference patterns between guided modes, gratings corresponding to each components of **K** in (2.39) are obtained. The hologram can then be determined by simply varying the grating strength according to the required coupling coefficients.

2.8.2 Matrix-vector multipliers calculated using the eigenvectors of MMI (a special case when the multimode waveguide is at imaging length)

The general method outlined in 2.8.1 can be used to design matrix-vector multipliers as long as (2.44) can be satisfied. Self-imaging of multimode waveguide is not essential. However, the design can be simplified when the length of the multimode waveguide is equal to its imaging length.

In section 2.5, we derived the self-imaging property, which describes the reproduction of a single or multiple image of the input field profile at periodic interval along the propagation direction of a multimode waveguide [38]. First of all, by choosing the length of the multimode waveguide to be equal to the self-imaging length L_{img}, the problem can be simplified since the matrix $\mathbf{B}$ in (2.41) becomes the identity matrix. For an $N \times N$ MMI coupler, there are N orthogonal eigenvectors that represent the patterns at input, output, and any intermediate imaging planes [46]. These eigenvectors are obtained by sampling the guided mode profiles corresponding to each access waveguides. Instead of using the M guided modes as a basis set to design the hologram as discussed in 2.8.1, the gratings are calculated directly from the interference patterns between these N eigenvectors. The strengths of these gratings are proportional to the coupling coefficients in the $N \times N$ matrix, $\mathbf{K}$, which now directly relate the amplitudes of the input waveguides $\mathbf{P}(0)$ and output waveguides $\mathbf{P}(L_{img})$ by

$$\mathbf{P}(L_{img}) = \exp(-j\mathbf{K}L_{img})\mathbf{P}(0). \tag{2.46}$$

2.9 Comparison of two different design approaches

Here, we show that by writing the eigenvectors of MMI in the form of the mode amplitude vectors and going through the calculations from (2.41) to (2.44), the hologram calculated using (2.46) is mathematically equivalent to the hologram calculated using the general method in 2.8.1. The advantage of the method in 2.8.2 is its simplicity when the beam propagation method is used to design the hologram as discussed later in the examples in chapter 3.

First, we derive the relation between the eigenmodes and guided modes. From (2.25), we know that the matrix relating the eigenmodes (N basis) to the guided modes (M basis) can be written as

$$\mathbf{V}^T = \begin{bmatrix} a_{11} & a_{21} & \cdots & a_{M1} \\ a_{12} & a_{22} & \cdots & a_{M2} \\ \vdots & \vdots & \ddots & \vdots \\ a_{1M} & a_{2M} & \cdots & a_{MM} \end{bmatrix}. \tag{2.47}$$

Consider the N basis eigenmodes $(\mathbf{e}_N)_i$ and $(\mathbf{e}_N)_j$, in the N basis, they are $N \times 1$ unit vectors with 1's in the ith and the jth elements, respectively. The eigenmodes can be zero padded and be expressed in terms of the guided modes using the M

basis through

$$(\mathbf{e}_M) = \mathbf{V}_T \begin{bmatrix} 0 \\ \vdots \\ (\mathbf{e}_N) \\ \vdots \\ 0 \end{bmatrix}. \tag{2.48}$$

Using (2.47) and (2.48), $(\mathbf{e}_M)_i$ and $(\mathbf{e}_M)_j$ can be obtained

$$(\mathbf{e}_M)_i = \begin{bmatrix} a_{i1} \\ a_{i2} \\ \vdots \\ a_{iM} \end{bmatrix}, \quad (\mathbf{e}_M)_j = \begin{bmatrix} a_{j1} \\ a_{j2} \\ \vdots \\ a_{jM} \end{bmatrix}. \tag{2.49}$$

And the field expressions of these two eigenvectors are

$$\begin{aligned} E_{(\mathbf{e}_M)_i} &= \sum_{k=1}^{M} a_{ik}\phi_k \exp(-j\beta_k z) \\ E_{(\mathbf{e}_M)_j} &= \sum_{k=1}^{M} a_{jk}\phi_k \exp(-j\beta_k z). \end{aligned} \tag{2.50}$$

Now, we calculate the hologram using the eigenmodes first. In the N basis, the $N \times N$ hologram $\mathbf{K}$ calculated using these two eigenmodes is a zero matrix with 1's in the ijth and the jith elements.

$$\mathbf{K} = \begin{bmatrix} 0 & \cdots & \cdots & \cdots & 0 \\ \vdots & \ddots & \ddots & 1 & \vdots \\ \vdots & \ddots & 0 & \ddots & \vdots \\ \vdots & 1 & \ddots & \ddots & \vdots \\ 0 & \cdots & \cdots & \cdots & 0 \end{bmatrix}_{N\times N}. \tag{2.51}$$

With (2.49) and (2.50), we can calculate the same hologram using the guided modes. The interference pattern (hologram) between these two eigenmodes is

$$|E_{(\mathbf{e}_M)_i} + E_{(\mathbf{e}_M)_j}|^2 - |E_{(\mathbf{e}_M)_i}|^2 - |E_{(\mathbf{e}_M)_j}|^2. \tag{2.52}$$

In matrix form, it is

$$\begin{aligned}
\mathbf{H} = &\begin{bmatrix} a_{i1}+a_{j1} & 0 & \cdots & 0 \\ 0 & a_{i2}+a_{j2} & \cdots & 0 \\ \vdots & \vdots & \ddots & \vdots \\ 0 & 0 & \cdots & a_{iM}+a_{jM} \end{bmatrix} \\
&\times \begin{bmatrix} a_{i1}+a_{j1} & a_{i2}+a_{j2} & \cdots & a_{iM}+a_{jM} \\ a_{i1}+a_{j1} & a_{i2}+a_{j2} & \cdots & a_{iM}+a_{jM} \\ \vdots & \vdots & \ddots & \vdots \\ a_{i1}+a_{j1} & a_{i2}+a_{j2} & \cdots & a_{iM}+a_{jM} \end{bmatrix} \\
&- \begin{bmatrix} a_{i1} & 0 & \cdots & 0 \\ 0 & a_{i2} & \cdots & 0 \\ \vdots & \vdots & \ddots & \vdots \\ 0 & 0 & \cdots & a_{iM} \end{bmatrix} \begin{bmatrix} a_{i1} & a_{i2} & \cdots & a_{iM} \\ a_{i1} & a_{i2} & \cdots & a_{iM} \\ \vdots & \vdots & \ddots & \vdots \\ a_{i1} & a_{i2} & \cdots & a_{iM} \end{bmatrix} \\
&- \begin{bmatrix} a_{j1} & 0 & \cdots & 0 \\ 0 & a_{j2} & \cdots & 0 \\ \vdots & \vdots & \ddots & \vdots \\ 0 & 0 & \cdots & a_{jM} \end{bmatrix} \begin{bmatrix} a_{j1} & a_{j2} & \cdots & a_{jM} \\ a_{j1} & a_{j2} & \cdots & a_{jM} \\ \vdots & \vdots & \ddots & \vdots \\ a_{j1} & a_{j2} & \cdots & a_{jM} \end{bmatrix}.
\end{aligned} \tag{2.53}$$

This hologram (M-basis) can be transformed into the basis set of the eigen-

modes (N-basis) by

$$\mathbf{V}\exp(\mathbf{H})\mathbf{V}^T = \exp(\mathbf{V}\mathbf{H}\mathbf{V}^T). \tag{2.54}$$

Now, we calculate $\mathbf{H}\mathbf{V}^T$ first

$$\mathbf{H}\mathbf{V}^T = \begin{bmatrix} a_{i1}+a_{j1} & 0 & \cdots & 0 \\ 0 & a_{i2}+a_{j2} & \cdots & 0 \\ \vdots & \vdots & \ddots & \vdots \\ 0 & 0 & \cdots & a_{iM}+a_{jM} \end{bmatrix}$$

$$\times \begin{bmatrix} 0 & \ldots & 1 & \cdots & 1 & \cdots & 0 \\ 0 & \ldots & 1 & \cdots & 1 & \cdots & 0 \\ \vdots & \vdots & \vdots & \vdots & \vdots & \vdots & \vdots \\ 0 & \ldots & 1 & \cdots & 1 & \cdots & 0 \end{bmatrix}$$

$$- \begin{bmatrix} a_{i1} & 0 & \cdots & 0 \\ 0 & a_{i2} & \cdots & 0 \\ \vdots & \vdots & \ddots & \vdots \\ 0 & 0 & \cdots & a_{iM} \end{bmatrix} \begin{bmatrix} 0 & \ldots & 1 & \cdots & 0 \\ 0 & \ldots & 1 & \cdots & 0 \\ \vdots & \vdots & \vdots & \vdots & \vdots \\ 0 & \ldots & 1 & \cdots & 0 \end{bmatrix}$$

$$- \begin{bmatrix} a_{j1} & 0 & \cdots & 0 \\ 0 & a_{j2} & \cdots & 0 \\ \vdots & \vdots & \ddots & \vdots \\ 0 & 0 & \cdots & a_{jM} \end{bmatrix} \begin{bmatrix} 0 & \ldots & 1 & \cdots & 0 \\ 0 & \ldots & 1 & \cdots & 0 \\ \vdots & \vdots & \vdots & \vdots & \vdots \\ 0 & \ldots & 1 & \cdots & 0 \end{bmatrix}$$

$$
\begin{aligned}
&= \begin{bmatrix}
0 & \dots & a_{i1}+a_{j1} & \cdots & a_{i1}+a_{j1} & \cdots & 0 \\
0 & \dots & a_{i2}+a_{j2} & \cdots & a_{i2}+a_{j2} & \cdots & 0 \\
\vdots & \vdots & \vdots & \vdots & \vdots & \vdots & \vdots \\
0 & \dots & a_{iM}+a_{jM} & \cdots & a_{iM}+a_{jM} & \cdots & 0
\end{bmatrix} \\
&- \begin{bmatrix}
0 & \dots & a_{i1} & \cdots & 0 \\
0 & \dots & a_{i2} & \cdots & 0 \\
\vdots & \vdots & \vdots & \vdots & \vdots \\
0 & \dots & a_{iM} & \cdots & 0
\end{bmatrix} - \begin{bmatrix}
0 & \dots & a_{j1} & \cdots & 0 \\
0 & \dots & a_{j2} & \cdots & 0 \\
\vdots & \vdots & \vdots & \vdots & \vdots \\
0 & \dots & a_{jM} & \cdots & 0
\end{bmatrix} \\
&= \begin{bmatrix}
0 & \dots & a_{j1} & \cdots & a_{i1} & \cdots & 0 \\
0 & \dots & a_{j2} & \cdots & a_{i2} & \cdots & 0 \\
\vdots & \vdots & \vdots & \vdots & \vdots & \vdots & \vdots \\
0 & \dots & a_{jM} & \cdots & a_{iM} & \cdots & 0
\end{bmatrix}.
\end{aligned}
\tag{2.55}
$$

The hologram in terms of the eigenmodes is thus

$$
\mathbf{VHV}^T = \begin{bmatrix}
a_{11} & a_{12} & \cdots & a_{1M} \\
a_{21} & a_{22} & \cdots & a_{2M} \\
\vdots & \vdots & \ddots & \vdots \\
a_{M1} & a_{M1} & \cdots & a_{MM}
\end{bmatrix} \begin{bmatrix}
0 & \dots & a_{j1} & \cdots & a_{i1} & \cdots & 0 \\
0 & \dots & a_{j2} & \cdots & a_{i2} & \cdots & 0 \\
\vdots & \vdots & \vdots & \vdots & \vdots & \vdots & \vdots \\
0 & \dots & a_{jM} & \cdots & a_{iM} & \cdots & 0
\end{bmatrix}
$$

$$
= \begin{bmatrix}
0 & \cdots & & \cdots & & \cdots & 0 \\
\vdots & \ddots & & \ddots & & \ddots & \vdots \\
 & & \begin{bmatrix} 0 & \cdots & \cdots & \cdots & 0 \\ \vdots & \ddots & \ddots & 1 & \vdots \\ \vdots & \ddots & 0 & \ddots & \vdots \\ \vdots & 1 & \ddots & \ddots & \vdots \\ 0 & \cdots & \cdots & \cdots & 0 \end{bmatrix}_{N\times N} & & \\
\vdots & \ddots & & \ddots & & \ddots & \vdots \\
0 & \ddots & & \ddots & & \ddots & 0
\end{bmatrix}_{M\times M}
$$

$$
= \begin{bmatrix}
0 & \cdots & \cdots & \cdots & 0 \\
\vdots & \ddots & \ddots & \ddots & \vdots \\
\vdots & \ddots & \mathbf{K} & \ddots & \vdots \\
\vdots & \ddots & \ddots & \ddots & \vdots \\
0 & \ddots & \ddots & \ddots & 0
\end{bmatrix}_{M\times M} . \quad (2.56)
$$

It is obvious that the hologram is a grating coupling the ith and the jth eigenmodes. Compare (2.56) and (2.51), it can be concluded that the holograms calculated using two methods are mathematically equivalent.

2.10 Discussion

For a specific unitary transformation, the hologram is not unique. The grating shapes and strengths can be adjusted to suit specific design considerations as long as the overlap integrals in (2.37) and (2.38) yield the desired coupling coefficients.

While a set of MWHs can be physically different but mathematically equivalent, one should not expect each member of this set to perform equally. This is because any figure of merit based on physical performance such as tolerance and bandwidth will be based on physical realization of the structure such as waveguide dimension or index contrast. It is beyond the scope of this work to categorize or evaluate the various design approaches that are possible, rather we focus on a specific design approach to demonstrate the concepts of this class of devices in the next chapter.

Chapter 3

Modeling, Fabrication, and Analysis of Multimode Waveguide Holograms (MWHs)

3.1 Introduction

The design principle of MWH devices was introduced in the previous chapter. Based on the design principle, beam propagation models are used to design several devices including a mode-order converter, a Hadamard transformer, and a optical pattern generator/correlator. Optical pattern generators are fabricated to verify the theory and the model. Also, the bandwidth and fabrication tolerance of MWH devices are also analyzed using a specific design example.

From the previous chapter, the design of MWHs involves the calculation of the interference patterns between either the guided modes of the multimode waveguides or the eigenmodes of the MMI couplers. In order to verify the hologram design, we have to model the propagation of beams in the MWH devices. Waveguides with nonuniform structures such as the MWH devices cannot be treated with analytical methods. For our simulations, we choose the beam propagation method (BPM), which has been developed for the analysis of nonuniform structures as bends, tapers, and crosses in the beam propagation direction.

The finite difference beam propagation method (FD-BPM) has been shown

to be accurate, computationally efficient, and stable compared to the conventional fast fourier transform beam propagation method (FFT-BPM) [47]. A multi-step wide-angle scheme developed by Hadley [48] [49] described in the next section is used for our simulations.

3.2 Finite difference wide-angle beam propagation method (WA-BPM)

Here, we use the slowly varying amplitude approximation to obtain an approximate form of Helmholtz equation for the beam propagation simulation [39].

The scalar Helmholtz equation is

$$\nabla^2\Psi + k_0^2 n^2 \Psi = 0. \tag{3.1}$$

In the slowly varying envelop approximation, the wave function of the light Ψ propagating in the $+z$ direction is separated into the slowly varying envelope function ϕ and the very fast oscillatory phase term $\exp(-j\beta z)$ as

$$\Psi(\mathbf{r}) = \phi(\mathbf{r}) \exp(-j\beta z), \tag{3.2}$$

where

$$\beta = n_{ref} k_0. \tag{3.3}$$

n_{ref} is the reference index, for which the refractive index of the substrate or the cladding is generally used. Substituting (3.2) into (3.1), we obtain

$$\frac{\partial^2\phi}{\partial z^2} - 2j\beta\frac{\partial\phi}{\partial z} + \nabla_\perp^2\phi + (k_0^2 n^2 - \beta^2)\phi = 0, \tag{3.4}$$

where $\nabla_\perp^2$ is the Laplacian in the lateral directions and is expressed as

$$\nabla_\perp^2 = \frac{\partial^2}{\partial x^2} + \frac{\partial^2}{\partial y^2}. \tag{3.5}$$

Substituting (3.3) into (3.4), we have

$$2j\beta\frac{\partial\phi}{\partial z} - \frac{\partial^2\phi}{\partial^2 z^2} = \nabla_\perp^2\phi + k_0^2(n^2 - n_{ref}^2)\phi. \tag{3.6}$$

If the second derivative of the wave function is neglected, then (3.6) is reduced to

$$2j\beta\frac{\partial\phi}{\partial z} = \nabla_\perp^2\phi + k_0^2(n^2 - n_{ref}^2)\phi. \tag{3.7}$$

This is called the Fresnel approximation or the paraxial approximation. The paraxial approximation is limited in treating wide-angle propagation. Beams containing appreciable Fourier components at angles of more than a few degrees from the propagation axis experience substantial phase errors. For the analysis of our multimode waveguides, the wide-angle formulation is required.

The wide-angle formulation (3.6) can be written as

$$2j\beta\frac{\partial\phi}{\partial z} - \frac{\partial^2\phi}{\partial^2 z^2} = P\phi, \tag{3.8}$$

where

$$P = \nabla_\perp^2 + k_0^2(n^2 - n_{ref}^2). \tag{3.9}$$

Equation (3.8) can be rewritten in the form

$$\frac{\partial}{\partial z}\left(1 + \frac{j}{2\beta}\frac{\partial}{\partial z}\right)\phi = -\frac{j}{2\beta}P\phi, \tag{3.10}$$

and therefore

$$\frac{\partial\phi}{\partial z} = \frac{-\frac{j}{2\beta}P}{1 + \frac{j}{2\beta}\frac{\partial}{\partial z}}\phi. \tag{3.11}$$

Equation (3.11) suggests the recurrence relation

$$\frac{\partial}{\partial z}\Big|_n = \frac{-\frac{j}{2\beta}P}{1 + \frac{j}{2\beta}\frac{\partial}{\partial z}|_{n-1}}. \tag{3.12}$$

Using (3.12) in the denominator of (3.11), we obtain a propagator of the form

$$\left.\frac{\partial\phi}{\partial z}\right|_n = -j\frac{N}{D}\phi, \tag{3.13}$$

where N and D are polynomials in P. Equation (3.13) is a Padé (n,d) approximation of the true Helmholtz operator. The most useful low-order Padé operators are shown in table 3.1.

Table 3.1: Useful low-order Padé approximants for the Helmholtz operator

order	$\frac{N}{D}$
(1,0)	$\frac{P}{2\beta}$
(1,1)	$\frac{\frac{P}{2\beta}}{1+\frac{P}{4\beta^2}}$
(2,2)	$\frac{\frac{P}{2\beta}+\frac{P^2}{4\beta^3}}{1+\frac{3P}{4\beta^2}+\frac{P^2}{16\beta^4}}$
(3,3)	$\frac{\frac{P}{2\beta}+\frac{P^2}{2\beta^3}+\frac{3P^3}{32\beta^5}}{1+\frac{5P}{4\beta^2}+\frac{3P^2}{8\beta^4}+\frac{P^3}{64\beta^6}}$

If (3.13) is discretized using standard centered differencing, we obtain

$$D(\phi^{m+1}-\phi^m) = \frac{-j\Delta z}{2}N(\phi^{m+1}-\phi^m), \tag{3.14}$$

which can be rewritten as

$$\phi^{m+1} = \frac{D-j(\Delta z/2)N}{D+j(\Delta z/2)N}\phi^m. \tag{3.15}$$

Since N and D are polynomials in P, (3.15) can be recast in the form

$$\phi^{m+1} = \frac{\sum_0^n \xi_i P^i}{\sum_0^n \xi_i^* P^i}\phi^m. \tag{3.16}$$

$\xi_1 = P^0 = 1$ and the other ξ's are easily determined from the coefficients of the polynomials N and D. Since a polynomial of degree n can always be factored in terms of its n roots, equation (3.16) can be written as

$$\phi^{m+1} = \frac{(1 + a_1 P)(1 + a_2 P) \cdots (1 + a_n P)}{(1 + a_1^* P)(1 + a_2^* P) \cdots (1 + a_n^* P)} \phi^m. \tag{3.17}$$

The parameters in (3.16) and (3.17) can be easily related. For example, in our simulation, a Padé (3,3) operator is used, we have

$$\begin{aligned} a_1 + a_2 + a_3 &= \xi_1 \\ a_1 a_2 + a_2 a_3 + a_1 a_3 &= \xi_2 \\ a_1 a_2 a_3 &= \xi_3. \end{aligned} \tag{3.18}$$

In general, determination of a's requires a one-time solution of an nth-order complex algebraic equation. From equation (3.17), it is apparent that a propagator can be decomposed into a multistep algorithm as

$$\phi^{m+\frac{i}{n}} = \frac{(1 + a_i P)}{(1 + a_i^* P)} \phi^{m+\frac{i-1}{n}}. \tag{3.19}$$

where $i = 1, 2, \cdots, n$. In the simulation, the a's are obtained by solving the following equations

$$\begin{aligned} a_1 + a_2 + a_3 = \xi_1 &= \frac{1}{4\beta^2}(5 - j\beta\Delta z) \\ a_1 a_2 + a_2 a_3 + a_1 a_3 = \xi_2 &= \frac{1}{8\beta^4}(3 - j2\beta\Delta z) \\ a_1 a_2 a_3 = \xi_3 &= \frac{1}{64\beta^6}(1 - j3\beta\Delta z). \end{aligned} \tag{3.20}$$

The beam propagation is then calculated by the multistep algorithm. Programming of the BPM algorithm is discussed in Appendix B.

3.3 Two design examples of MWH devices

Based on the design principle, two devices are designed and simulated using 2-D wide-angle beam propagation method (WA-BPM) using the Padé (3,3) approximant operator. The effective indices of the waveguide core (1.516) and of the cladding region (1.0) are estimated using the effective index method in accordance with the fabrication technique used later for experimental demonstration. In the simulations presented here, the hologram is modeled as smooth perturbations to the effective index of the waveguide core.

3.3.1 Mode-order converter

A mode-order converter based on MWH using the configuration in Fig. 2.1 is proposed and simulated. The design method described in section 2.8.1 is used to calculate the hologram for an anti-diagonal matrix in (2.40) that converts the mode-order in the multimode waveguide. The width of the waveguide is 16 μm and the length is 1.5 mm. The maximum index modulation depth is approximately 0.003. The slices of the BPM simulation are illustrated in Fig. 3.1 for four different mode conversion pairs, Fig. 3.1(a) shows TE_{00} to TE_{30}, Fig. 3.1(b) shows TE_{10} to TE_{20}, Fig. 3.1(c) shows TE_{20} mode to TE_{10}, and Fig. 3.1(d) shows TE_{30} to TE_{00}. The advantage of the proposed approach is that the MWH mode converter is only 1.5 mm long. This device is more than ten times more compact then the mode converter made from multichannel branching waveguides [50].

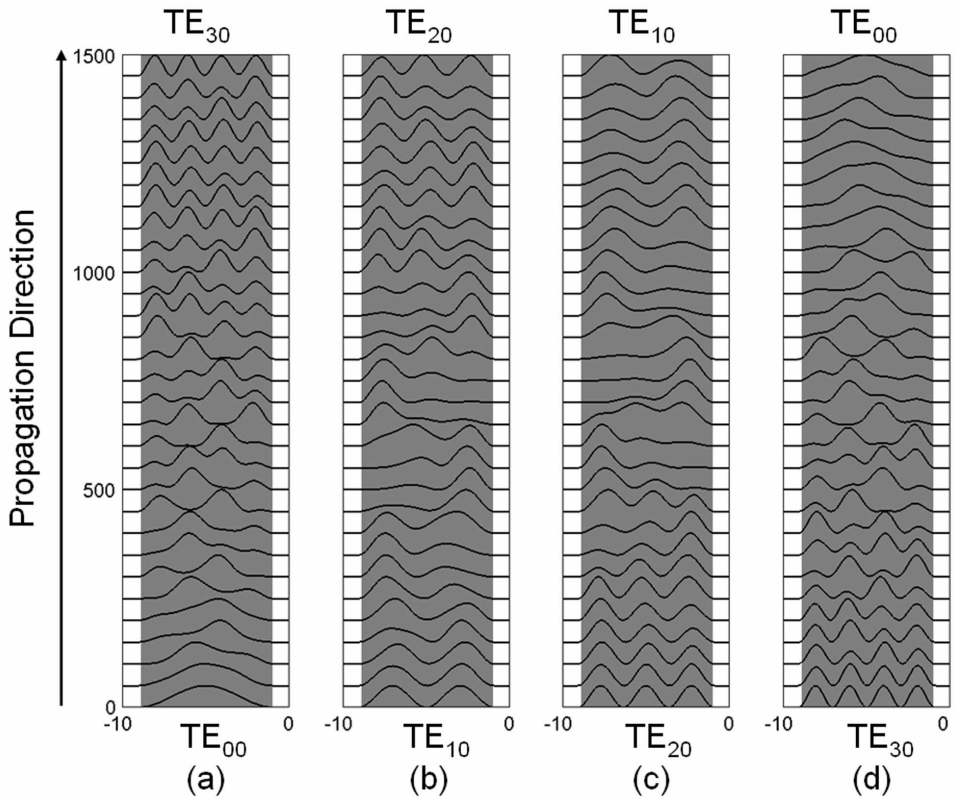

Figure 3.1: Normalized intensity slices of the BPM simulation showing the evolution of modes along the proposed MWH mode-order converter.

3.3.2 Hadamard transformer

The Hadamard transformer is capable of recognizing multiple phase-modulated labels as demonstrated recently using a star network [51]. Using the matrix-vector multiplier configuration, a Hadamard transformer is proposed and simulated. The transfer matrix of a 4×4 Hadamard transformer is described by

$$\frac{1}{2}\begin{bmatrix} 1 & 1 & 1 & 1 \\ 1 & -1 & 1 & -1 \\ 1 & 1 & -1 & -1 \\ 1 & -1 & -1 & 1 \end{bmatrix} \tag{3.21}$$

The MWH is designed using the eigenvectors of the MMI coupler to calculate the grating as described in section 2.8.2. The width of the multimode section of the MMI coupler is 16 μm, and the length is chosen to be at the first imaging length of 2052 μm. The maximum index modulation depth is approximately 0.003. It can be seen from the BPM simulation in Fig. 3.2 that four orthogonal phase modulated spatial patterns are mapped into four different ports as described by the matrix in (3.21). This approach offers the advantage of compactness and does not require optical crossings (see Fig. 1.1) as encountered in the star network approach [24] [25].

3.4 Spatial optical pattern generator/correlator

In this section, the concept and theory of a spatial optical pattern generator/correlator is introduced. An experimental verification of the MWH theory and

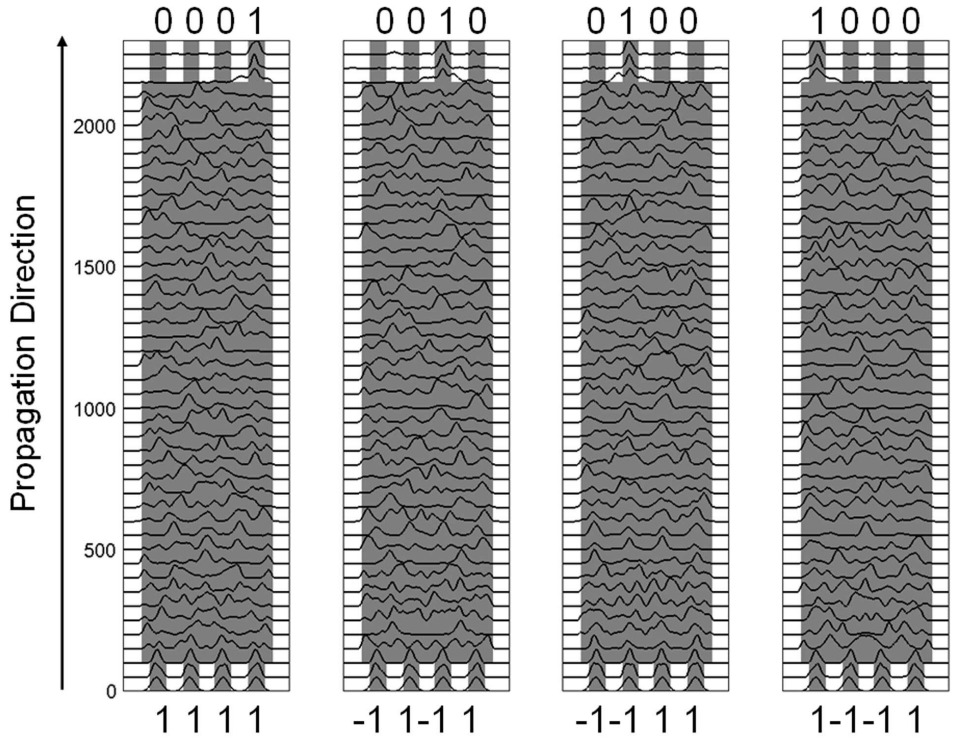

Figure 3.2: Normalized intensity slices of the BPM simulation of four phase modulated patterns in a MWH Hadamard transformer.

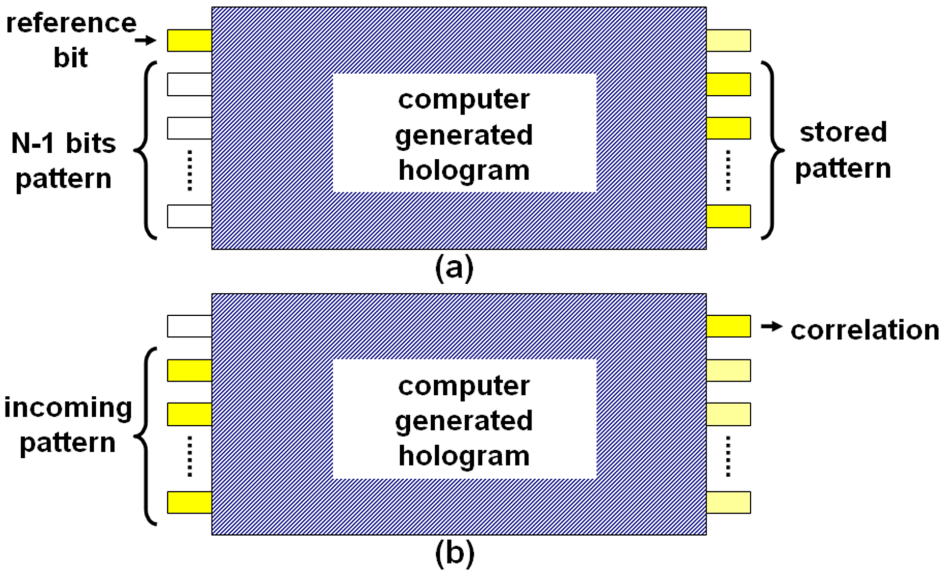

Figure 3.3: Schematic of a MWH optical pattern generator/correlator using MMI. (a) the stored pattern is regenerated when light is coupled into the reference bit port. (b) the reference bit is reconstructed with an amplitude that is proportional to the correlation of the incoming pattern and the stored pattern.

the BPM model using fabricated optical pattern generators will be described in the subsequent sections.

The concept of a MWH optical processor is illustrated in Fig. 3.3. The $N \times N$ MMI coupler with MWH in the figure is at the self-imaging length. In analogy to traditional holograms, one input port is designated as the reference bit, and the other ports are used to represent the image, which in this case is an $N-1$ bit spatial pattern. When light is coupled into the reference bit port, as shown in Fig. 3.3(a), the stored $N-1$ bit spatial pattern is reconstructed at the output ports. On the other hand, when the $N-1$ bit spatial pattern is coupled into the device as shown in Fig. 3.3(b), the reference bit is reconstructed with an amplitude that is proportional to the correlation of the incoming pattern and the stored pattern.

3.4.1 Solution for the output of optical pattern generator/correlator (MWH processor)

The pattern generator/correlator (MWH processor) is designed by the interference of the reference bit $\mathbf{R}$ and the stored pattern $\mathbf{S}$ as outlined in section 2.8.2. The combination of these two patterns can be written as a single vector, $\mathbf{W} = \mathbf{R}+\mathbf{S}$. In the following calculations, $\mathbf{W}$ is a unit vector($|\mathbf{W}|^2 = 1$).

As described in section 2.8, the interference patterns between any two eigenvectors correspond to individual grating components in the hologram. For $\mathbf{W} = [W_1, W_2, \cdots, W_N]$, the corresponding hologram of length l can thus be written as,

$$\exp(-j\mathbf{K}l). \tag{3.22}$$

The coupling matrix $\mathbf{K}$ is related to individual components of $\mathbf{W}$ as

$$\mathbf{K} = C\tilde{\mathbf{K}} = C \begin{bmatrix} W_1W_1 & W_1W_2 & W_1W_3 & \cdots & W_1W_N \\ W_2W_1 & W_2W_2 & W_2W_3 & \cdots & W_2W_N \\ W_3W_3 & W_3W_3 & W_3W_3 & \cdots & W_3W_N \\ \vdots & \vdots & \vdots & \cdots & \vdots \\ W_NW_1 & W_NW_2 & W_NW_3 & \cdots & W_NW_N \end{bmatrix}, \tag{3.23}$$

where C is the coupling efficiency. We calculate the following matrix product first,

$$\tilde{\mathbf{K}}\tilde{\mathbf{K}} = |\mathbf{W}|^2 \begin{bmatrix} W_1W_1 & W_1W_2 & W_1W_3 & \cdots & W_1W_N \\ W_2W_1 & W_2W_2 & W_2W_3 & \cdots & W_2W_N \\ W_3W_3 & W_3W_3 & W_3W_3 & \cdots & W_3W_N \\ \vdots & \vdots & \vdots & \cdots & \vdots \\ W_NW_1 & W_NW_2 & W_NW_3 & \cdots & W_NW_N \end{bmatrix} = \tilde{\mathbf{K}}. \tag{3.24}$$

We can expand (3.22) as

$$\exp(-j\mathbf{K}l) = \exp[(-jCl)\tilde{\mathbf{K}}] = \left[\mathbf{I} + (-jCl)\tilde{\mathbf{K}} + \frac{(-jCl)^2}{2!}\tilde{\mathbf{K}}^2 + \cdots\right]. \tag{3.25}$$

With input pattern $\mathbf{P}(0)$, the expression for the output is

$$\mathbf{P}_{out} = \exp(-j\mathbf{K}l)\mathbf{P}(0). \tag{3.26}$$

Using (3.24) and (3.25), we can rewrite (3.26) as

$$\begin{aligned}\mathbf{P}_{out} &= \mathbf{P}(0) + \left[(-jCl) + \frac{(-jCl)^2}{2!} + \cdots\right]\tilde{\mathbf{K}}\mathbf{P}(0) \\ &= \mathbf{P}(0) + [\exp(-jCl) - 1][\mathbf{W}\cdot\mathbf{P}(0)]\mathbf{W}. \end{aligned}\tag{3.27}$$

Since we know $\mathbf{W} = \mathbf{R} + \mathbf{S}$, the solution for the optical processor is thus,

$$\mathbf{P}_{out} = \mathbf{P}(0) + [(\mathbf{R}+\mathbf{S})\cdot\mathbf{P}(0)][\exp(-jCl) - 1](\mathbf{R}+\mathbf{S}). \tag{3.28}$$

As a reminder here, $\mathbf{P}(0)$ is the input pattern, $\mathbf{R}$ is the reference bit, $\mathbf{S}$ is the stored pattern, l is the length of the hologram, and the coupling efficiency, C, is proportional to the index modulation depth. For pattern generation, $\mathbf{P}(0) = \mathbf{R}$, and it can be seen from (3.28) that the intensity of the generated pattern $\mathbf{S}$ is proportional to $[1 - \cos(Cl)]$. For pattern correlation, since $\mathbf{R}$ and $\mathbf{P}(0)$ do not overlap at the input waveguides, the intensity of the generated reference bit $\mathbf{R}$ is proportional to

$$[\mathbf{S}\cdot\mathbf{P}(0)]^2[1 - \cos(Cl)], \tag{3.29}$$

which is proportional to the correlation of the stored pattern and the input pattern.

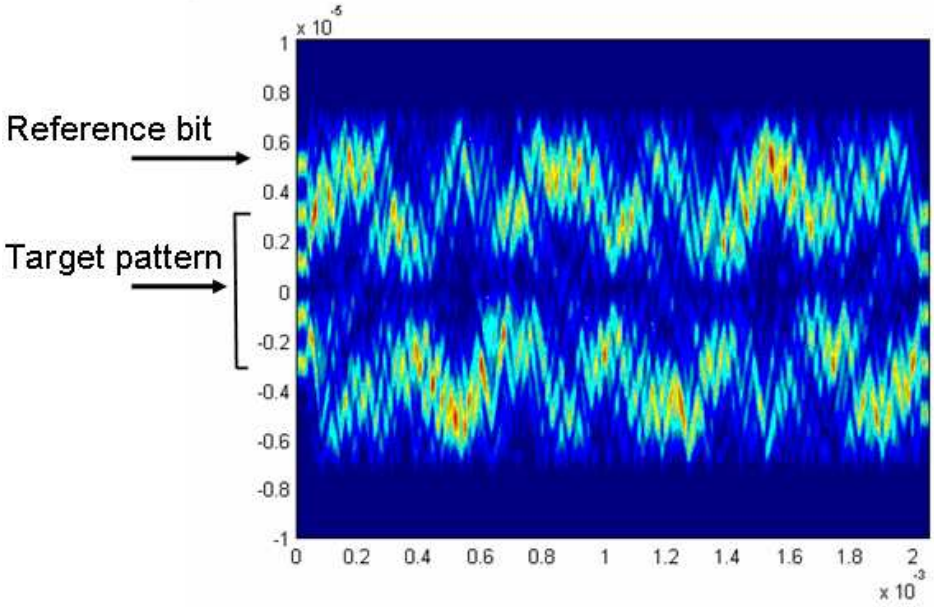

Figure 3.4: Simulated interference pattern between the reference bit and the stored pattern. This interference pattern is proportional to the index variation in the MWH processor.

3.4.2 Simulation of optical pattern generator/correlator

MWH processors with 4-bit stored patterns are designed using our theory and simulated by the BPM model. The index of refraction variation of the 6×6 MWH processor is proportional to the intensity pattern of the write pattern, which consists of the reference bit and the stored pattern as described in the previous section. The index variation of constructed hologram is proportional to the intensity pattern shown in Fig. 3.4. The output waveguides are placed at the mirror image plane as can be seen in the figure. When the incoming pattern matches that of the stored pattern, the reference bit is reconstructed (circled) as can be seen in Fig. 3.5. The amplitude of the reconstructed reference bit is expected to be proportional to the correlation of the incoming pattern and the stored pattern.

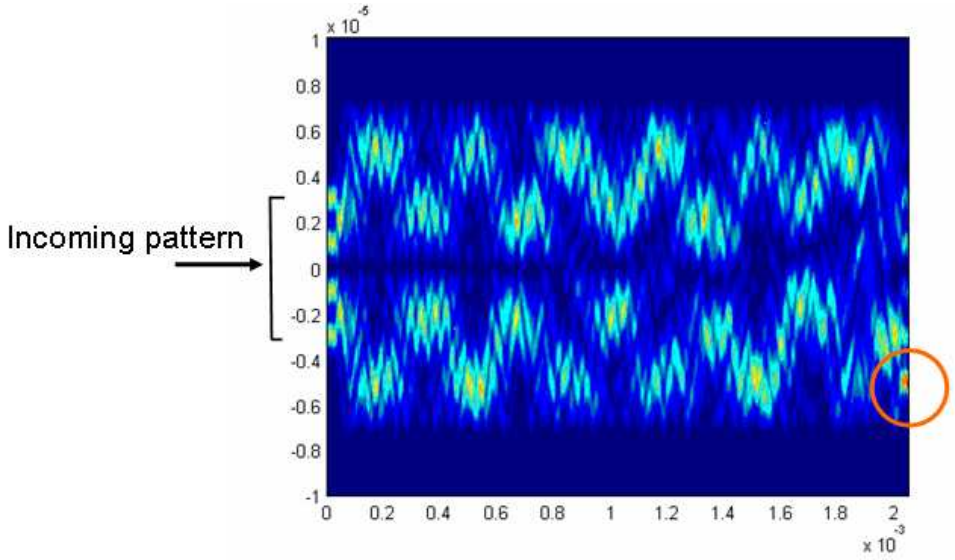

Figure 3.5: Reading the hologram with index variation proportional to the intensity pattern in Fig. 3.4. The incoming pattern is the same as the stored pattern.

Optical pattern correlation of intensity modulated patterns

The simulated correlation outputs of a MWH correlator with (1 1 1 1) stored pattern using different 4-bit intensity modulated input patterns are shown in Fig. 3.6. The correlation outputs are normalized and compared with ideal correlation results. It can be seen from the figure that the correlation result is close to ideal correlation as predicted by the derivation using coupled mode theory. This shows that our theory is valid.

Optical pattern correlation of phase modulated patterns

Using phase modulated input patterns, the correlation outputs of the MWH correlator are simulated. The wavelength dependence of the MWH correlator is also investigated at the same time. As shown in Fig. 3.7, close to ideal correla-

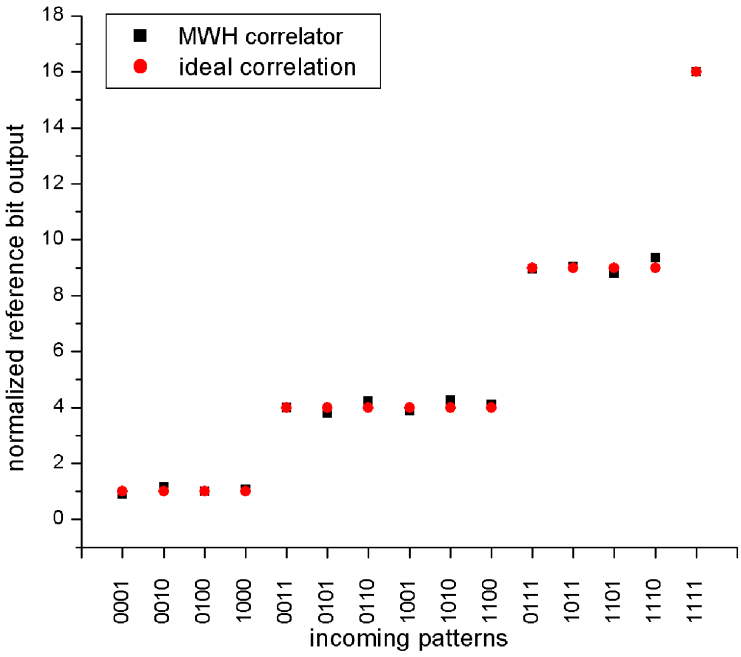

Figure 3.6: Simulated correlation results of a MWH correlator with the stored pattern (1 1 1 1). Square: MWH correlator; Circle: ideal correlation.

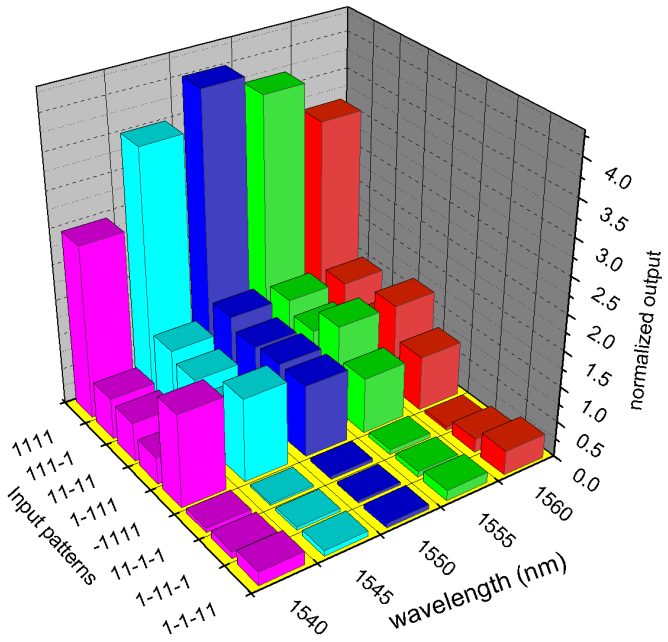

Figure 3.7: Correlation results and wavelength dependence of a MWH correlator.

tion performance can be observed at the designed operating wavelength (1550 nm). Degraded correlation performance can be observed when the wavelength is detuned from the designed wavelength.

Effect of hologram and index modulation depth

The effect of the hologram length in the MMI coupler is also investigated. Holograms are written on different fractions of the total length of the MMI coupler. The correlation output of the matched pattern for different hologram lengths is recorded. The simulated data are fit with (3.29) and plotted in Fig. 3.8(a). The parameter C in (3.29) is proportional to the depth of index modulation. The index modulation depth is varied in the simulation with fixed hologram length. The

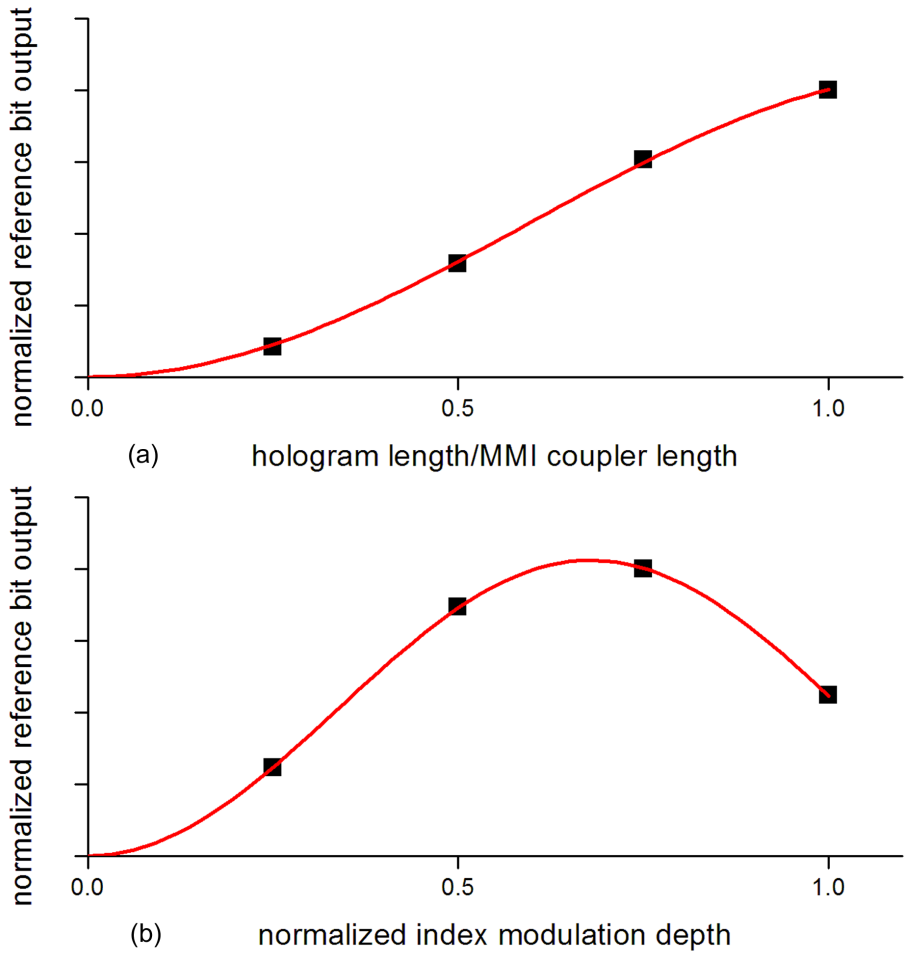

Figure 3.8: Simulated effects of (a) hologram length and (b) index modulation depth on the reference bit output. Square: WA-BPM simulation; Curve: Fit using (16).

simulation result and the fit with (3.29) are shown in Fig. 3.8(b).

MWH with binary index modulation

The smooth index modulation used in the analytical theory is difficult to obtain in lithographically fabricated devices. The feasibility of lithographically fabricated devices is investigated by simulations of the MWH pattern generator/correlator with binary index modulation as illustrated in Fig. 3.9. Small differences are found in the

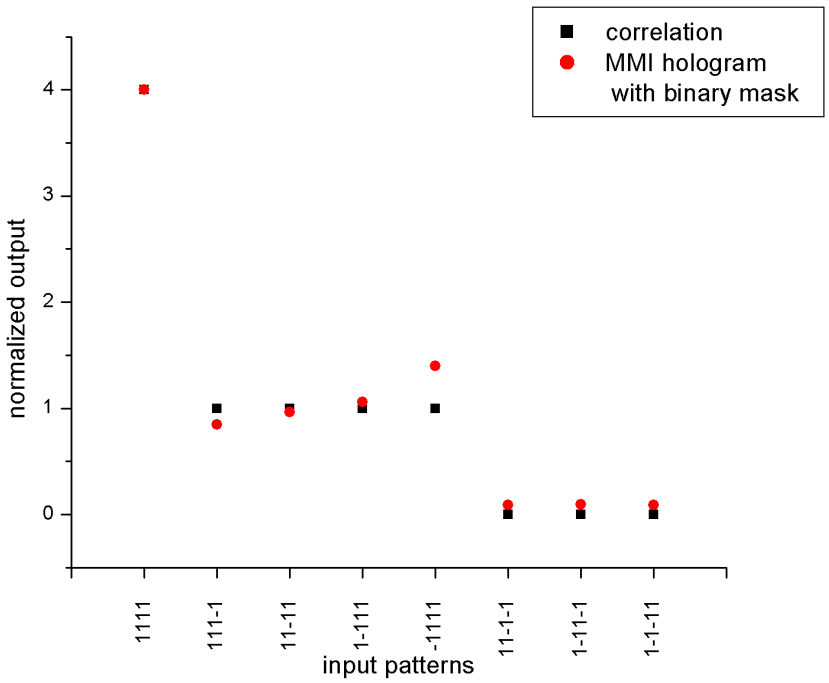

Figure 3.9: Pattern correlation using a MWH correlator designed for stored pattern (1111) with binary index modulation

generation/correlation properties, but the overall device performance is not affected.

3.5 Experiment

The MWH pattern generators were fabricated using passive waveguides on a Si wafer. 4.6 microns of SiO_2 was used for the bottom cladding layer. The core consists of a 2.4 μm layer of Cyclotene^{TM} (BCB), and the upper cladding is air (Fig. 3.10). This asymmetric waveguide design was selected so that index variations for each hologram could be created lithographically by etching shallow indentations on the top of the Cyclotene^{TM} surface (Fig. 3.11). The waveguide and hologram pattern was transferred using conventional photolithography using i-line projection

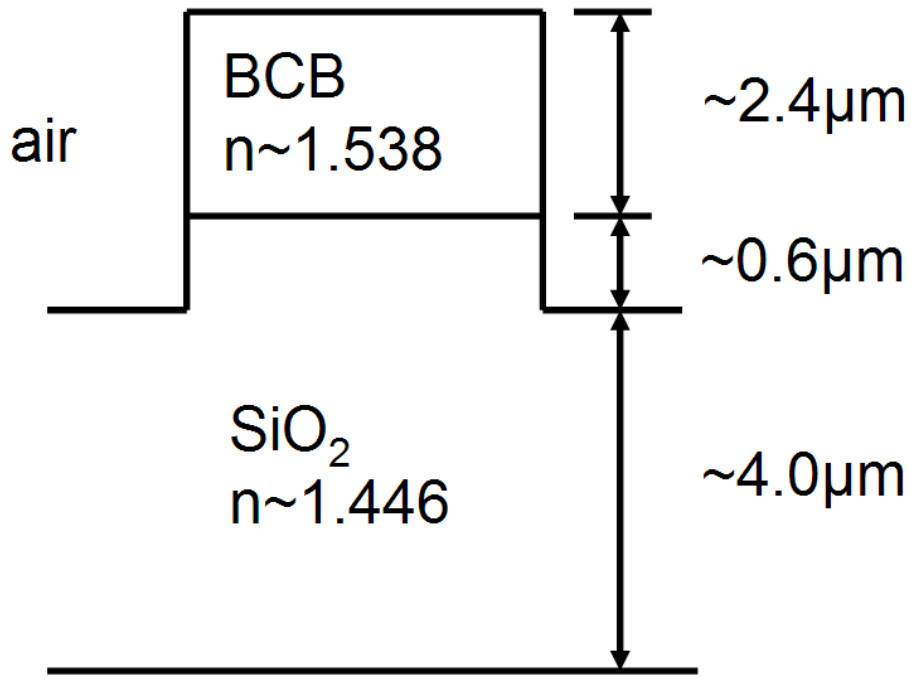

Figure 3.10: The layered structure of fabricated MWH pattern generators

aligner and reactive ion etching (RIE). The device width is 16 μm (Fig. 3.12), and the length of the device is chosen at the first mirror-imaging length, 1026 μm (Fig. 3.13). Devices were probed by coupling a CW laser at 1560 nm into the reference bit port as shown in Fig. 3.14. The output was imaged with an Electrophysics MicronViewer 7290 IR camera. It can be seen from Fig. 3.15 that the patterns stored in the MWH pattern generator were reconstructed as predicted by coupled mode theory and WA-BPM simulation.

By varying the wavelength of the CW laser, the wavelength dependent diffraction efficiency of the device was measured. The light was coupled into the reference bit port of a pattern generator with 001 pattern. Fig. 3.16 shows a measurement of the output intensity profile of pattern generators with and without hologram using a

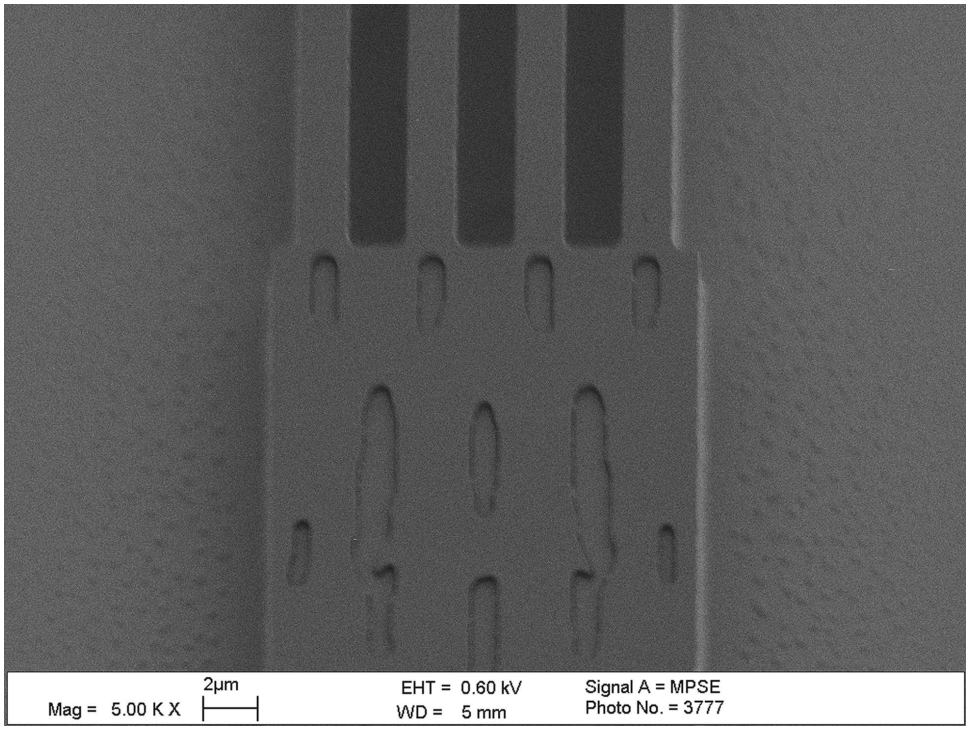

Figure 3.11: Plan-view SEM micrograph of a section of a MWH pattern generator. The shallow etched computer generated pattern is visible on the surface of the device.

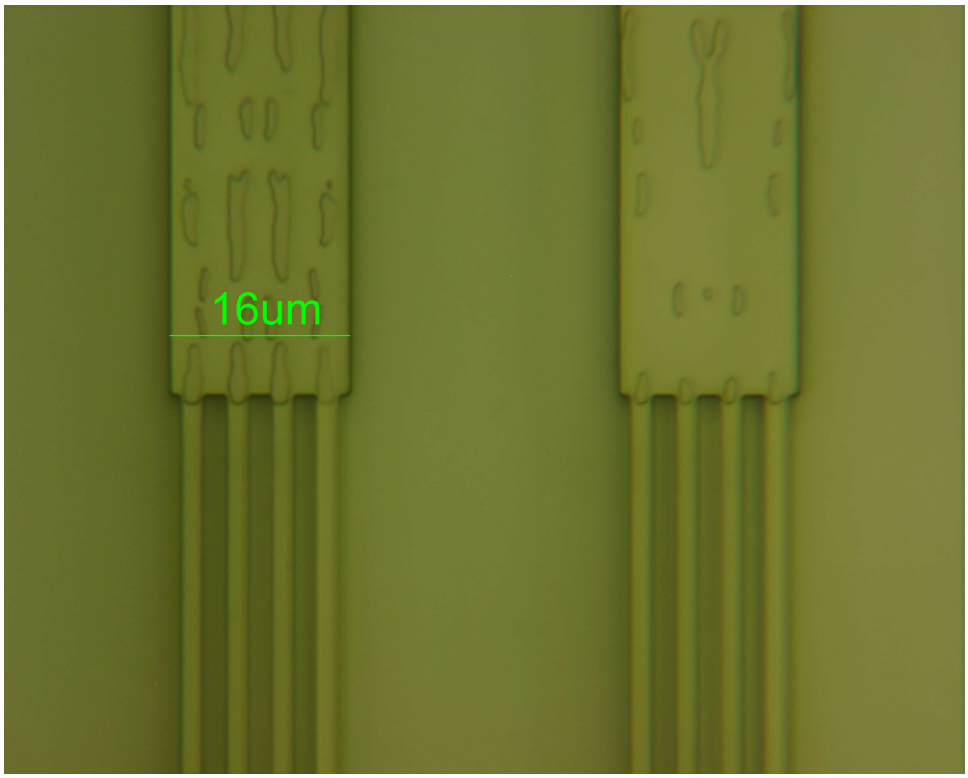

Figure 3.12: Optical microscope picture showing the width and access waveguides of fabricated MWH pattern generators. The hologram patterns are visible on the multimode waveguides.

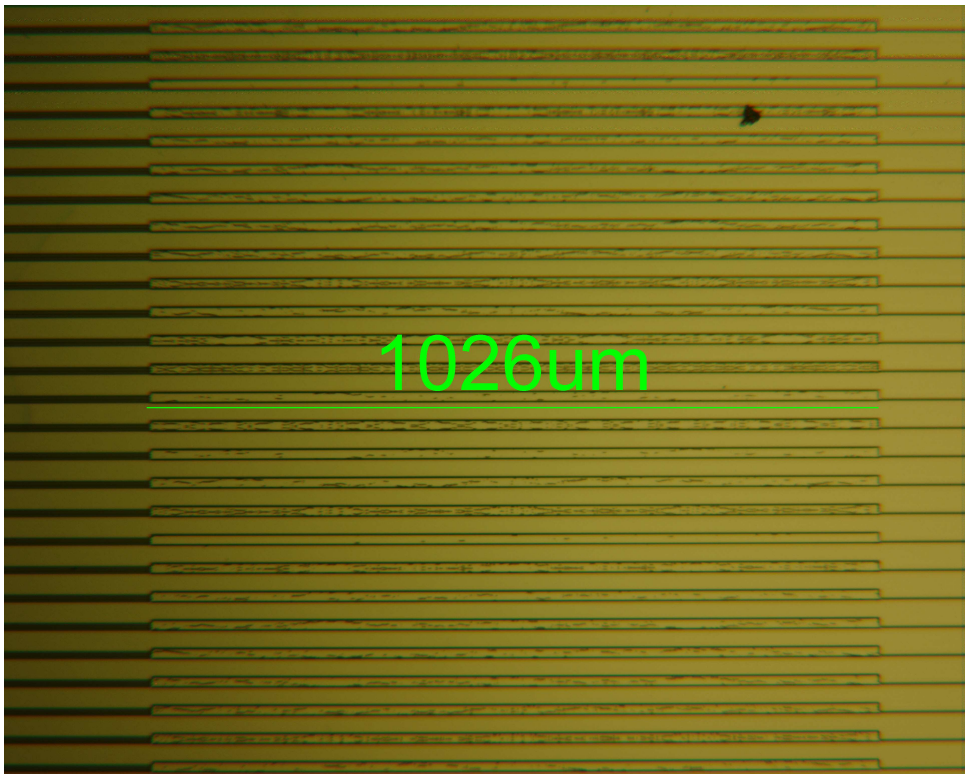

Figure 3.13: Optical microscope picture showing the whole length of fabricated MWH pattern generators. The hologram patterns are visible on the multimode waveguides. The reference bit inputs are on the right side, and the generated pattern outputs are on the left side.

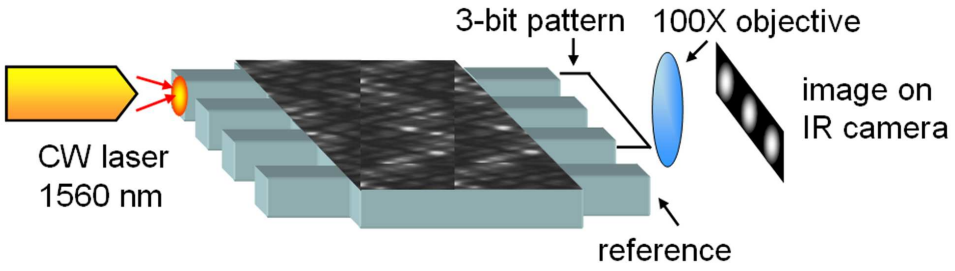

Figure 3.14: Schematic of the experimental setup to measure the spatial pattern stored in the MWH pattern generator. The output spatial pattern is imaged with an IR camera.

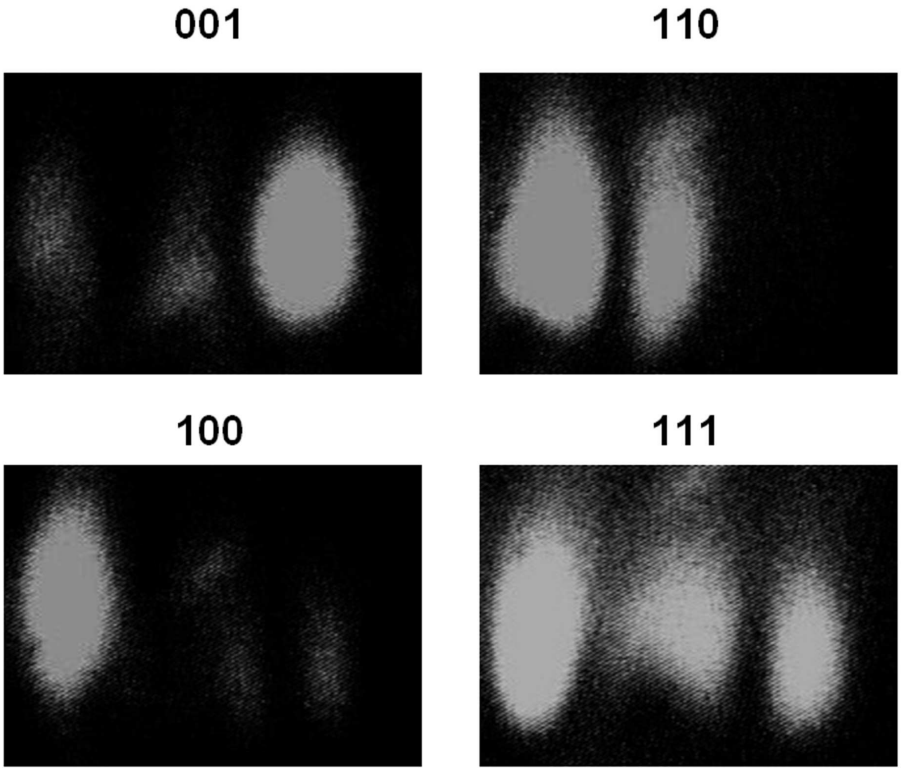

Figure 3.15: Experimental results of 3 bit spatial pattern generation by MWH pattern generator.

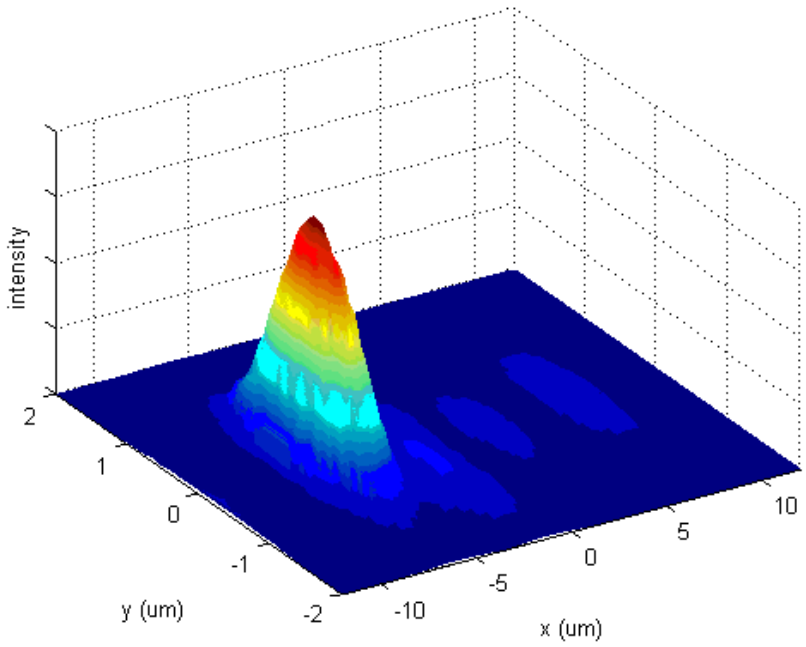

Figure 3.16: Output intensity profile of a pattern generator without embedded hologram measured with a scanning lensed fiber.

scanning lensed fiber. When light was coupled into a pattern generator without embedded hologram, the output shows the reference bit only. When light was coupled into a pattern generator with 001 hologram, most of the reference bit is scattered into the 001 output pattern as shown in Fig. 3.17.

The intensity of the "1" bit in the generated pattern was recorded as a function of wavelength and plotted in Fig. 3.18. The results from WA-BPM simulation are also plotted, and good agreement between the BPM model and the measured data can be seen in the figure. An estimation of the bandwidth of MWH devices can be obtained using co-directional coupling theory [53] as shown in the next section. Using the fabricated device parameter, the FWHM of the spectral response for mode coupling between the lowest and the highest order modes is calculated to be ~ 40

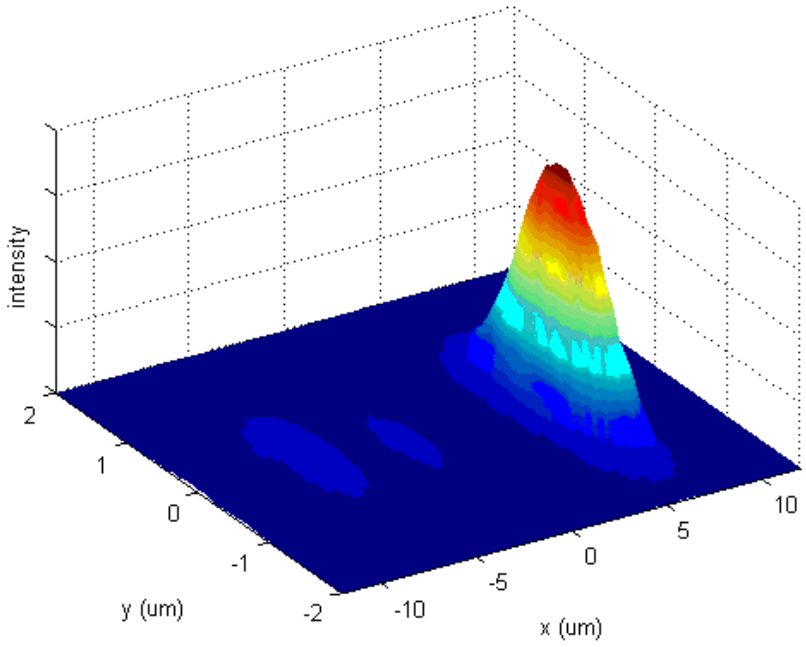

Figure 3.17: Output intensity profile of a pattern generator with 001 hologram measured with a scanning lensed fiber.

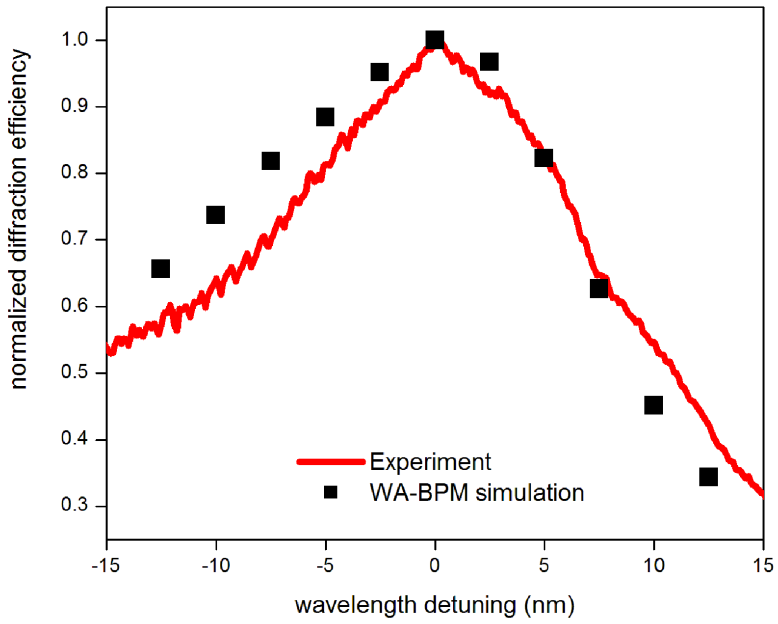

Figure 3.18: Wavelength dependence of the diffraction efficiency of a MWH pattern generator patterned with 001 pattern.

nm. In reality, the MWH device consists of multiplexed gratings with different periodicity, and wavelength dependence of the self-imaging property also needs to be taken into consideration. The excellent agreement between our BPM model and experimental data shows that different effects are predicted correctly by our model. Our BPM model is thus a valuable tool for designing and analyzing these devices.

3.6 Analysis of MWH length, bandwidth, and fabrication tolerance

In the theoretical analysis, it is assumed that the Bragg conditions are satisfied for every grating element, and only the synchronous terms are collected to obtain (2.36). The validity of the condition and the effect of the crosstalk between gratings

can be considered qualitatively as follows. Considering two grating vectors $\mathbf{k}_{ji} = \beta_j - \beta_i$ and $\mathbf{k}_{ki} = \beta_k - \beta_i$, when the jth mode is present, grating $\mathbf{k}_{ji}$ scatters it into the ith mode, however, a small fraction of its power is also scattered by the grating $\mathbf{k}_{ki}$ into the ith mode. The fraction of the ith mode from grating $\mathbf{k}_{ki}$ is the crosstalk and can be estimated by [52]

$$(\kappa L)^2 \frac{\sin^2(\delta L)}{(\delta L)^2}, \quad \delta \gg \kappa \tag{3.30}$$

where κ is the coupling coefficient of the grating, L is the length of the grating, and $\delta = \beta_k - \beta_j$. For a multimode channel waveguide of width W and core index n_c , δ can be estimated using (2.22) as

$$\delta = \frac{\pi\lambda}{4n_c W^2}(k^2 - j^2), \tag{3.31}$$

where λ is the wavelength. Equations (3.30) and (3.31) give an estimate of the range of coupling coefficient for the Bragg condition approximations to be valid. Also, it can be seen from (3.30) that when δL is sufficiently large, the crosstalk is negligible. Using the location of the second zero of (3.31) as a measurement of selectivity as in ref. [52], the requirement on the minimum length of the hologram L_{min} is

$$L_{min} \geq \frac{2\pi}{\delta} = \frac{8n_c W^2}{\lambda(k^2 - j^2)} \geq \frac{8n_c W^2}{3\lambda}. \tag{3.32}$$

The simulated and fabricated device in this thesis are designed to be at the first mirror image length, $4n_c W^2/\lambda$, and the first direct image length, $8n_c W^2/\lambda$, of the multimode waveguides, with the MWHs covering the whole lengths of the devices. Although the self-imaging property is not essential for this class of devices, it offers a

simplified design method for MWH as described in 2.8.2 and satisfies the minimum length requirement of (3.32).

The specific polymer waveguide system chosen for the experiment is used to investigate the fabrication tolerances and scalability of the MWH devices. The spatial pattern generator/correlator described in section 3.4 and demonstrated in experiments is used in the simulations. First, the fabrication tolerance on the lateral shift between the MMI coupler and the hologram is investigated since they are fabricated in two different lithography steps. Using the BPM model, the diffraction efficiency and the discrimination capability are calculated and plotted in Fig. 3.19. The discrimination capability is defined as

$$1 - \frac{\max|c|^2}{|a|^2}, \tag{3.33}$$

where c is the cross-correlation and a is the auto-correlation.

From (2.37) and (2.38), the lateral shift can be estimated as errors to the coupling coefficients due to the change in the overlap integrals. Since the MWH is designed using the eigenvectors of the MMI in this example, the error to the coupling coefficient is estimated using the change in the overlap integral of these eigenvectors due to the lateral shift. The input waveguides are well separated in this case, and the eigenvectors can be approximated using the guided modes of the single mode access ports. This way, each coupling coefficient is affected by the same amount and the effect of the lateral shift can be estimated as a change to the overall coupling efficiency, C, in (3.29). With these approximations, C can be written as a function

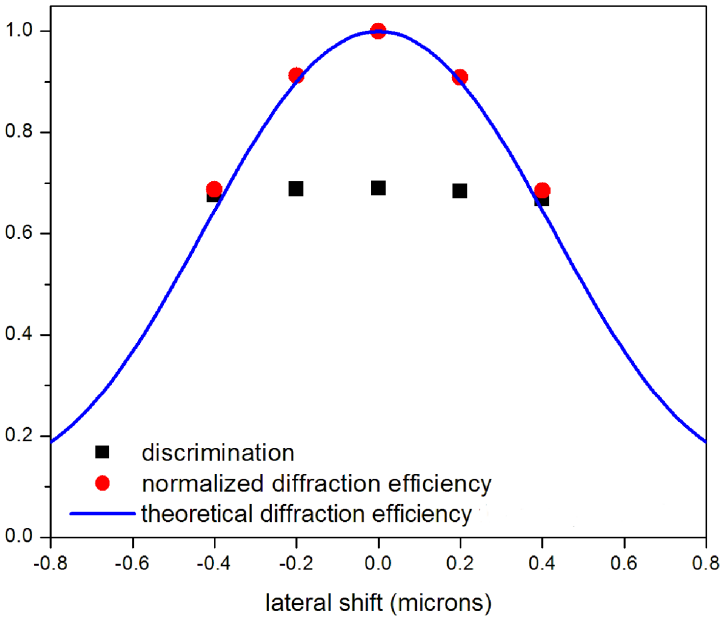

Figure 3.19: BPM simulation and theoretical results on the effect of hologram lateral shift on the diffraction efficiency and the discrimination capability of the MWH pattern generator/correlator.

of the lateral shift Δx as

$$C(\pm\Delta x) = C_0 \frac{\int \Phi^2(x)\Phi^2(x \pm \Delta x)\mathrm{d}x}{\int \Phi^4(x)\mathrm{d}x}, \tag{3.34}$$

where C_0 is the coupling efficiency when the lateral shift is zero, and Φ is the mode of the single mode access ports. Since the lateral shift only affects the overall coupling coefficient, it is not surprising that the discrimination capability in Fig. 3.19 is almost constant with the lateral shift in the range of -0.5 to 0.5 μm offset. A theoretical prediction of the diffraction efficiency is obtained using (3.34) in (3.29) and plotted in Fig. 3.19.

For applications in modern high-speed optical communications systems, the scalability and bandwidth of the MWHs are investigated. The MWH consists basically of multiplexed long period gratings on a MMI coupler. The wide transmission bandwidth of long period grating structure is well documented in the literature [54]. The spectral dependence of these long period gratings can be determined by the expressions [53] derived for co-directional coupling. The ratio of power coupled into mode n from mode m is given by

$$\frac{P_n}{P_m} = \frac{sin^2\left[\kappa_{mn} L \sqrt{1 + \left(\frac{\delta}{\kappa_{mn}}\right)^2}\right]}{1 + \left(\frac{\delta}{\kappa_{mn}}\right)^2}, \tag{3.35}$$

where δ is the detuning from the grating period, κ_{mn} is the coupling coefficient, and L is the grating length. Assuming maximum power transfer, that is, $\kappa_{mn} L = \pi/2$, the FWHM $\Delta\lambda$ of the spectral response given approximately by (3.35) is [53]

$$\Delta\lambda = \frac{0.8\lambda^2}{L\Delta n_{mn}}, \tag{3.36}$$

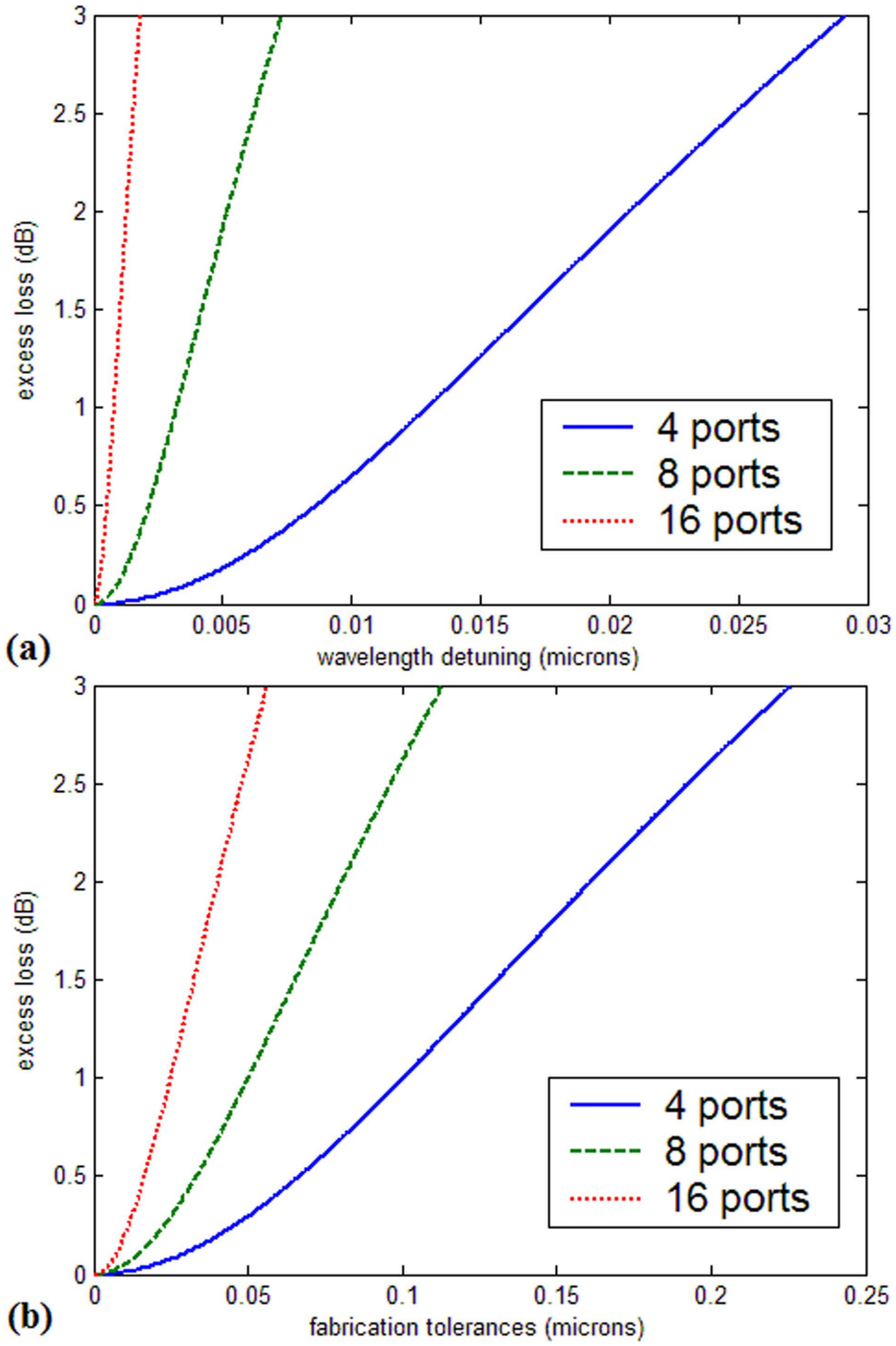

Figure 3.20: Bandwidth (a) and fabrication tolerance (b) of the polymer MMI coupler used in our experiment. The practical scaling of these devices is limited by the proportionality between the number of ports and the sensitivity to wavelength detuning and fabrication tolerance.

where Δn_{mn} is the difference in the effective indices of modes m and n. From (2.22), we obtain,

$$\Delta n_{mn} = \frac{(n^2 - m^2)\lambda^2}{8 n_c W^2}, \tag{3.37}$$

where n_c is the core index, and W is the waveguide width. The simulated and fabricated waveguides are designed to be at the first mirror image length, $4n_cW^2/\lambda$, and the first direct image length, $8n_cW^2/\lambda$. Substituting these into (3.36), we have

$$\Delta\lambda \sim \frac{1.6\lambda}{(n^2 - m^2)}. \tag{3.38}$$

It is obvious that the bandwidth decreases for modes that are far apart. For the simulated and fabricated devices, the number of supported guided modes is around 8. It can be seen that the $\Delta\lambda$ is ~ 40 nm for mode coupling between modes 1 and 8. For high speed applications, the decrease in bandwidth limits the number of modes in the MWH devices.

From our simulations, the optical bandwidth and fabrication tolerances of the MMI coupler are the dominating factor in the performance of the MWH devices we considered in this thesis. The scalability of the MWH devices to perform transformation on large sized input vectors is thus determined by the scalability of MMI couplers. Using the formalism introduced by Besse *et. al.* [55], the bandwidth and fabrication tolerances of the polymer MMI coupler at the first mirror image length ($N = M$ in ref. [55]) are analyzed. The calculated results are shown in Fig. 3.20. The optical bandwidth and fabrication tolerances are inversely proportional to the number of ports. It can be seen from the figure that devices with larger than 8 ports will be difficult to fabricate using current fabrication technology owing to the

rapid rise in excess loss. The examples given here are only applicable to the specific material system chosen for this demonstration. It is worth noting that these limitations can be relaxed if a different material system with smaller core/cladding index contrast is chosen. However, the multimode waveguide has to support at least the same number of guided modes in order to perform the same transformations. The tradeoff will thus be increased device size.

3.7 Application to optical pattern recognition

The optical pattern generator/correlator analyzed in section 3.4 computes the correlation of the incoming patterns with a single stored pattern. In order to recognize multiple patterns using this configuration, multiple MWH devices are required. A more efficient way for pattern recognition in which a MWH can be used to recognize multiple patterns is described in this section. We begin this section by consider the unitary transformation property of MWH devices.

If we look at the 4×4 Hadamard transform matrix (3.21) as an example, it is obvious that each row of the matrix represents a four bit phase modulated pattern, and the output at each port represents the correlation of the incoming pattern and the stored pattern. So, the 4×4 Hadamard matrix computes the correlations of the incoming pattern with the four stored patterns simultaneously. Since the MWH is mathematically represented by an unitary matrix, the only restriction on the stored patterns is that the four stored patterns have to be orthonormal.

3.7.1 Pattern recognition of 4-bit phase modulated patterns

For 4-bit phase modulated patterns, there are $2^4 = 16$ possible variations, which are not all orthogonal. If the absolute phase is neglected, rather we focus on the phase difference between adjacent bits, the variations can be reduced by half, for example, (1-1 1 1) and (-1 1-1-1) are now considered the same. These eight variations can then be separated into two orthogonal groups as in table 3.2.

Table 3.2: Patterns are separated into two orthogonal groups. The correlation between any two patterns within a group is 0.

group1	group2
±(1 1 1 1)	±(1 1 1-1)
±(1 1-1-1)	±(1 1-1 1)
±(1-1 1-1)	±(1-1 1 1)
±(1-1-1 1)	±(-1 1 1 1)

Each group can be stored in a MWH with the rows of the unitary matrix represented by the patterns of the individual group. Any incoming patterns can be correlated simultaneously with all eight pattern using the schematic shown in Fig. 3.21 with two MWHs.

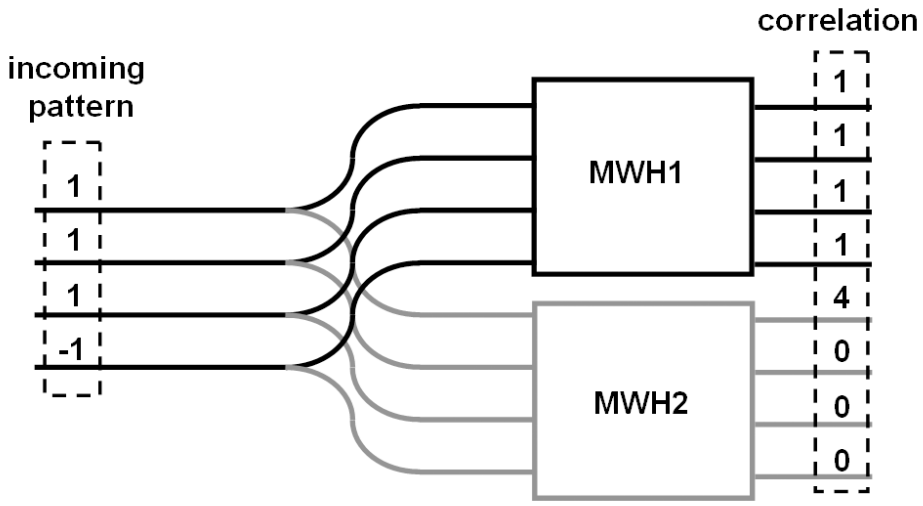

Figure 3.21: Schematic for 4-bit pattern correlation using two MWHs.

3.7.2 Analysis on pattern recognition of 2^N-bit binary phase modulated patterns

The same principle can be applied to longer patterns. We consider 2^N-bit phase modulated patterns. If we neglect the absolute phase as in the 4-bit example, the number of patterns is $2^{2^N}/2 = 2^{(2^N-1)}$. The number of MWHs needed to implement a correlator for all patterns is thus

$$\frac{2^{(2^N-1)}}{2^N} = 2^{(2^N-N-1)}. \tag{3.39}$$

It can be seen that when N is greater or equal to 3, the number of MWHs required for correlation becomes vary large, which makes signal distribution a challenge. It is obvious that a correlator consisting of multiple MWHs for long bit length pattern is difficult to implement with current fabrication technology.

Now, we analyze the contrast ratio of correlation defined as

$$R = \frac{|a|^2}{\max|c|^2}, \tag{3.40}$$

where $|a|$ is the auto-correlation and $|c|$ is the cross-correlation. For matching patterns, the auto-correlation of each 2^N-bit pattern is

$$|a|^2 = 2^N. \tag{3.41}$$

The maximum value of cross-correlation with unmatched patterns can be calculated by consider the cross-correlation between two patterns with 1 bit difference. The result is thus

$$\max|c|^2 = \frac{1}{2^N}(2^N - 2)^2. \tag{3.42}$$

The contrast ratio for 2^N bit patterns is then

$$R = \left(\frac{2^N}{2^N - 2}\right)^2. \tag{3.43}$$

For 4 bits pattern, $N = 2$, the contrast ratio is 4; for 8 bits pattern, $N = 3$, the contrast ratio is 16/9; and it can be seen that the contrast ratio decrease quickly with the increase of N.

3.7.3 Bit-error rate of pattern recognition with ideal correlators

Pattern recognition is achieved by either optically or electronically determining a match between the incoming pattern and the stored pattern. A threshold level, v_{th}, somewhere between $v_{on} = |a|^2$ and $v_{off} = \max|c|^2$ has to be set in order for a decision to be made. An error occurs when a match falls below the threshold or when

a mismatch exceeds the threshold due to the noise on the incoming pattern. One common approach to quantify the error is to divide the number of errors occurring over a time interval by the number of pulses transmitted during this interval, which is called the bit-error rate (BER). In the following analysis, the MWH is assumed to be perfect without fabrication errors.

To estimate the bit error rate, we assume each bit b_m of the incoming pattern is an independent random variable with variance σ^2. The output o_n at each port of the 2^N bit correlator can be written as

$$o_n = \frac{1}{\sqrt{2^N}} \sum_{1}^{2^N} c b_m, \tag{3.44}$$

where $c = \pm 1$. The variance of Cb_m, where C is a constant, is C^2 times the variance of b_m; and the variance of the sum of independent random variables is the sum of the individual variances. As a result, the variance of o_n is

$$\left(\frac{\sigma^2}{2^N}\right) 2^N = \sigma^2, \tag{3.45}$$

which is the same as the variance of the individual bit.

By assuming the noise on individual bits has a Gaussian distribution function, the BER can be estimated as [56]

$$BER \approx \frac{1}{\sqrt{2\pi}} \frac{e^{-Q^2/2}}{Q}. \tag{3.46}$$

The parameter Q is defined as

$$Q = \frac{v_{th} - v_{off}}{\sigma_{off}} = \frac{v_{on} - v_{th}}{\sigma_{on}}. \tag{3.47}$$

A Q value of 6 or higher corresponds to a BER of 10^{-9} or less, which is considered to be errorless in telecommunication standards.

For MWH correlators, $\sigma_{on} = \sigma_{off} = \sigma$, we define

$$V = v_{on} - v_{off} = \frac{4(2^N - 1)}{2^N}. \tag{3.48}$$

where (3.41) and (3.42) are used. By setting v_{th} midway between v_{on} and v_{off}, we have from (3.47) and (3.48)

$$Q = \frac{V}{2\sigma} = \frac{2(2^N - 1)}{2^N \sigma}. \tag{3.49}$$

It can be seen that as the pattern length increases, the Q parameter reaches an upper limit $\lim_{N\to\infty} Q = 2/\sigma$ ("2" in the equation because one bit difference in phase modulated pattern causes 2 bits difference in correlation). The amplitude and phase noise of each bit, quantified by σ^2 in our analysis ultimately determines the BER of pattern recognition, which is expected since a ideal correlator is assumed.

3.7.4 BER considering MWH imperfections

From the analysis in section 3.6, we know that the effect of grating cross talk does not affect BER when the length of the hologram is sufficient. Although the lateral shift of the hologram does not significantly affect the discrimination capability, it causes an overall decrease in the diffraction efficiency. The fabrication error and wavelength detuning analyzed in section 3.6 also introduces excess loss. The decrease in diffraction efficiency or excess loss cause the v_{on} signal to fall below the threshold level v_{th}, which is set when the MWH is assumed to be perfect. An error in recognition may result from these losses. Here, we analyze the BER caused by MWH imperfections.

We consider a more general case for both amplitude and phase modulated patterns. For a N bit pattern, the auto-correlation is $v_{on} = |a|^2 = N$; and the cross-correlation with the pattern with one bit difference is $v_{off} = \max|c|^2 = (N-1)^2/N$. The threshold level setting midway between v_{on} and v_{off} is thus

$$v_{th} = \frac{2N^2 - 2N + 1}{2N}. \tag{3.50}$$

The loss L causes v_{on} to decrease to LN, and the corresponding Q defined by (3.47) thus decreases as

$$Q = Q_p \frac{(2L-2)N^2 + 2N - 1}{2N - 1}, \tag{3.51}$$

where Q_p is the Q when the MWH is assumed to be perfect.

Assuming $Q_p = 8$, which corresponds to a BER of 10^{-15}, the degradation of BER for different pattern lengths due to loss is calculated using (3.51) in (3.46) and plotted in Fig. 3.22. From Fig. 3.19 and Fig. 3.20, it can be seen that with this particular material system we analyzed, the excess loss caused by small lateral hologram shift, fabrication error, and wavelength detuning can severely degrade the BER of the correlator. Thus, implementation of MWH correlator in optical communication systems for long pattern correlation is a big challenge using current fabrication technology.

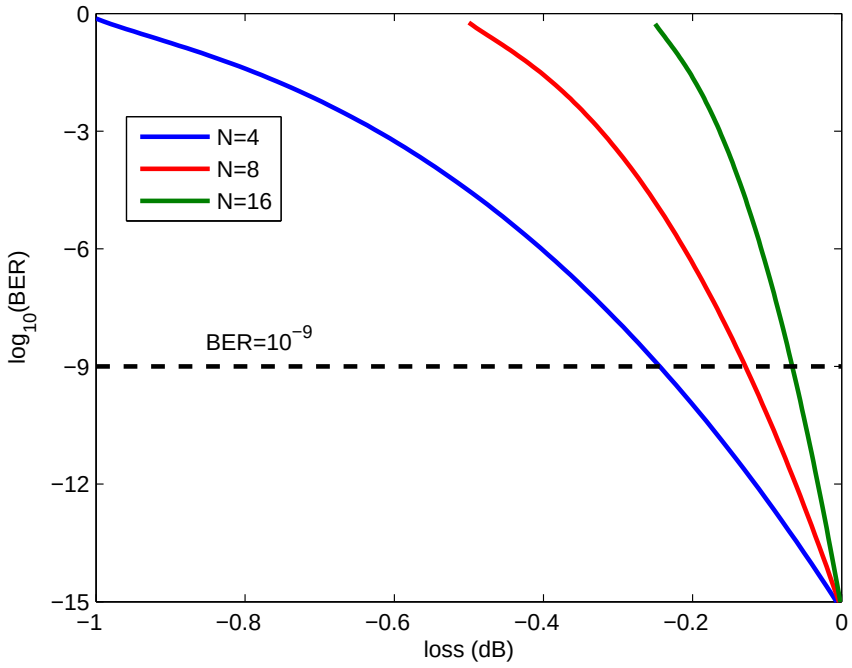

Figure 3.22: Degradation of BER due to loss caused by MWH imperfections.

Chapter 4

Measurement of the third order nonlinearity $\chi^{(3)}$

4.1 Introduction

Using the third-order nonlinear optical properties of materials for optical switching has been an active area of research. The nonlinear index coefficient, n_2, is proportional to the real part of the third order nonlinearity, $\chi^{(3)}_{1111}$ of materials; the imaginary part of $\chi^{(3)}_{1111}$ causes loss due to two photon absorption and limits the effective distance of the waveguide [20]. Knowledge of the phase and magnitude of the nonlinearity of a material is important in determining its device potential. A simple and reliable method to determine the nonlinear optical properties is thus valuable.

Two experimental techniques are commonly used to determine the $\chi^{(3)}$ of materials. A common technique is the Z-scan method [57]. In Z-scan, the transmittance of a sample is measured through a finite aperture as the sample is moved along the propagation path of a focused Gaussian beam. The advantage of the Z-scan technique is that the sign and amplitude of $\chi^{(3)}$ can be deduced from such a transmittance curve. So, it is particularly useful when the nonlinear refraction is accompanied by nonlinear absorption (imaginary part of $\chi^{(3)}$). However, in order to obtain a measurable signal on a thin sample, relatively high intensities and large material nonlinearities are often required. The other technique is the degenerate

four-wave mixing (DFWM) technique [32], which is a sensitive technique for studies of the $\chi^{(3)}$ of nonlinear materials. Typically, the measured signal is proportional to $|\chi^{(3)}|^2$, but the phase of $\chi^{(3)}$ is not available. Additional measurements are needed to determine the real and imaginary parts of $\chi^{(3)}$ using DFWM technique, such as the phase-mismatched DFWM method [58].

In this chapter, a simple optical arrangement for phase sensitive detection of DFWM to characterize the real and imaginary parts of $\chi^{(3)}$ is demonstrated. This technique can potentially improve the sensitivity of the common DFWM technique by using the coherent detection scheme, which, at the same time, offers phase information of the nonlinearity. A processable polyacetylene sample is characterized at a wavelength of 1.5 μm using this technique.

4.2 Degenerate four-wave mixing model

Consider degenerate four wave mixing ($\omega_1 = \omega_2 = \omega_3 = \omega_4 = \omega$) in an isotropic material, the third-order susceptibility with the choice of frequencies given by $\chi_{ijkl}(\omega = \omega_1 + \omega_2 - \omega_3)$ can be represented as [19]

$$\chi_{ijkl}(\omega = \omega + \omega - \omega) = \chi_{1122}(\omega = \omega + \omega - \omega)(\delta_{ij}\delta_{kl} + \delta_{ik}\delta_{jl}) + \chi_{1221}(\omega = \omega + \omega - \omega)(\delta_{il}\delta_{jk}). \tag{4.1}$$

The nonlinear polarization from degenerate four-wave mixing is given by

$$P_i(\omega) = 3\epsilon_0 \sum_{jkl} \chi_{ijkl}(\omega = \omega + \omega - \omega) E_j(\omega) E_k(\omega) E_l(-\omega). \tag{4.2}$$

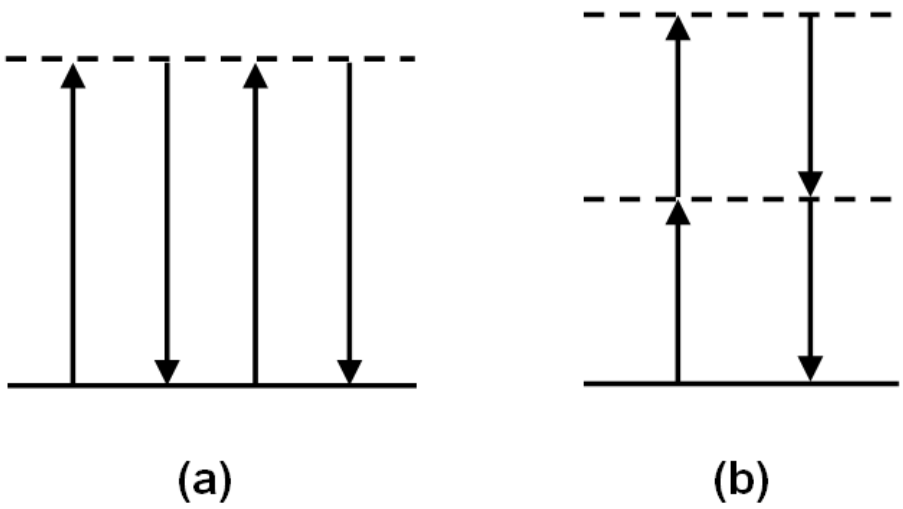

Figure 4.1: Energy level diagrams showing the (a)one photon resonant and (b) two photon resonant contributions to the nonlinear polarization.

Using (4.1) in (4.2), we obtain

$$P_i = 6\epsilon_0\chi_{1122}E_i(\mathbf{E}\cdot\mathbf{E}^*) + 3\epsilon_0\chi_{1221}E_i^*(\mathbf{E}\cdot\mathbf{E}), \tag{4.3}$$

which can be written in vector form as

$$\mathbf{P}_i = 6\epsilon_0\chi_{1122}(\mathbf{E}\cdot\mathbf{E}^*)\mathbf{E} + 3\epsilon_0\chi_{1221}(\mathbf{E}\cdot\mathbf{E})\mathbf{E}^*. \tag{4.4}$$

The two contributions to $\mathbf{P}$ can be represented in terms of energy diagrams in Fig. 4.1. Part (a) shows the one-photon-resonant contribution described by the first term in (4.4). Part (b) shows the two-photon-resonant contribution described by the second term in (4.4).

Now, consider degenerate four-wave mixing with the total field given by

$$\mathbf{E} = \mathbf{E}_1 + \mathbf{E}_2 + \mathbf{E}_3 + \mathbf{E}_4, \tag{4.5}$$

where

$$\begin{aligned}
\mathbf{E}_1(\mathbf{r},t) &= \frac{1}{2}A_1(\mathbf{r})\exp[j(\omega t - \mathbf{k}_1\cdot\mathbf{r})] + c.c. \\
\mathbf{E}_2(\mathbf{r},t) &= \frac{1}{2}A_2(\mathbf{r})\exp[j(\omega t - \mathbf{k}_2\cdot\mathbf{r})] + c.c. \\
\mathbf{E}_3(\mathbf{r},t) &= \frac{1}{2}A_3(\mathbf{r})\exp[j(\omega t - \mathbf{k}_3\cdot\mathbf{r})] + c.c. \\
\mathbf{E}_4(\mathbf{r},t) &= \frac{1}{2}A_4(\mathbf{r})\exp[j(\omega t - \mathbf{k}_4\cdot\mathbf{r})] + c.c.
\end{aligned} \tag{4.6}$$

Phase matching is automatically achieved since

$$\mathbf{k}_4 = \mathbf{k}_1 + \mathbf{k}_2 - \mathbf{k}_3. \tag{4.7}$$

Using (4.5) in (4.4), collecting the phase matched terms, and assuming $\mathbf{E}_4 \ll \mathbf{E}_{1,2,3}$, we obtain the nonlinear polarization in the direction of beam 4

$$\begin{aligned}
\mathbf{P}_4^{NL} &= 3\epsilon_0\chi_{1122}[(\mathbf{E}_3\cdot\mathbf{E}_2^*)\mathbf{E}_1 + (\mathbf{E}_1\cdot\mathbf{E}_2^*)\mathbf{E}_3] + 3\epsilon_0\chi_{1221}(\mathbf{E}_1\cdot\mathbf{E}_3)\mathbf{E}_2^* \\
&= 3\epsilon_0(2\chi_{1122} + \chi_{1221})\mathbf{E}_1\mathbf{E}_2^*\mathbf{E}_3.
\end{aligned} \tag{4.8}$$

When all incident beam polarizations are the same, (4.8) generates a polarization parallel to the field whose scalar amplitude is written as

$$P_4^{NL} = 3\epsilon_0\chi_{1111}E_1E_2^*E_3, \tag{4.9}$$

where $\chi_{1111}^{(3)} = 2\chi_{1122} + \chi_{1221}$ (For simplicity, we'll refer to $\chi_{1111}^{(3)}$ as $\chi^{(3)}$ from now on). This is the third-order nonlinearity measured in our experiment.

Each of the interacting waves obeys the wave equation

$$\nabla^2\mathbf{E} - \mu\epsilon\frac{\partial^2\mathbf{E}}{\partial t^2} = \mu\frac{\partial^2}{\partial t^2}\mathbf{P}^{NL}. \tag{4.10}$$

Substituting (4.9) into (4.10) and making use of the slowly-varying amplitude approximation, we obtain

$$\frac{\mathrm{d}A_4}{\mathrm{d}z} = -j\frac{3\omega}{8cn}\chi^{(3)}A_1A_2^*A_3. \tag{4.11}$$

Assuming the pump beams are undepleted, the DFWM signal, beam 4, after a nonlinear sample of thickness L is thus proportional to

$$I_4 = C\frac{\omega^2}{\epsilon_0^4 n_0^4 c^4}|\chi^{(3)}|^2 L^2 I_1 I_2 I_3 = mI_1 I_2 I_3, \tag{4.12}$$

where C is a proportionality constant.

In our experiment, a reference material with known nonlinearity $\chi^{(3)}_{ref}$ and thickness L_{ref} is first measured to obtain the proportionality constant m_{ref}. Then, the same measurement is carried out on the sample to obtain m_{sam}. By comparing the proportionality constants, m_{ref} and m_{sam}, the absolute value of $\chi^{(3)}_{sam}$ can be calculated as

$$|\chi^{(3)}_{sam}| = |\chi^{(3)}_{ref}|\left(\frac{m_{sam}}{m_{ref}}\right)^{1/2}\frac{L_{ref}}{L_{sam}}\left(\frac{n_{sam}}{n_{ref}}\right)^2. \tag{4.13}$$

4.3 Different Phase-matching geometries of degenerate four-wave mixing (DFWM)

In our experiment, the forward phase-matched geometry as illustrated in Fig. 4.2 is used. With this geometry, the three incident beams (of frequency ω), labeled as 1, 2, and 3 generate the output beam , 4, via $\chi^{(3)}$. The phase matching geometry is similar to the folded BOXCARS arrangement in coherent anti-Stokes Raman spectroscopy (CARS) [59].

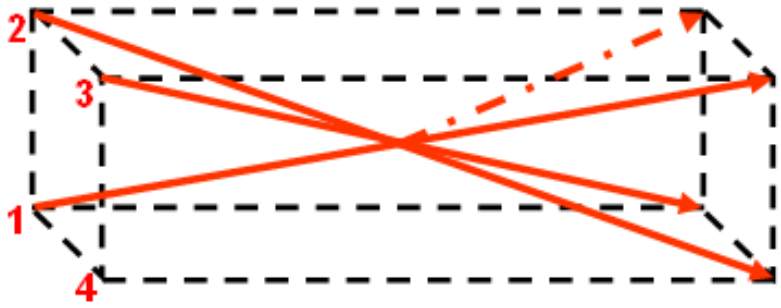

Figure 4.2: Illustration of the forward phase-matched geometry.

In the planar BOXCARS arrangement, the phase matching diagram is illustrated in Fig 4.3. In order to separate the pump and generated beams, it is generally arranged that the pump beams and the generated beam are orthogonally polarized. However, the crossing beams do not need to be coplanar to achieve phase matching. In the folded BOXCARS arrangement as shown in the same figure, the planar BOXCARS phase matching diagram can be folded along the center line, and the phase matching condition can still be maintained. The advantage of this arrangement is that the beams are now completely separated spatially.

The difficulty in implementing this geometry experimentally is to obtain good spatial and temporal overlap of the interacting beams, which usually requires sophisticated setup of beam steering optics and delay lines for spatial and temporal alignment. In our experiment, a 2-D phase grating is designed to generate the beam geometry, which also assures proper spatial and temporal overlap of the interacting beams. A detailed description of the 2-D grating is given in section 4.5. The use of

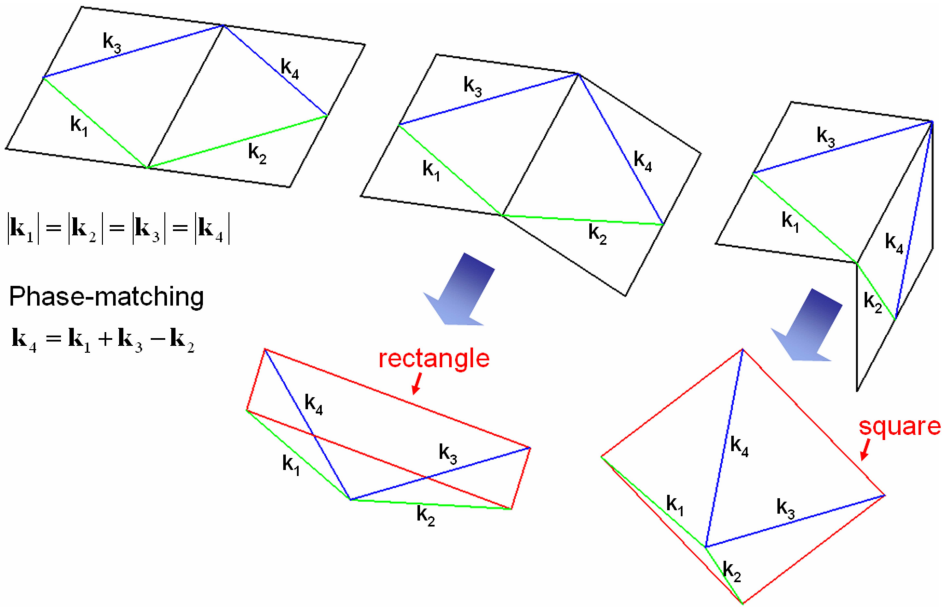

Figure 4.3: Planar and folded BOXCARS phase-matching diagram.

a 2-D phase grating also allows the coherent detection of DFWM which allows the characterization of complex $\chi^{(3)}$. Coherent detection of DFWM is described next.

4.4 Coherent detection of DFWM

As shown in (4.13), only the absolute value of $\chi^{(3)}_{sam}$ can be obtained in the direct DFWM measurement. Also, in the case when the nonlinearity is small, it becomes challenging to detect the weak DFWM signal with good signal-to-noise ratios (SNR's).

Coherent detection has long been recognized as a method to achieve signal amplification [60]. In the coherent detection scheme, a reference field, E_{ref} is mixed coherently with the diffracted DFWM signal, E_{DFWM}, the total intensity on the

detector is

$$I = I_{ref} + I_{DFWM} + 2\sqrt{I_{ref} I_{DFWM}} \cos\theta, \tag{4.14}$$

where θ is the phase difference between the reference field and the DFWM signal. In addition to the improved SNR, another advantage of the coherent detection scheme is that the detected signal is now phase sensitive. By varying the phase of the reference field, the full complex field of the DFWM signal can be measured.

There are difficulties in practical implementation of the coherent detection scheme. One of the problems is that the reference and the DFWM beams have to be overlapped temporally and spatially, which requires careful alignment. A more challenging problem is to stabilize the relative phase between the reference and the DFWM beams. In general, active stabilization with feedback control is used to ensure phase stability [60]. However, the disadvantage is the considerable complexity and added cost over the direct detection scheme.

4.5 Coherent detection using diffractive optical elements

Recently, optical heterodyne detection spectroscopy using diffractive optical elements for passive phase stabilization has been proposed and demonstrated by several groups [61]-[63]. A typical schematic of this technique is shown in Fig. 4.4. In these schemes, one pump beam and one probe beam either angle or wavelength separated are incident on a 1-D diffraction grating to generate the required beam geometry using the ± 1 diffraction order. The beams are then imaged on to the sample with transmission or reflective optics with the other diffraction orders blocked.

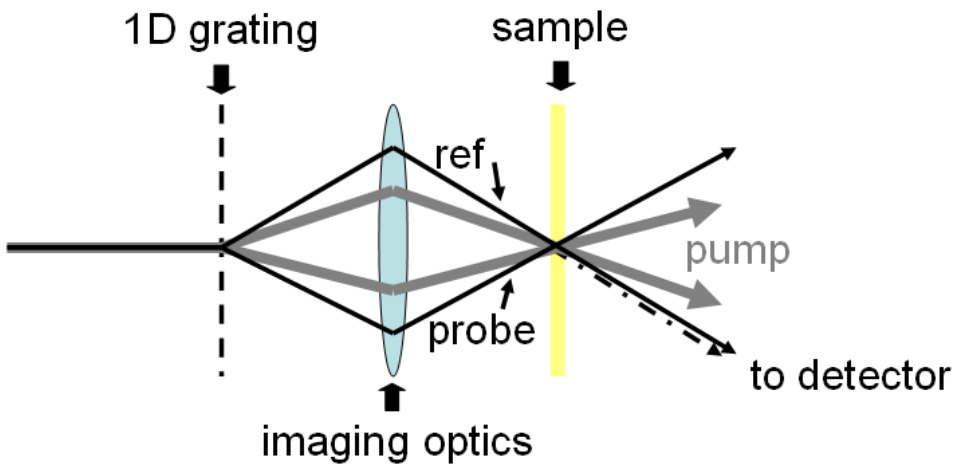

Figure 4.4: Optical arrangement for heterodyne detection spectroscopy.

The use of diffractive optics ensures the spatial overlap of the interacting beams automatically. The stabilization of the phase between the reference and diffracted beams is achieved passively without any additional components, and the spatial and temporal overlap of the reference and diffracted beams is also obtained without the need of additional alignment.

4.6 2-D phase grating

In our experiment, a 2-D phase grating is designed to generate the four beams required for coherent detection of DFWM signal. The schematic of the 2-D grating is illustrated in Fig. 4.5. The phase shift between adjacent grating elements is π such that most of the diffracted beams go into the ($\pm$1,$\pm$1) orders and the (0,0) order is suppressed. Fig. 4.6 shows the calculated diffraction pattern of the 2-D phase grating in Fig. 4.5, it can be seen that the (0,0) order is completely suppressed and most of the power is equally diffracted into the ($\pm$1,$\pm$1) orders as expected.

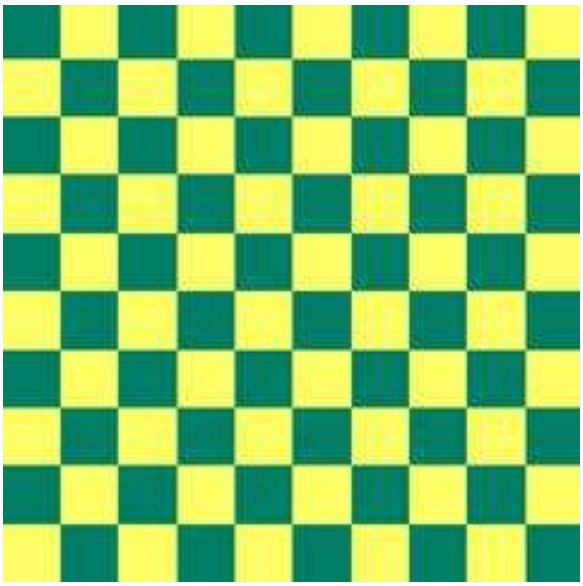

Figure 4.5: Schematic of the 2-D grating used in the experiment. The relative phase between adjacent grating element is π.

The four beams in the ($\pm$1,$\pm$1) orders form the required beam geometry for our experiment.

The 2-D grating fabricated on fused silica is shown in Fig. 4.7. The diffraction pattern probed with a He-Ne laser is shown in Fig. 4.8. Since the probe laser is far from our design wavelength of 1.5 μm, the phase shift between adjacent grating elements is no longer π and strong (0,0) order can be seen in the picture. We measured the diffraction efficiency into the ($\pm$1,$\pm$1) orders using a CW laser at 1.5 μm and found the efficiency to be around 70% (total power in the four ($\pm$1,$\pm$1) order beams).

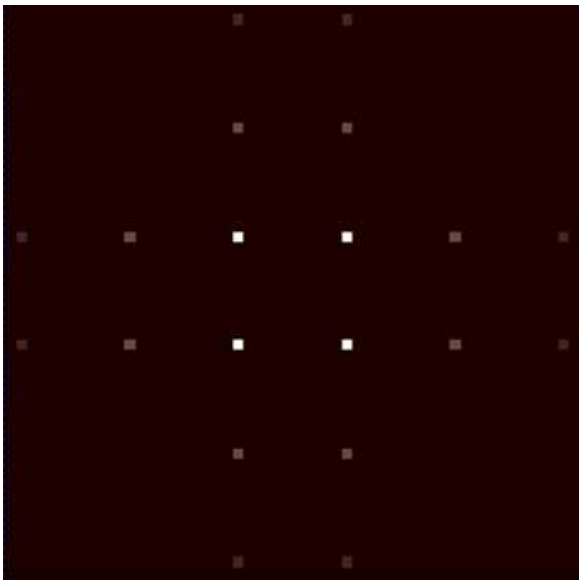

Figure 4.6: Calculated diffraction pattern of the grating in figure 3.4

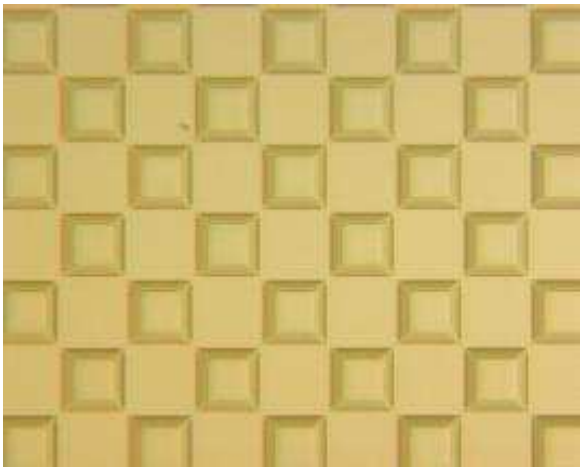

Figure 4.7: 2-D diffraction grating fabricated on fused silica.

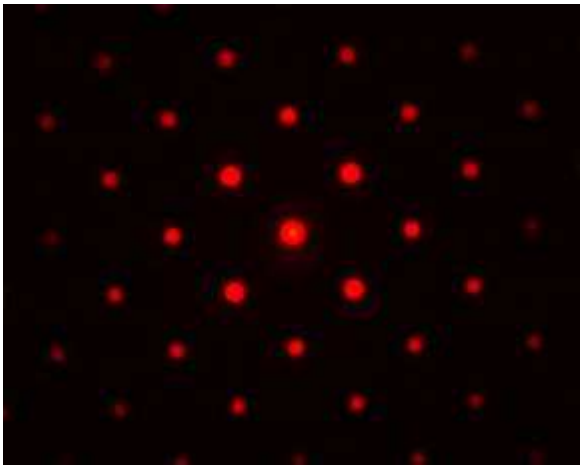

Figure 4.8: The diffraction pattern of HeNe laser scattered by the 2-D grating in Fig. 4.7

4.7 Measurement of $\chi^{(3)}$

4.7.1 Experimental setup

The schematic of the experimental setup for direct detection of DFWM signal is illustrated in Fig. 4.9. The schematic for coherent detection is similar to this schematic and will be described in later sections. The laser source used in the experiment is an OPA (Spectra-Physics OPA800-C) pumped by a regenerative Ti:sapphire amplifier (Spectra-Physics Hurricane system). The system generates 130 fs output pulses at 1525 nm with a repetition rate of 1 kHz. A half-wave plate and a polarizer are used to control the light intensity into the DFWM experimental setup. A small amount of the beam is deflected onto a photodetector before entering the setup to monitor the input power. The beam is focused onto the 2-D phase grating with grating period 40 μm using a spherical lens with 20 cm focal length. After the 2-D grating, the beam is diffracted into four replicas (±1,±1 diffraction orders) with

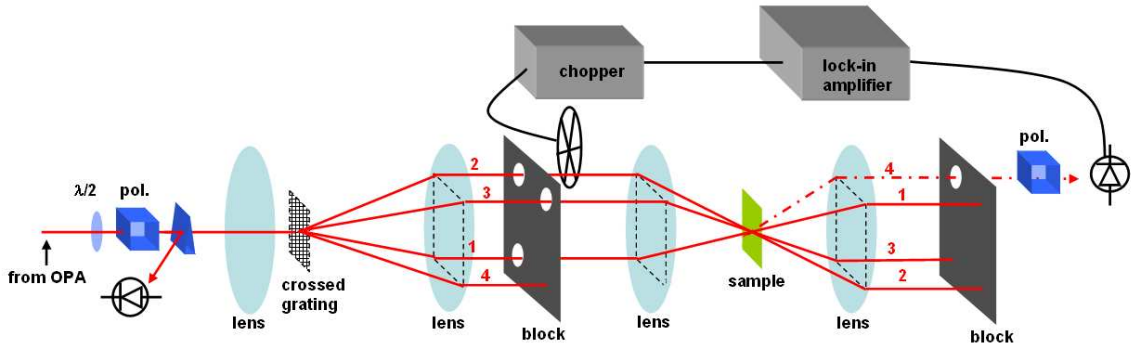

Figure 4.9: Schematic of the Direct detection of $|\chi^{(3)}|$.

70% efficiency. All the other diffractive orders are blocked with a mask. The beams are arranged in the folded-BOXCARS geometry and are 1X imaged onto the sample with the telescope consisting of two identical spherical lenses with 10 cm focal lengths. Beam 2 is chopped at 500 Hz before the sample to eliminate pump-probe contamination [63]. The use of a 2-D phase grating ensures both phase matching and the spatial and temporal overlap of the DFWM signal and the reference field. After the sample, a spherical lens with 10 cm focal length is used to collimate the beams. By blocking the unwanted beams and scattered light, only the reference beam and the DFWM is allowed into the detection system consisting of a polarizer and a photodetector. The electrical signal from the photodetector is sent into a lock-in amplifier which is phase-locked with the optical chopper. In this experiment, a 520 μm thick fused silica is chosen as the reference material for comparison with the nonlinear polymer sample. The $\chi^{(3)}$ of fused silica has been well characterized to be 1.5×10^{-14} esu [64][65].

4.7.2 Direct detection of $|\chi^{(3)}|$

In the direct detection experiment (Fig. 4.9), the reference field (beam 4) is blocked before the sample, and the DFWM signal is generated in the direction of beam 4 with an intensity proportional to $|\chi^{(3)}|^2 I_1 I_2 I_3$. In traditional DFWM experiment, locating the direction of the DFWM signal is challenging since the signal is weak. In our experimental setup, since the DFWM is generated collinearly with beam 4, by simply unblocking beam 4, the detection system can be easily aligned, and irises can be placed accurately to block the unwanted beams and scattered light. The DFWM signal of a 100 μm thick processable polyacetylene polymer provided by the Georgia Tech Department of Chemistry (Joseph Perry, Seth Marder, and Joel Hales) is measured and compared to a fused silica reference. Fig. 4.10 shows the cubic dependence of the DFWM signal to the input beam intensity. The magnitude, $|\chi^{(3)}|$, of the nonlinear polymer is calculated to be $(7.0 \pm 0.05) \times 10^{-11}$ esu from the measurement.

4.7.3 Coherent detection of $\chi^{(3)}$

The experimental arrangement used for coherent detection of $\chi^{(3)}$ is illustrated in Fig. 4.11. In the coherent detection experiment, the reference field (beam 4) is unblocked and mixed with the DFWM signal on the detector. A 150 μm thick cover slip (CS-1) is mounted on a rotation stage and inserted into the path of the reference field to control the relative phase between reference and signal. An additional cover slip (CS-2) and half-wave plates are inserted into the beam paths to ensure the

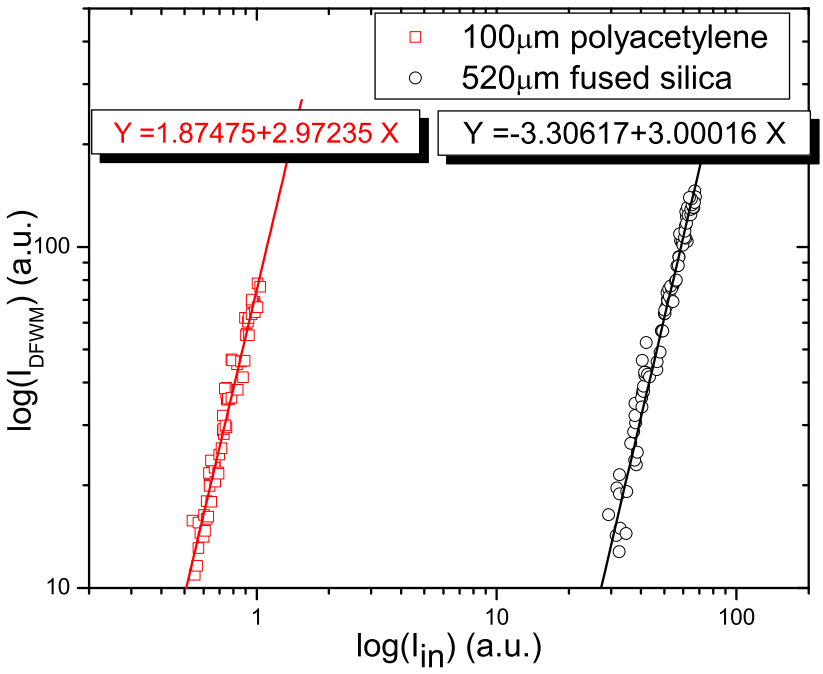

Figure 4.10: Cubic dependence of the DFWM signal of polyacetylene and fused silica to the input intensity.

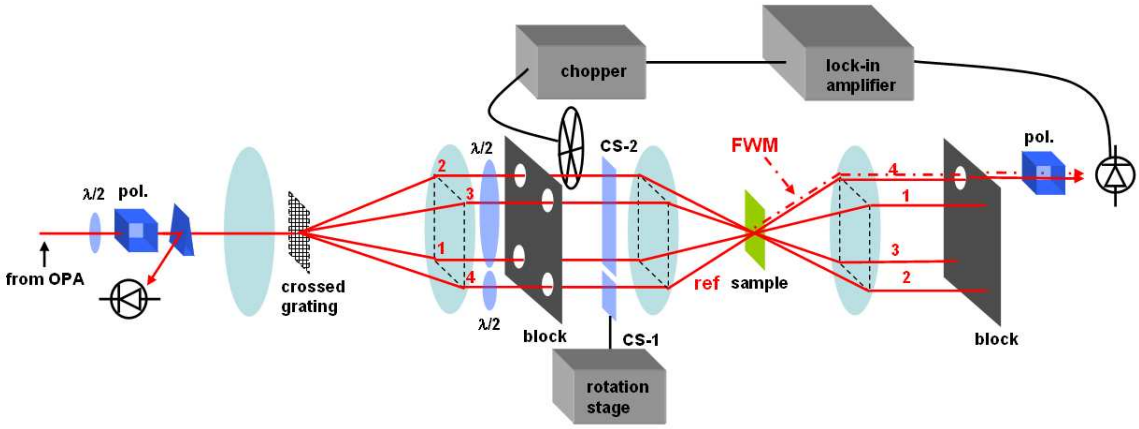

Figure 4.11: Schematic of the coherent detection of $\chi^{(3)}$.

proper temporal overlap and to adjust the intensity of the reference and signal beams on the detector.

Using 4.14, the coherent detection signal can be described by the following equation,

$$I = I_{DFWM} + I_{ref} + 2\sqrt{I_{DFWM} + I_{ref}}\cos(\theta_i + \Delta\theta). \tag{4.15}$$

$\Delta\theta$ is the phase difference between reference and signal due to cover slip rotation and $\theta_i = \theta_0 + \phi_i$, where $\chi^{(3)} = |\chi^{(3)}|\exp(j\phi_i)$. The DC signal I_{ref} is removed by chopping beam 2. Rotation of the cover slip changes the path lengths of the reference beam in air and in cover slip as shown in Fig. 4.12, which introduces phase difference between the reference and signal beams. The phase difference $\Delta\theta$ is related to the cover slip rotation angle by [66]

$$\Delta\theta = \frac{2\pi d}{\lambda}\left[n_{cs}\left(\frac{1}{\cos\beta} - \frac{1}{\cos\beta_0}\right) - n_a\left(\frac{\cos(\alpha-\beta)}{\cos\beta} - \frac{\cos(\alpha_0-\beta_0)}{\cos\beta_0}\right)\right], \tag{4.16}$$

where n_{cs} is the refractive index of the cover slip, n_a is the refractive index of air, d is the cover slip thickness, λ is the wavelength, α and β are the incident and

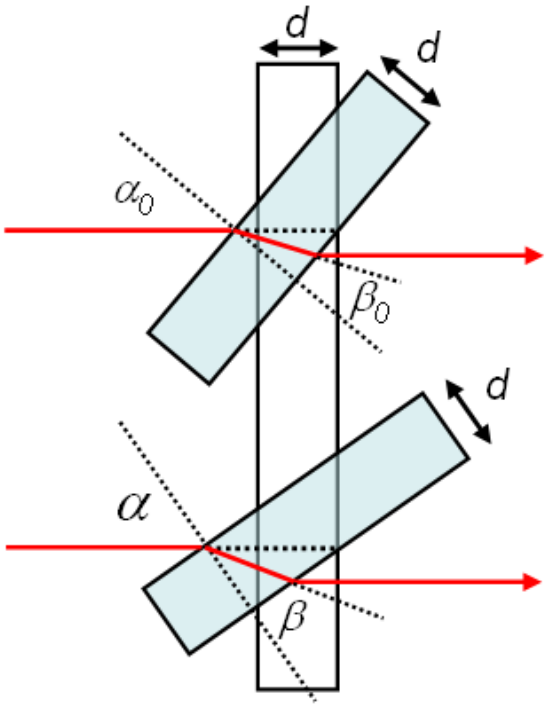

Figure 4.12: Path length difference introduced by cover slip rotation.

transmission angles at the air and cover slip interface and are related by $n_a \sin\alpha = n_{cs} \sin\beta$.

The interference signals of the polyacetylene film and the reference fused silica are plotted and fit with the above expressions in Fig. 4.13. The phase of the nonlinear polymer is calculated to be 21.0°±1.2° by comparing the fit parameters.

4.8 Nonlinear refractive index, nonlinearity coefficient, and nonlinear absorption coefficient

The third order nonlinearity $\chi^{(3)}$ is responsible for the nonlinear refractive index which can be used for ultrafast switching as described in chapter 1. In the

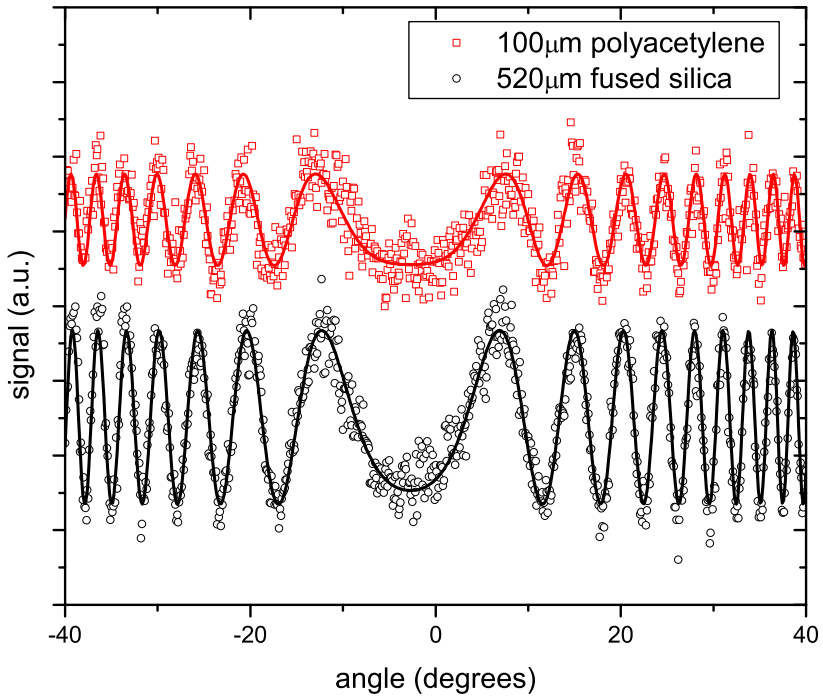

Figure 4.13: Interferograms of the coherent detected DFWM signals of polyacetylene and fused silica.

literature, the nonlinearity is usually quantified in terms of nonlinear refractive index n_2 or in terms of nonlinearity coefficient γ, and the nonlinear absorption is quantified by the two-photon absorption coefficient α_2. In this section, the relation between these quantities are summarized.

The nonlinear refractive index n_2 is defined as

$$n = n_0 + n_2 I, \tag{4.17}$$

where n_0 is the linear refractive index and I is the intensity of the optical field. The parameter n_2 has units of m^2/W and is related to the real part of $\chi^{(3)}$ as [20]

$$n_2 = \frac{3\mathrm{Re}\chi^{(3)}}{4\epsilon_0 c n_0^2}. \tag{4.18}$$

Here, $\epsilon_0 = 8.8542 \times 10^{-12}$ F/m and $c = 2.998 \times 10^8$ m/s. Normally, $\chi^{(3)}$ is measured in the electrostatic units (esu) and can be converted in SI units as

$$\chi^{(3)}\left[\frac{\mathrm{m}^2}{\mathrm{V}^2}\right] = \left(\frac{4\pi}{9} \cdot 10^{-8}\right) \chi^{(3)}[\mathrm{esu}]. \tag{4.19}$$

With this, n_2 is related to $\chi^{(3)}$ as

$$n_2\left[\frac{\mathrm{m}^2}{\mathrm{W}}\right] = \frac{\pi}{3\epsilon_0 c n_0^2} 10^{-8} \mathrm{Re}\chi^{(3)}[\mathrm{esu}]. \tag{4.20}$$

For nonlinearity in optical fibers, it is customary to evaluate the nonlinearity using the nonlinearity coefficient γ ($\mathrm{W}^{-1}\mathrm{km}^{-1}$), which is defined by

$$\gamma = \frac{n_2 \omega_0}{c A_{eff}}, \tag{4.21}$$

where A_{eff} is the effective core area and is normally in the range of 50-80 $\mu\mathrm{m}^2$ for optical fibers in the 1.5 μm region [20]. The corresponding nonlinearity coefficient can vary from 2-30 $\mathrm{W}^{-1}\mathrm{km}^{-1}$ if we use $n_2 \approx 3 \times 10^{-20}$ m^2/W [65].

Similarly, the two-photon absorption coefficient is defined as

$$\alpha = \alpha_0 + \alpha_2 I, \tag{4.22}$$

where α_0 is the linear absorption coefficient. The parameter α_2 has units of m/W and is related to the imaginary part of $\chi^{(3)}$ as [20]

$$\alpha_2 = \frac{3\omega \mathrm{Im}\chi^{(3)}}{2\epsilon_0 c^2 n_0^2}. \tag{4.23}$$

When α_2 is measured in the electrostatic units, it is related to $\chi^{(3)}$ as

$$\alpha_2 \left[\frac{\mathrm{m}}{\mathrm{W}}\right] = \frac{2\pi\omega}{3\epsilon_0 c^2 n_0^2} 10^{-8} \mathrm{Im}\chi^{(3)}[\mathrm{esu}]. \tag{4.24}$$

From the magnitude and phase of the measured $\chi^{(3)}$ of the polyacetylene sample, we calculated the n_2 to be 5.3×10^{-17} (m^2/W), and the α_2 to be 1.7×10^{-10} (m/W). Previous switching experiments using common dispersion shifted fibers [29][30] require several kilometers of fibers for sufficient nonlinearity. A recent switching experiment [31] using highly nonlinear fiber with γ=1100$\mathrm{W}^{-1}\mathrm{km}^{-1}$ requires only 2 meters of fiber. With the polyacetylene measured in the experiment, the length can be further reduced from meters by a factor of 10. Another factor of 10 can be obtained by the reduction of waveguide dimension. However, it is still insufficient for integrated components.

A more realistic figure of merit taken into account of two-photon absorption can be obtained as follows. For a third-order nonlinear material to provide a useful phase change before light is substantially absorbed, it is essential that the two-photon figure of merit $T = \alpha_2 \lambda / n_2$ be less than 1 [67]. For the polyacetylene

sample, the figure of merit T is calculated to be 4.8, which is insufficient for photonic switching applications.

4.9 Discussion on DFWM measurement using 2-D phase grating

DFWM measurement using 2-D phase grating combines both the sensitivity of DFWM scheme and the passive phase stability using diffractive optical elements. This setup is applicable over a wide wavelength range as long as enough power is obtained in the $(\pm 1, \pm 1)$ orders. The spatial and temporal overlap can be obtained easily.

This setup does not provide time-resolved nonlinearity information, which can be obtained in sophisticated systems with optical delays. In the experiment, the insertion of a 150 μm cover slip into any one or two of the interacting beams eliminates the DFWM signal completely, which ensures no slow effects is present. To completely identify the individual χ_{ijkl} components in (4.4), individual control of the polarization of interacting beams is needed [58]. To implement individual polarization control in the current setup is difficult since the spacing between the interacting beams is only $\sim$ 1 cm.

Chapter 5

Optical switching using cross-phase modulation (XPM) in semiconductor optical amplifiers (SOAs)

5.1 Introduction

Optical switching using optical nonlinearities is very important for optical signal processing applications. The nonlinearity of SOAs has been exploited for optical switching by many researchers [68]-[70]. In order to achieve ultrafast switching in SOAs, it is necessary to eliminate the problem of slow relaxation in semiconductors. In this chapter, we demonstrate a simple configuration for ultrafast switching in segmented SOAs. We start with a theoretical description of nonlinear pulse propagation in nonlinear waveguides; the nonlinearity in SOA is then introduced; and the experiment and modeling of the switch are presented.

5.2 Nonlinear pulse propagation in single mode optical waveguide

The electric field of a pulse in a single mode nonlinear optical waveguide can be written as

$$E(x, y, z, t) = \phi(x, y)A(z, t)\exp[-j(\beta_0 z - \omega_0 t)] + \text{c.c.}, \tag{5.1}$$

where ϕ is the waveguide mode, $\beta_0 = n(\omega_0)\omega_0/c$, and A is the slowly varying envelope of the pulse. The electric field obeys the wave equation

$$\nabla^2 E - \mu_0 \frac{\partial^2 D}{\partial t^2} = 0, \tag{5.2}$$

where D represents the total displacement field, including both the linear and nonlinear contributions. Now, we introduce the Fourier transforms of $E(z,t)$ and $D(z,t)$ as in ref. [19]

$$E(z,t) = \int_{-\infty}^{\infty} \tilde{E}(z,\omega) \exp(j\omega t) \frac{\mathrm{d}\omega}{2\pi}, \tag{5.3}$$

$$D(z,t) = \int_{-\infty}^{\infty} \tilde{D}(z,\omega) \exp(j\omega t) \frac{\mathrm{d}\omega}{2\pi}. \tag{5.4}$$

The Fourier components $\tilde{E}(z,\omega)$ and $\tilde{D}(z,\omega)$ are related by,

$$\tilde{D}(z,\omega) = \epsilon(\omega)\tilde{E}(z,\omega), \tag{5.5}$$

where the dielectric constant describes both the linear and nonlinear contributions.

In the frequency domain, the wave equation becomes

$$\nabla^2 \tilde{E} + \frac{\omega^2}{c^2} \frac{\epsilon(\omega)}{\epsilon_0} \tilde{E}(z,\omega) = 0. \tag{5.6}$$

This equation can be written in terms of the Fourier component of $A(z,t)$, which is given by

$$\tilde{A}(z,\omega') = \int_{-\infty}^{\infty} A(z,t) \exp(-j\omega' t) \mathrm{d}t, \tag{5.7}$$

and is related to $\tilde{E}(z,\omega)$ by

$$\tilde{E}(z,\omega) \simeq \phi(x,y)\tilde{A}(z,\omega-\omega_0) \exp(-j\beta_0 z). \tag{5.8}$$

Substituting (5.8) into (5.6) and dropping the $\partial^2/\partial z^2$ term, we obtain the following two equations for ϕ and $\tilde{A}$

$$\nabla_\perp^2 \phi + \left(\frac{\omega^2}{c^2} \frac{\epsilon}{\epsilon_0} - \beta_0^2 \right) \phi = 0, \tag{5.9}$$

and

$$-2j\beta_0 \frac{\partial \tilde{A}}{\partial z} + (\beta^2 - \beta_0^2)\tilde{A} = 0. \tag{5.10}$$

Eq. (5.9) is the eigenvalue equation that gives the mode profile ϕ of the waveguide. The propagation constant β can be solved using first-order perturbation theory.

Since β only differs from β_0 by a small amount, we can approximate (5.10) as

$$\frac{\tilde{A}(z, \omega - \omega_0)}{\partial z} + j(\beta - \beta_0)\tilde{A}(z, \omega - \omega_0) = 0. \tag{5.11}$$

The propagation constant β can be expanded as

$$\beta = \beta_0 + \Delta\beta_{NL} + \beta_1(\omega - \omega_0) + \frac{1}{2}\beta_2(\omega - \omega_0)^2 + \cdots, \tag{5.12}$$

where $\Delta\beta_{NL}$ is the nonlinear contribution to the propagation constant. In (5.12), β_1 is the reciprocal of the group velocity, and β_2 is the dispersion of the group velocity as

$$\beta_1 = \left. \frac{\mathrm{d}\beta}{\mathrm{d}\omega} \right|_{\omega=\omega_0} \equiv \frac{1}{v_g(\omega_0)}, \tag{5.13}$$

$$\beta_2 = \left. \frac{\mathrm{d}^2\beta}{\mathrm{d}\omega^2} \right|_{\omega=\omega_0} = -\frac{1}{v_g} \left. \frac{\mathrm{d}v_g}{\mathrm{d}\omega} \right|_{\omega=\omega_0}. \tag{5.14}$$

Introducing (5.12) into (5.11), we obtain

$$\frac{\partial \tilde{A}}{\partial z} + j\Delta\beta_{NL}\tilde{A} + j\beta_1(\omega - \omega_0)\tilde{A} + \frac{1}{2}j\beta_2(\omega - \omega_0)^2\tilde{A} = 0. \tag{5.15}$$

By transforming this equation from the frequency domain to the time domain, we obtain the pulse propagation equation:

$$\frac{\partial A}{\partial z} + \beta_1 \frac{\partial A}{\partial t} + \frac{1}{2} j\beta_2 \frac{\partial^2 A}{\partial t^2} - j\Delta\beta_{NL} A = 0. \tag{5.16}$$

In the next section, we discuss the nonlinear contribution to $\Delta\beta_{NL}$ from nonlinearities in SOAs.

5.3 Pulse propagation in semiconductor optical amplifiers

In semiconductor optical amplifiers (SOAs), the medium response to the optical field is described by the carrier density rate equation [18]

$$\frac{\partial N}{\partial t} = D\nabla^2 N + \frac{I}{qV} - \frac{N}{\tau_c} - \frac{a(N - N_0)}{\hbar\omega_0} |E|^2, \tag{5.17}$$

where N is the carrier density, D is the diffusion coefficient, I is the injection current, q is the electron charge, V is the active volume, τ_c is the spontaneous carrier lifetime, $\hbar\omega$ is the photon energy, a is the gain coefficient, and N_0 is the transparency carrier density.

The dielectric constant ϵ is given by

$$\epsilon = \epsilon_0 (n_b^2 + \chi), \tag{5.18}$$

where n_b is the background index accounting for dielectric waveguiding in SOAs. The nonlinear susceptibility χ represents the gain of the material due to carrier injection and is generally a complex number. The imaginary part is related to the gain/loss in the SOA, and the real part accounts for the phase shift. A simple

phenomenological model is used to describe the complicated relation between the carrier density N and χ. In this model, the relation between χ and N is given by

$$\chi(N) = -\frac{\bar{n}c}{\omega_0}(\alpha + j)a(N - N_0), \tag{5.19}$$

where $\bar{n}$ is the effective mode index, and the linewidth enhancement factor α accounts for the carrier induced index change.

The susceptibility χ contributes a nonlinear term $\Delta\beta_{NL}$ to the propagation constant (5.12). The nonlinear contribution is

$$\Delta\beta_{NL} = \frac{\omega_0\Gamma}{2\bar{n}c}\chi, \tag{5.20}$$

where Γ is the optical confinement factor defined by the fraction of optical energy inside the active region. By neglecting the group velocity dispersion term in (5.16), the equation describing pulse propagation in SOA is then

$$\frac{\partial A}{\partial z} + \frac{1}{v_g}\frac{\partial A}{\partial t} = j\frac{\omega_0\Gamma}{2\bar{n}c}\chi A - \frac{1}{2}\alpha_{loss}A, \tag{5.21}$$

where α_{loss} is the waveguide loss.

By neglecting carrier diffusion and averaging (5.17) over the active region, the carrier-density rate equation is simplified to

$$\frac{\partial N}{\partial t} = \frac{I}{qV} - \frac{N}{\tau_c} - \frac{g(N)}{\hbar\omega_0}|A|^2, \tag{5.22}$$

where the gain is defined by

$$g(N) = \Gamma a(N - N_0). \tag{5.23}$$

Combining (5.22) and (5.23), we obtain

$$\frac{\partial g}{\partial t} = \frac{g_0 - g}{\tau_c} - \frac{g|A|^2}{E_{sat}}, \tag{5.24}$$

where $E_{sat} = \hbar\omega_0\sigma/a$ is the saturation energy of the amplifier, and σ is the mode cross section ($\sigma = wd/\Gamma$). The small-signal gain is defined by

$$g_0 = \Gamma\sigma N_0(\frac{I}{I_0} - 1), \tag{5.25}$$

where $I_0 = qVN_0/\tau_c$ is the transparency current.

Since A in (5.21) represents the power, we can write A in terms of the amplitude and phase as $A = \sqrt{P}\exp(j\theta)$, where $P(z,t)$ and $\theta(z,t)$ are the amplitude and phase, respectively. Combining (5.21) through (5.24), and transforming to a reference frame moving with the pulse, $\tau = t - z/v_g$, we obtain the following set of equations describing nonlinear pulse propagation in SOAs:

$$\frac{\partial P}{\partial z} = (g - \alpha_{loss})P, \tag{5.26}$$

$$\frac{\partial \theta}{\partial z} = -\frac{1}{2}\alpha g, \tag{5.27}$$

$$\frac{\partial g}{\partial t} = \frac{g_0 - g}{\tau_c} - \frac{gP}{E_{sat}}. \tag{5.28}$$

Eq. (5.27) shows the origin of the self-phase modulation (SPM) and cross-phase modulation (XPM). The time dependence of the gain $g(z,\tau)$ leads to a temporal modulation of the phase. The gain saturation and recovery is described by (5.28).

When waveguide loss is negligible, (5.26)-(5.28) can be solved in a closed form as follows. (5.26) and (5.28) can be integrated over the length of the amplifier L to obtain

$$P_{out}(\tau) = P_{in}(\tau)\exp[h(\tau)] \tag{5.29}$$

$$\theta_{out}(\tau) = \theta_{in} - \frac{1}{2}\alpha h(\tau), \tag{5.30}$$

where $h(\tau)$ is the integrated gain over the pulse profile and can be written as

$$h(\tau) = \int_0^L g(z,\tau)\mathrm{d}z. \tag{5.31}$$

Integrating (5.28), we obtain the following differential equation for $h(\tau)$,

$$\frac{\mathrm{d}h}{\mathrm{d}\tau} = \frac{g_0 L - h}{\tau_c} - \frac{P_{in}(\tau)}{E_{sat}}[\exp(h) - 1]. \tag{5.32}$$

The output pulse can then be obtained by solving for the gain (5.32) numerically, and then applying the solution to the input pulse profile P_{in}.

Using typical parameters for SOAs, we simulated the propagation of a 2.77 ps (full width at half maximum, FWHM) Gaussian pulse in a SOA with 32.4 dB gain by solving (5.26)-(5.28). The time dependent gain and phase shift are illustrated in Fig. 5.1. It can be seen in Fig. 5.1(a) that the gain is quickly saturated within the duration of the pulse, and then slowly recovers with time constant τ_c. From (5.27), we know that the gain saturation of the amplifier by the pulse is accompanied by a phase shift as illustrated in Fig. 5.1(b). The phase shift is the result of the increase in refractive index caused by the decrease of carrier density as the gain saturates.

5.4 Optical switching using XPM in SOAs

5.4.1 Operating principle

Now, we consider a optical switch with control pulses (strong) and signal pulses (weak) of different wavelengths propagating in the SOA as illustrated in Fig. 5.2. As the gain is saturated by the control pulse, the refractive index seen by the signal pulse increases. The phase change consists of a fast saturation within the duration

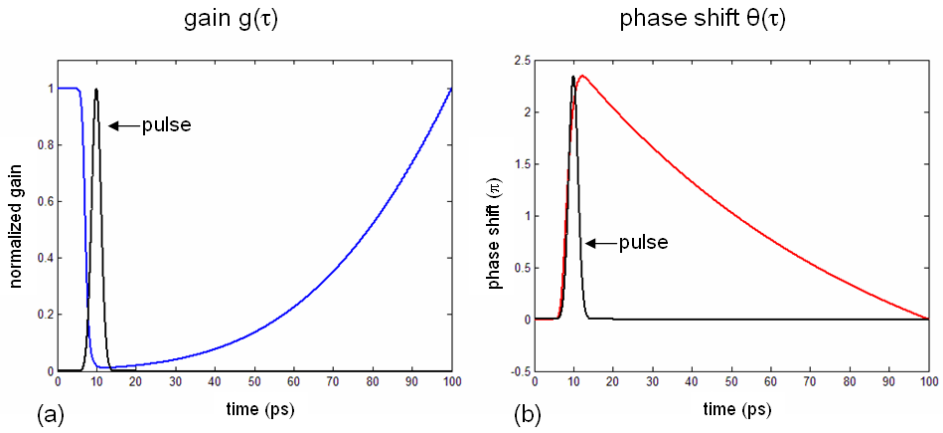

Figure 5.1: The time dependent gain (a) and phase shift (b) of a SOA with a 2.77 ps pump pulse.

of the control pulse and a slow recovery as illustrated in Fig. 5.1. If the pulse width are much shorter than the carrier lifetime τ_c, we can ignore the frequency shift resulting from the slow recovery. Focusing on the fast increase of phase, such a monotonic change in phase is equivalent to a red shift in the signal light frequency described by the chirp

$$\Delta\omega(\tau) = \frac{\mathrm{d}\theta}{\mathrm{d}\tau}. \tag{5.33}$$

Thus, when the control pulse is aligned with the signal pulse, the signal pulse is shifted to longer wavelength. With a filter aligned with the shifted spectrum, the signal pulses with or without frequency shift can be selected. In this scheme, the switching time is not limited by the slow recovery time of the SOA.

5.4.2 Experiment on XPM in SOAs

To experimentally demonstrate this principle of operation, a CW laser is used as the probe light, and a mode-locked (ML) semiconductor laser is used as the pump

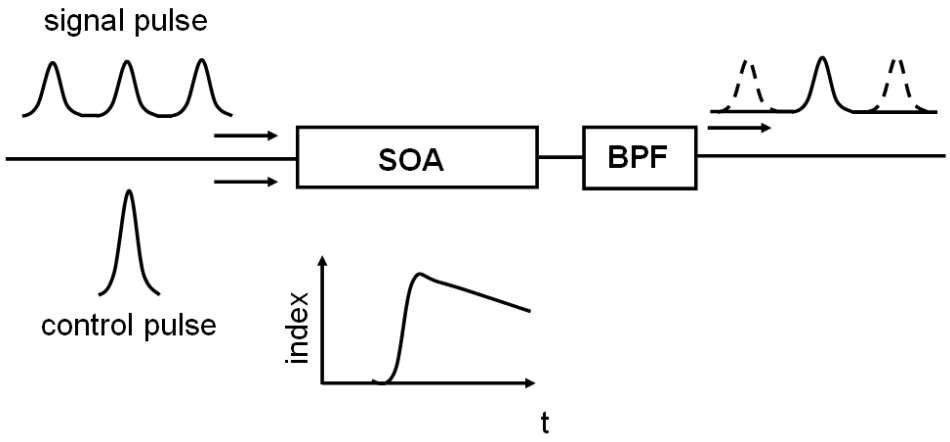

Figure 5.2: Schematic of a optical switch using XPM in SOA.

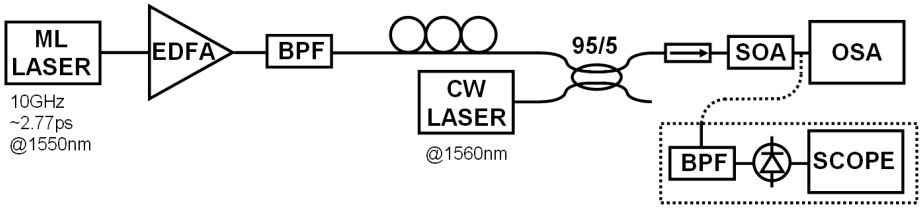

Figure 5.3: Experimental setup for characterizing the XPM induced frequency shift in SOA.

light as illustrated in Fig. 5.3. ML laser generates pulses with pulse width of 2.77 ps (FWHM) with a repetition rate at around 10 GHz at a wavelength of 1550 nm. The wavelength of the CW laser is 1560 nm. To ensure the four-wave mixing product is negligible, the wavelength separation of the pump and probe light has to be large enough so that the inverse of the beating frequency between the two field is much smaller than the carrier lifetime.

The amplitude and phase of the CW laser are modulated by the time dependent gain and phase similar to Fig. 5.1 caused by the pump pulse. The measured modulated CW output using a 45 GHz optical detector is shown in Fig. 5.4. The

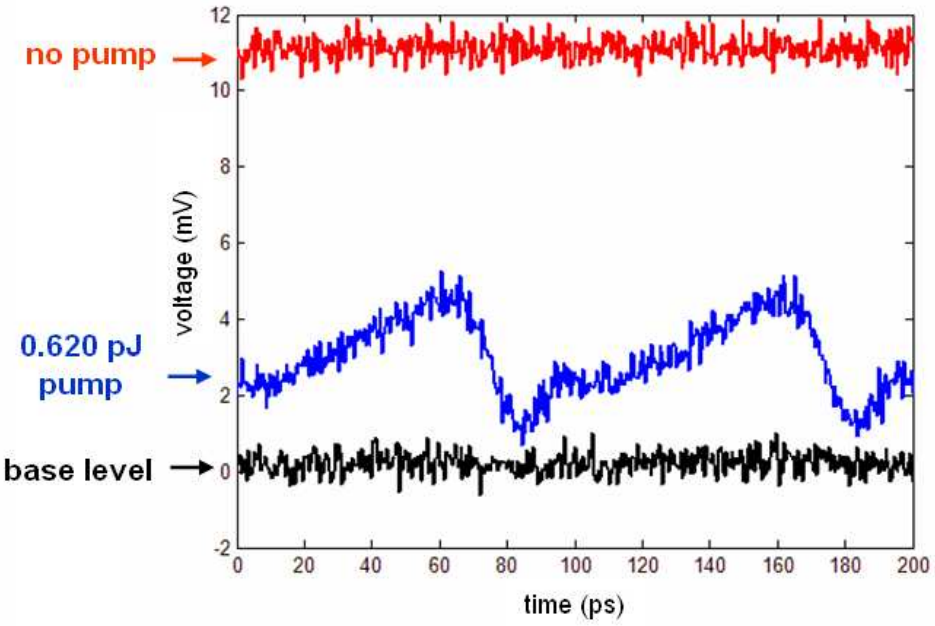

Figure 5.4: The modulated CW output resulting from XGM in a commercial SOA.

fast saturation of the gain and the slow recovery is evident in the figure. It can been seen in the figure that additional structure exists at the bottom of the gain saturation curve. These features can be explained by the ultrafast phenomena including carrier heating, spectral hole burning, and two photon absorption [71]. The spectrum of the modulated CW light at different pump powers is shown in Fig. 5.5. As predicted by theory, the spectrum is broadened by the XPM effect. A significant red shift can be seen in the figure which is attributed to the fast saturation; and the overall spectrum is blue shifted due to the slow recovery. The additional feature in the blue shifted part of the spectrum can be explained by the ultrafast phenomenon mentioned above.

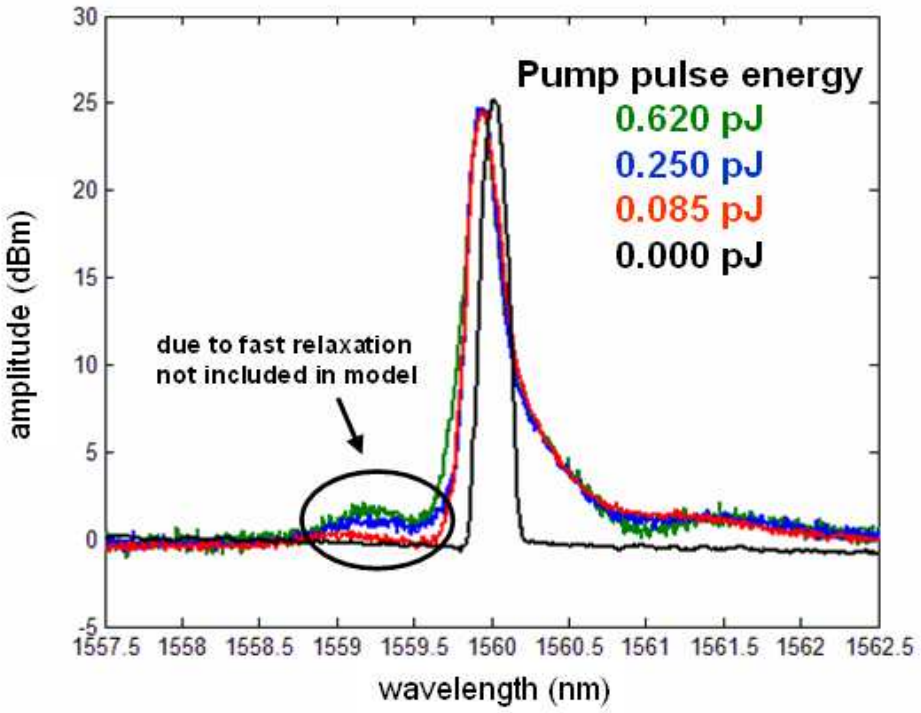

Figure 5.5: Broadening of the CW probe spectrum by the XPM induced frequency shift in a commercial SOA.

5.4.3 Characterization of the gain in SOAs

To obtain the SOA parameters for modeling, we first characterize the CW gain of the SOA with respect to pump pulse power using the setup in Fig. 5.6. In order to measure the gain, we first find the transparency current I_0 of the SOA. The transparency current is found by measuring the input power versus output power at different bias current level. When the bias current is below the transparency, the SOA acts as a saturable absorber, and we can see an positive curvature. When the bias current is above the transparency, the SOA acts as a saturable amplifier, and we can see an negative curvature. When the bias current is at transparency, we see a linear relation. The output power at transparency serves as the base value for gain

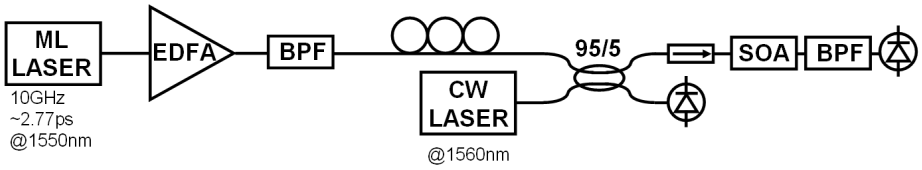

Figure 5.6: Experimental setup for characterizing the SOA gain as a function of pump pulse power.

measurement with all the connection and coupling loss taking into consideration. The gain is then calculated by dividing the output power at different input power with the base output value at the corresponding input power.

With fixed CW power, the CW gain of the SOA is measured as a function of the pump pulse input power. The results are plotted in Fig. 5.7 at two different injection current levels. The measured gain then is used in the modeling described in subsequent sections.

5.4.4 Modeling of XPM in SOAs

The model solves for the time dependent gain and phase as described in section 5.2. By varying the pump pulse power and the corresponding CW gain, we simulated the spectrum of the modulated CW signal. The result is shown in Fig. 5.8, a qualitative agreement between the simulation and the measured spectrum in Fig. 5.5 can be seen. By placing bandpass filters (Gaussian shaped filter with FWHM of 1.5nm) at different positions of the modulated CW spectrum, the filtered output is simulated and shown in Fig. 5.9. It can be seen that pulses can be obtained when the filter is placed sufficiently far away from the CW center wavelength. The

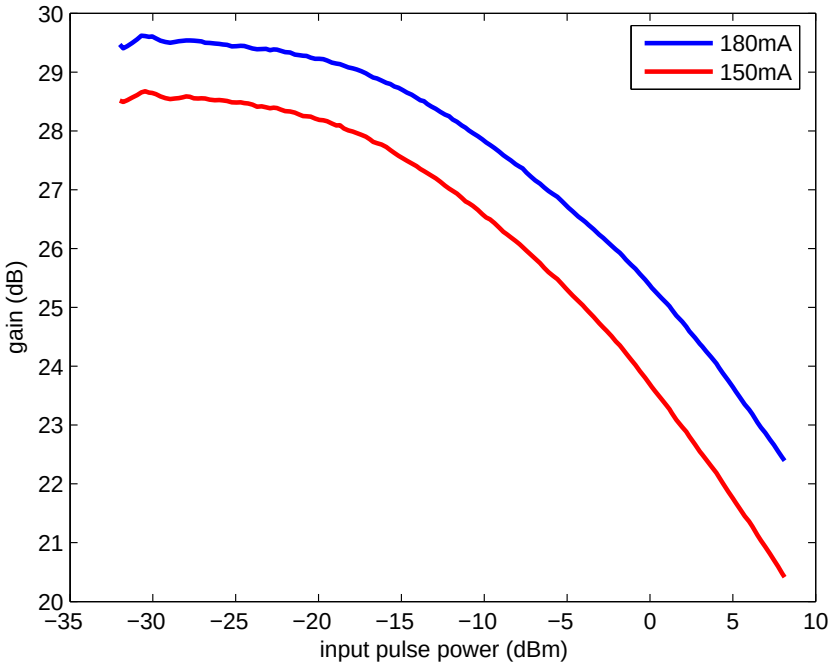

Figure 5.7: Measured SOA gain at two difference bias currents.

transmitted signal shape after the filter corresponds to the switch response when the CW signal is replaced by pulses. Thus, short switching window can be obtained using this configuration. Fast operation unlimited by the carrier time can thus be obtained using filter assisted frequency shift in SOAs.

5.5 Optical switching using XPM in segmented SOAs

For good switching performance, the filter has to be far enough from the signal frequency to suppress the slow recovery components and the unchirped fundamental frequency. Another way to suppress the slow recovery is to use a narrow bandwidth filter, however, this limits the application of the switch in high speed systems. It is obvious that a sufficient amount of frequency shift must be obtained in the device for

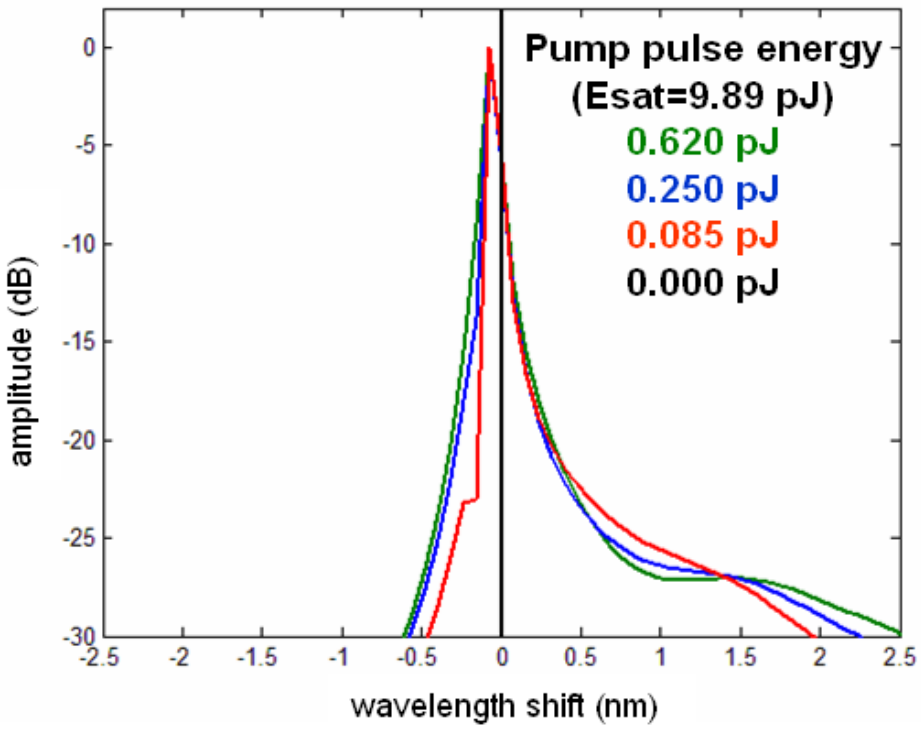

Figure 5.8: Modeled broadening of the CW probe spectrum by the XPM induced frequency shift.

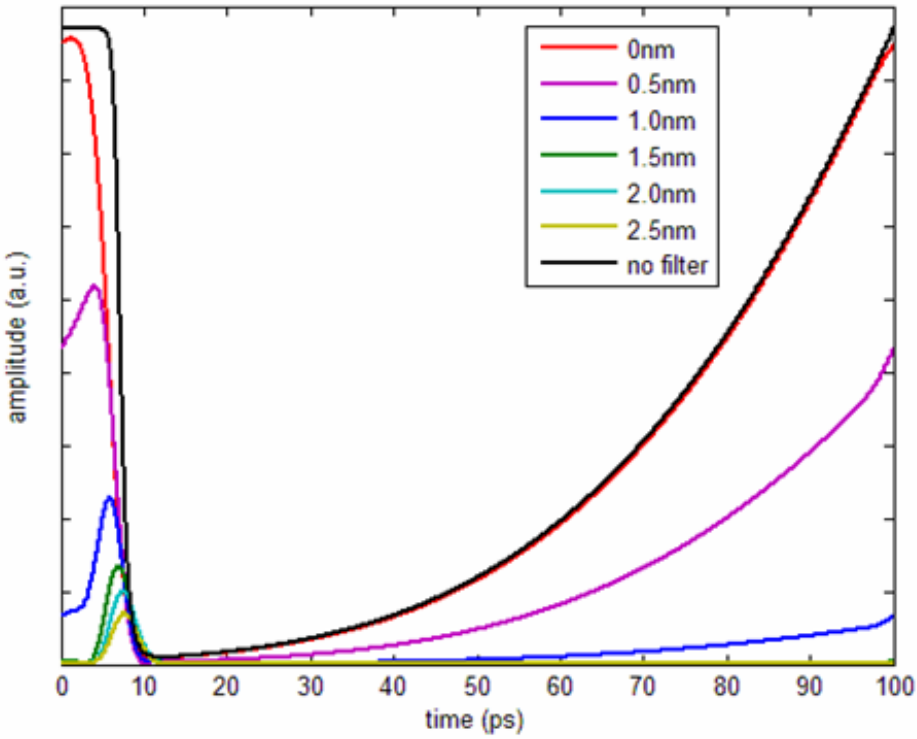

Figure 5.9: Modeling of filtered outputs of frequency shifted CW spectrum.

high speed operation. From (5.33), it is obvious that a shorter control pulse produces larger frequency shift and a shorter switching window, however, the control pulse has to be longer then the signal pulse for efficient switching. Increasing the phase shift θ is another way of increasing the switching time. From (5.30), it is obvious that a large linewidth enhancement factor α and large integrated gain h are beneficial.

The discussions so far only concern gain saturation in SOAs, however, the same equations can also be used to describe loss saturation in SOAs by considering the gain g in (5.28) as loss. When the SOA is reverse biased, it becomes a saturable absorber [7][8]. If the reversed biased SOA is used in the scheme shown in Fig. 5.2, the refractive index decreases as the loss is saturated by the pulse. As a result, instead of a red shift, the frequency shift described by (5.33) is now to the blue side. Fast switching can then be obtained by placing a filter in the blue side of the signal spectrum. From previous experiments [7][8], it is more efficient to obtain higher loss by increasing reverse bias in a short waveguide section then to obtain higher gain by increasing injection current or by increasing amplifier length. Thus, a saturable absorber is potentially a better candidate for high speed operations.

We propose using a segmented SOA with a long gain section to amplify the control pulse and a short saturable absorber section for the switching function. With the gain/loss combination, the total gain in the device can be kept low and thus avoid the problem of parasitic oscillation from the combination of amplified spontaneous emission and internal reflection [72]. The segmented SOA also allows counter-propagation of control and signal in the device as will be explained in later sections. This provides spatial separation of the control and signal. In the following

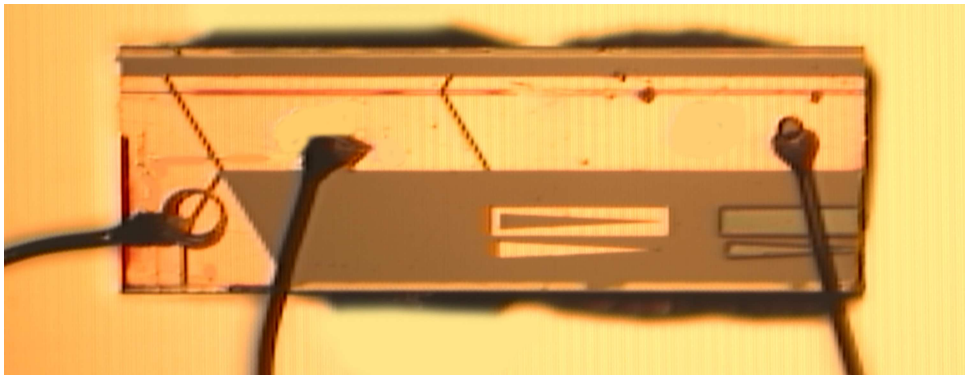

Figure 5.10: Microscope picture of the segmented SOA.

section, we explore the switching operation of SOAs with segmented gain and loss sections.

5.5.1 Segmented SOA

The top view of the segmented SOA is shown in Fig. 5.10. The device is composed of a six quantum well active region and a 3 μm wide ridge waveguide. The segments are defined by three separated gold contacts. The length of the right section is 635 μm, the middle section is 400 μm, and the left section is 85 μm. The separation creates electrical isolation between the segments and allows individual control of the bias condition of each segment. In our experiment, the left two sections are connected and reverse biased by a voltage source as a saturable absorber; and the right section is biased by a current source to amplify the control pulse. The built-in amplifier section allows lower power operation of the switch. The switching happens in the saturable absorber section using the blue shift caused by XPM.

The device used in the experiment was originally designed as a laser, as a

result, no anti-reflection coating is applied to the facet. When operating the device, the total gain has to be kept below the lasing threshold of the device. In the experiments and simulations presented below, the total gain is always kept equal to or lower than the total loss.

5.5.2 Counter-propagation in segmented SOA

In the previous discussions, the signal is cross-modulated by the co-propagating pump pulse. The signal is modulated by the integrated gain/loss h in (5.31), which is independent of the length of the device and spatial distribution of gain/loss in the device. If the signal and control pulse are co-propagated in a segmented SOA, the gain and loss segment cancels out each other since only the spatially independent total gain/loss is seen by the signal. Now, we consider the modified case where the signal and control are counter-propagating.

Using the formalism in section 5.3, the counter-propagating signals in segmented SOA can be described by

$$\frac{\partial A_1}{\partial z} + \frac{1}{v_g}\frac{\partial A_1}{\partial t} = \frac{1}{2}(1 - j\alpha)gA_1, \tag{5.34}$$

$$\frac{\partial A_2}{\partial z} - \frac{1}{v_g}\frac{\partial A_2}{\partial t} = \frac{1}{2}(1 - j\alpha)gA_2. \tag{5.35}$$

The gain is related to the signals by

$$\frac{\partial g}{\partial t} = \frac{g_0 - g}{\tau_c} - \frac{g(|A_1|^2 + |A_2|^2)}{E_{sat}}, \tag{5.36}$$

where we assume the wavelengths of the signal and control are different enough that their beating can be neglected. By transforming to a reference frame moving with

A_1 as before, we obtain

$$\frac{\partial A_1}{\partial \tau} = \frac{1}{2}(1 - j\alpha)gA_1, \tag{5.37}$$

$$\frac{\partial A_2}{\partial z} - \frac{1}{v_g/2}\frac{\partial A_2}{\partial \tau} = \frac{1}{2}(1 - j\alpha)gA_2, \tag{5.38}$$

$$\frac{\partial g}{\partial \tau} = \frac{g_0 - g}{\tau_c} - \frac{g(|A_1|^2 + |A_2|^2)}{E_{sat}}. \tag{5.39}$$

The amplitude and phase of the output of A_1 can be expressed as in (5.29) and (5.30) by

$$P_{1out}(\tau) = P_{1in}(\tau)\exp[h(\tau)] \tag{5.40}$$

$$\theta_{1out}(\tau) = \theta_{1in} - \frac{1}{2}\alpha h(\tau), \tag{5.41}$$

where the device response $h(\tau)$ is obtained by solving (5.38) and (5.39) over the length of the device. The signal now sees the integrated effect of the pump pulse at different spatial location of the segmented device over the length of the device. If the pulse width is shorter than the transit time through the device, any effect that occurs faster than the transit time through the device is averaged out. As a result, if the device is longer then the pulse, the switching performance is limited by the length of the device. On the other hand, if the device is shorter than the pulse, the switching performance is limited by the pulse width.

In the counter-propagating scheme, the interaction time between the signal and control is twice the transit time through the device. As can be seen in (5.38), in the reference frame moving with A_1, A_2 is effectively moving at half the group velocity, v_g, thus the interaction time is doubled.

Fig. 5.11 shows the schematics of a CW signal modulated by the control

pulse in a two segments SOA. The control pulse first saturates the gain section, which causes a decrease in gain (trace(a)). The control pulse then saturates the loss section, which increase the gain (trace(b)). If the gain is equal to loss, and the sections have the same recovery time, the recovery of gain and loss section compensates each other, and the integrated gain over the length of the device is thus described by trace(c). The transmission of the CW signal is modulated by the integrated gain, while its phase is also modulated by the same profile as related by the linewidth enhancement factor, α, in (5.41). The corresponding frequency shift described by the chirp in (5.33) is shown in trace(d). As described before, since the transit time through both sections is longer then the pulse width, the saturation time is determined by twice the transit time through the segments. Thus, the time constants in the figure are related to the segments lengths by $\tau_g = 2L_g/v_g$ and $\tau_l = 2L_l/v_g$. If the segment is short such that the transit time trough it is shorter than the pulse width, the time constant is then twice the pulse width.

Since the loss segment is shorter than the gain segment, a larger chirp in the blue side is expected as shown in trace(d). When a filter is aligned with the blue shifted part of the spectrum, a switching window corresponds to the loss saturation/positive chirp part will appear. When a filter is aligned with the red shifted part of the spectrum, a switching window corresponding to the gain saturation/negative chirp part will appear.

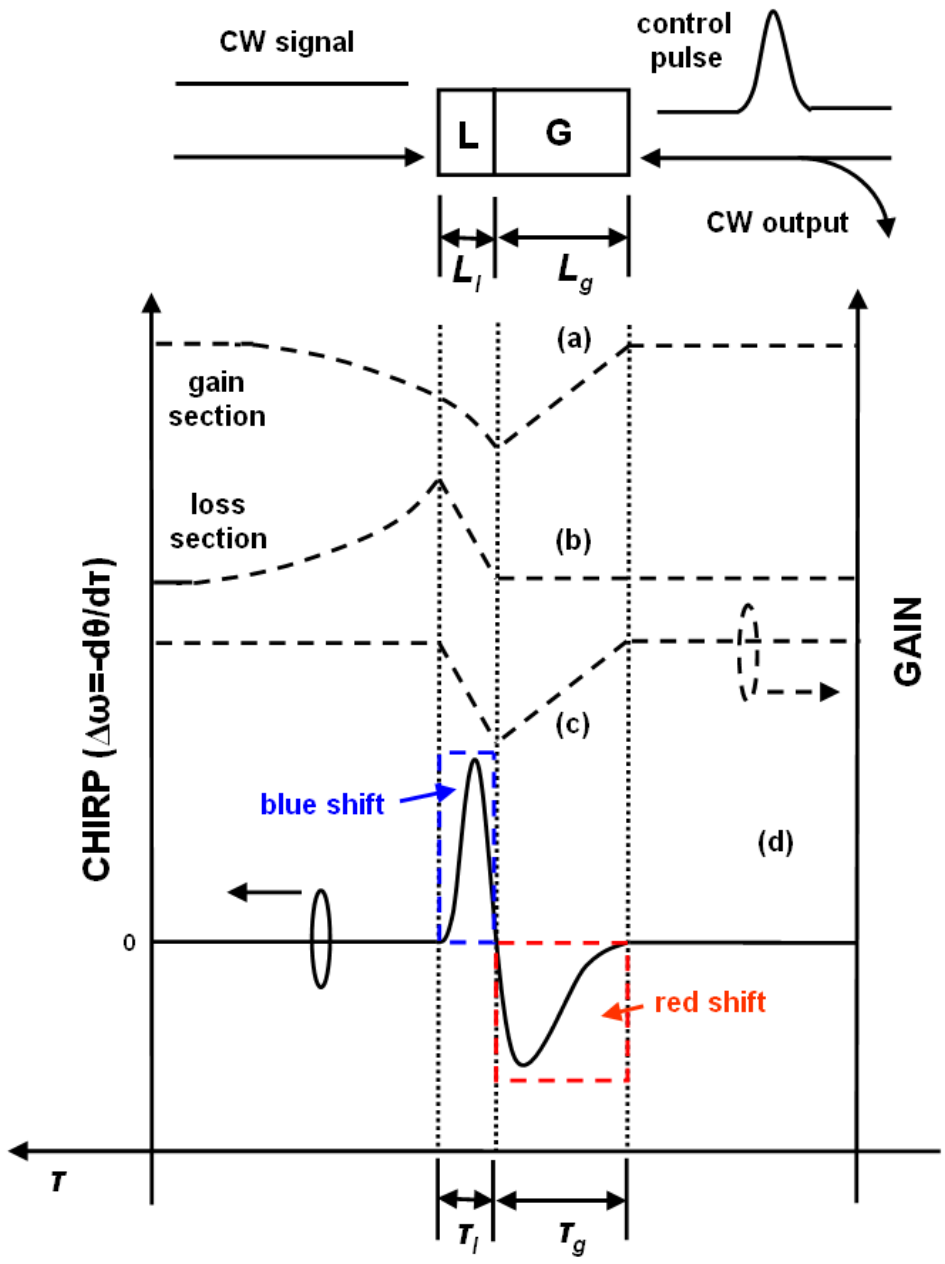

Figure 5.11: XGM and XPM in a two segments SOA. It is assumed that the gain equals loss, and the gain and loss sections have the same recovery time. Trace(a) shows the saturation and recovery of the gain segment. Trace(b) shows the saturation and recovery of the loss segment. Trace(c) shows the integrated effect of the gain and loss segments. Trace(d) show the corresponding chirp. The saturation time window is determined by the transit time through the segments since the pulse width is assumed to be shorter than the transit time.

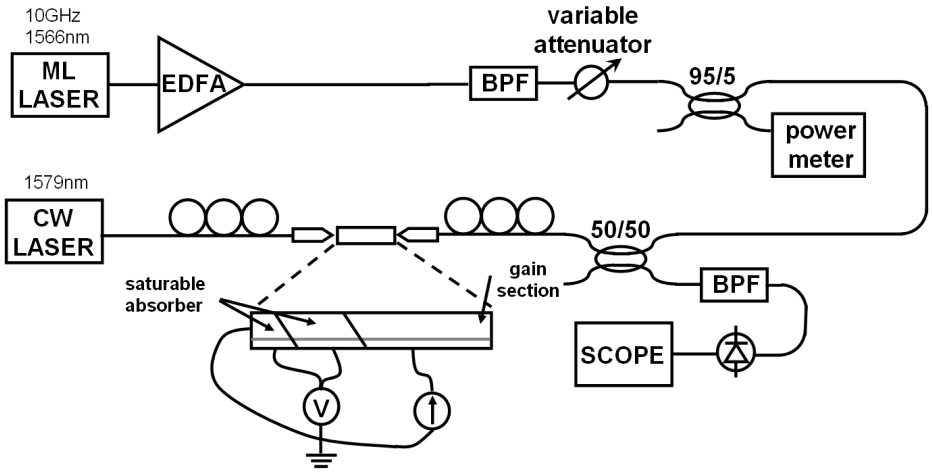

Figure 5.12: Experimental setup for characterizing the XPM induced frequency shift in segmented SOA.

5.5.3 Experimental demonstration of spectral broadening from XPM in segmented SOA

The device used in the experiment is the same one as shown in Fig. 5.10. The experimental setup for characterizing the spectrum broadening of CW signal in a segmented SOA is illustrated in Fig. 5.12. ML laser generates pulses with pulse width of 2.2 ps (FWHM) with a repetition rate at around 10 GHz at a wavelength of 1566 nm. The wavelength of the CW laser is 1579 nm. The control pulse and the CW laser are coupled into the device using lensed fibers on x-y-z stages. The gain section of the device is forward biased at 120 mA, and the loss section is reverse biased at 1.75 V. Fig. 5.13 shows the spectral broadening with various control pulse energy. A larger broadening in the blue side of the spectrum is observed from the measurement, which indicates larger loss than gain when the linewidth enhancement factor is considered to be equal in both segments.

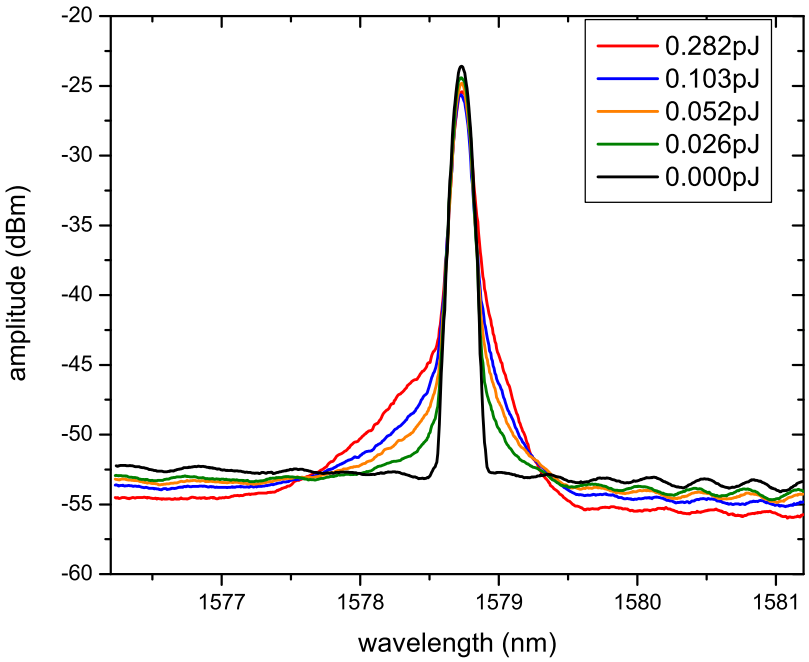

Figure 5.13: Broadening of the CW probe spectrum by the XPM induced frequency shift in a segmented SOA.

The switching window is measured by filtering the CW signal with a tunable bandpass filter (3 dB bandwidth $\sim$ 1.7 nm). The unfiltered CW spectrum with $\sim$ 0.3 pJ pump is shown in Fig. 5.14 together with the CW spectrum without pump pulse. The effect of spectral broadening from XPM is evident in the figure. We first align the filter with the center of the spectrum and then move it to the blue side (-1.5 nm from the center) of the spectrum. The filter shape and position is measured and plotted together with the broadened CW spectrum in Fig. 5.15. The filtered outputs are amplified with an EDFA and measured using a 45 GHz detector on an optical sampling scope. The results are shown in Fig. 5.16. The measured output is convolved with detector response and does not represent the real output. From the data, it is clear that the switching window is aligned with the loss saturation/positive chirp part as predicted.

In order to obtain better temporal resolution unlimited by the detector response, optical sampling technique is used, and a pulsed laser is used in place of the CW laser in Fig. 5.12. The modified experimental setup is illustrated in Fig. 5.17. When the two pulsed lasers have the same repetition rate, the probe pulse can sample the device temporal response by changing the relative time delay between the probe and pump pulses. Instead of varying the time delay, a small difference Δf is introduced in the repetition rate f of the two pulsed lasers; and the relative delay between the probe laser and the pump laser is in effect modulated with frequency Δf. The material response repeating every $1/f$ seconds is now sampled with a repetition rate of Δf. The signal can now be detected with a sensitive low bandwidth detector. The resolution of this technique is limited by the temporal width of the

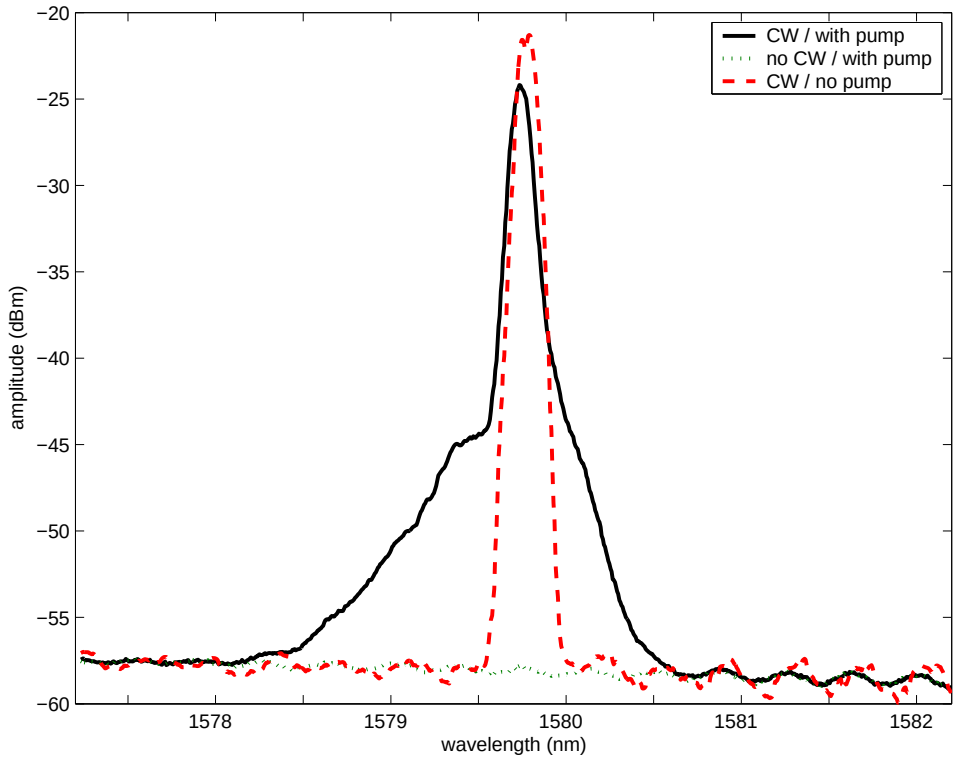

Figure 5.14: Measured effect of XPM induced frequency shift to the CW probe spectrum in a segmented SOA.

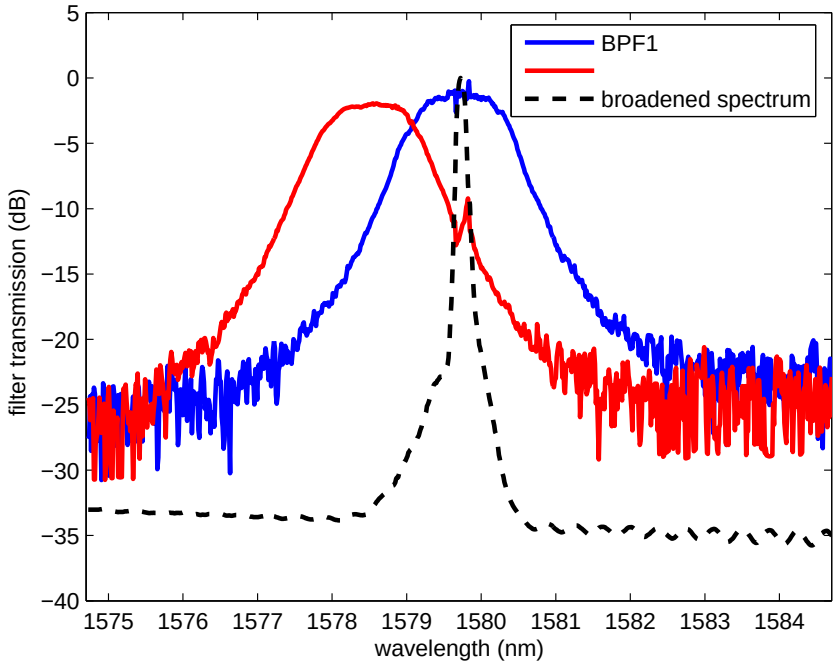

Figure 5.15: Measured filter shape and position with respect to the broadened spectrum. BPF 1 is aligned with the center of the spectrum. BPF 2 is -1.5 nm from the center of the spectrum. The black dashed curve shows the normalized amplitude of the broadened CW spectrum.

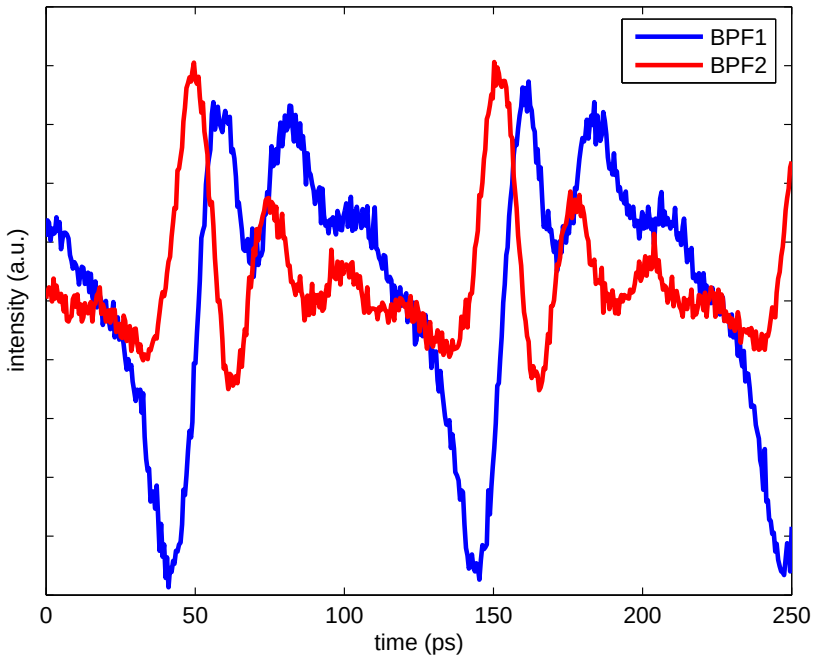

Figure 5.16: Measured outputs on an optical sampling scope corresponding to different filter positions. BPF 1 is aligned with the center of the spectrum. BPF 2 is -1.5 nm from the center of the spectrum.

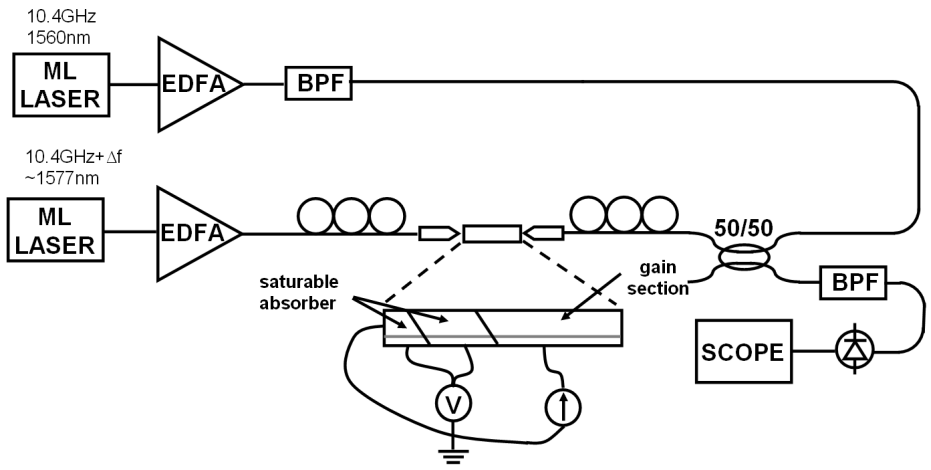

Figure 5.17: Experimental setup for characterizing the XPM induced frequency shift in segmented SOA using optical sampling technique.

probe pulse. In our experiment, the wavelength of the pump laser is 1560 nm, the wavelength of the probe laser is 1577 nm, both lasers have a repetition rate of ∼10.4 GHz, the difference frequency Δf is 5 kHz, and both lasers have a pulse width of 2.2 ps.

The device response is measured with a tunable bandpass filter (3 dB bandwidth $\sim$ 1.7 nm) at different positions of the output probe pulse spectrum. Fig. 5.18 shows the positions and shape of the filter along with the probe spectrum. Fig. 5.19 shows the device response when the filter is tuned to the blue side (BPF1-3) and aligned with the center (BPF4); and Fig. 5.20 shows the device response when the filter is tuned to the red side (BPF5-8). The $1/f \approx 100$ ps repetition period is down sampled to $1/\Delta f = 200$ μs. In Fig. 5.19 and 5.20, the time axis is re-normalized to 100 ps and shown as the delay $\Delta\tau$ between the pump and the probe pulses. The gain saturation time ($\sim$ 12 ps) and loss saturation time ($\sim$ 10 ps) correspond to

twice the transit time through the respective sections. It is clear that the loss is larger than gain in the device, which results in the overshoot of loss saturation. As predicted by theory, when the filter is tuned to the blue side, a switching window corresponding to loss saturation/positive chirp part is obtained. The filtered output indicates insufficient filter discrimination since the spectral width of the sampling pulse is larger than that of the CW laser used in the previous experiment; and the filter 3 dB bandwidth is $\sim$ 1.7 nm. When the filter is tuned to the red side, no clear switching window can be seen. This indicates insufficient negative chirp, which could result from the slightly longer transit time through the gain section; small gain in the gain section; or small linewidth enhancement factor corresponding to the gain saturation. The experimental result clearly indicates that the loss saturation is indeed more efficient for XPM switching applications in these devices.

5.5.4 Simulation of counter-propagation in segmented SOA

A simple model is developed to simulate the switching performance using the counter-propagating scheme in Fig. 5.11. The integrated device response $h(\tau)$ is solved using finite difference method [73] by choosing the relation between time and spatial steps as $\Delta z = (v_g/2)\Delta\tau$, where N is an integer. The spatial step Δz is chosen so that the corresponding $\Delta\tau$ is shorter than the pulse width so that the response is not limited by the transit time. In each propagation step, instead of using a first-order difference approximation as in ref. [73], the differential equations (5.37)-(5.39) are solved numerically. The calculated fields are stepped in time and

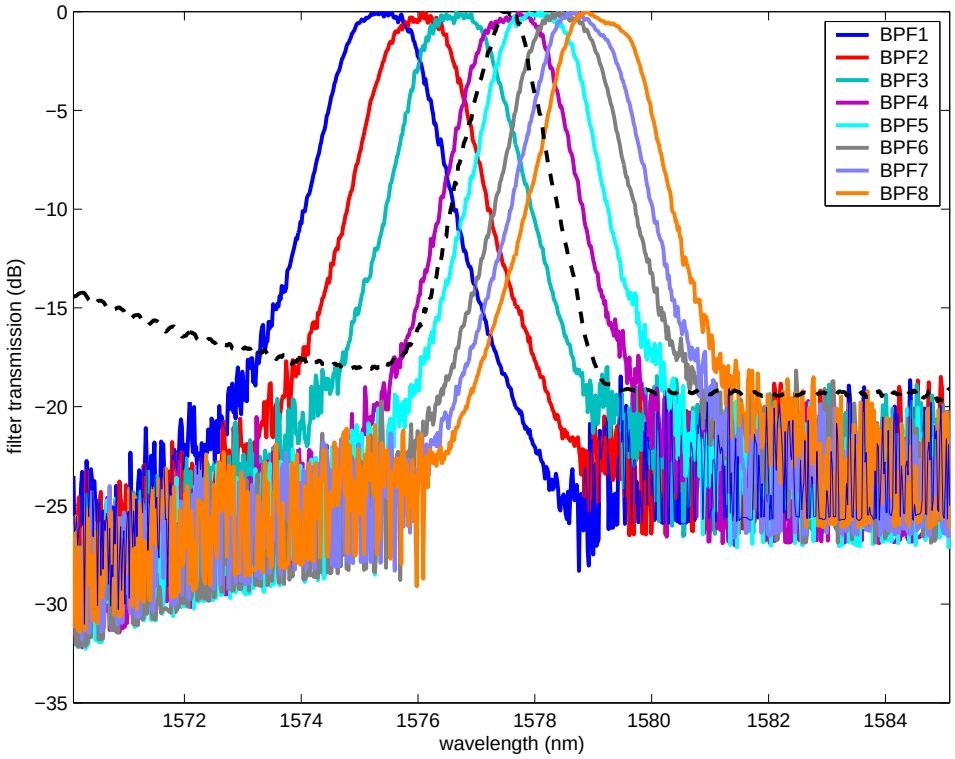

Figure 5.18: Measured bandpass filter (BPF) positions with respect to the probe spectrum (dashed black line).

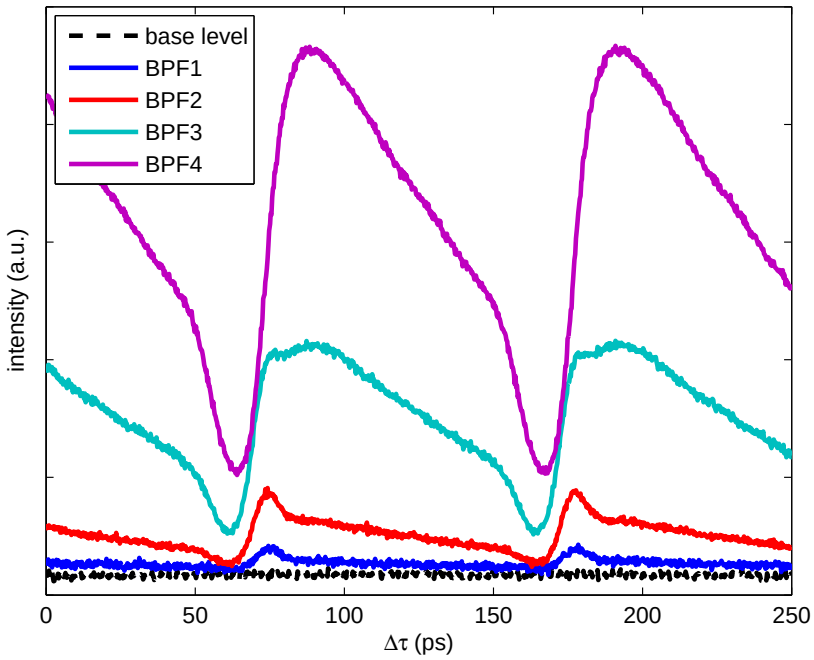

Figure 5.19: Measured outputs using optical sampling technique corresponding to different filter positions in the blue side (BPF1-3) and center (BPF4) of the spectrum. The filter labels correspond to the filter positions in Fig. 5.18.

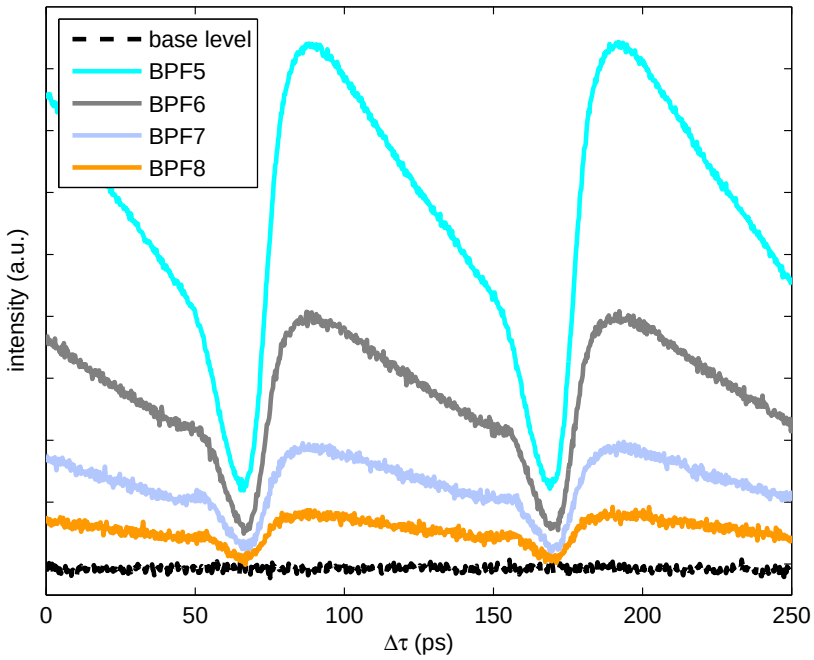

Figure 5.20: Measured outputs using optical sampling technique corresponding to different filter positions in the red side of the spectrum. The filter labels correspond to the filter positions in Fig. 5.18.

used as the input for the next spatial step. The integrated device response $h(\tau)$ is obtained after transition through the whole length of the device.

The schematics shown in Fig. 5.11 are simulated using the model. A device with 300 μm loss segment and 600 μm gain segment is simulated. The gain and loss segments are assumed to have the same unsaturated gain/loss of 25dB, the same saturation energy of 10 pJ, the same linewidth enhancement factor of 5, and the same recovery time. The index of refraction of the waveguide is assumed to be 3. The 300 μm saturable absorber section is chosen such that the corresponding transit time is 3 ps, and the corresponding switching window is thus close to twice the transit time at 6 ps.

The input control pulse has a Gaussian shape with FWHM of 2 ps. The CW signal, presented by a delta function in spectrum, is assumed to be weak compared to the control pulse. The XGM modulated CW signal output is shown in Fig. 5.21. The asymmetrical shape is determined by the transit time through the gain and loss segments. It can be seen that the time interval from normalized intensity 1 to minimum intensity is twice the transit time, 6 ps, through the 600 μm gain section. The time interval from the minimum back to 1 is again twice the transit time, 3 ps, through the 300 μm loss section. The corresponding chirp is shown in Fig. 5.22, which agrees with the prediction in Fig. 5.11.

The spectrum broadening of the CW signal is shown in Fig. 5.23. As expected, a larger blue shift is seen in the spectrum since the loss segment is shorter than to gain segment. Increasing control pulse energy results in larger broadening as predicted, and the simulated data shows a qualitative agreement with experimental

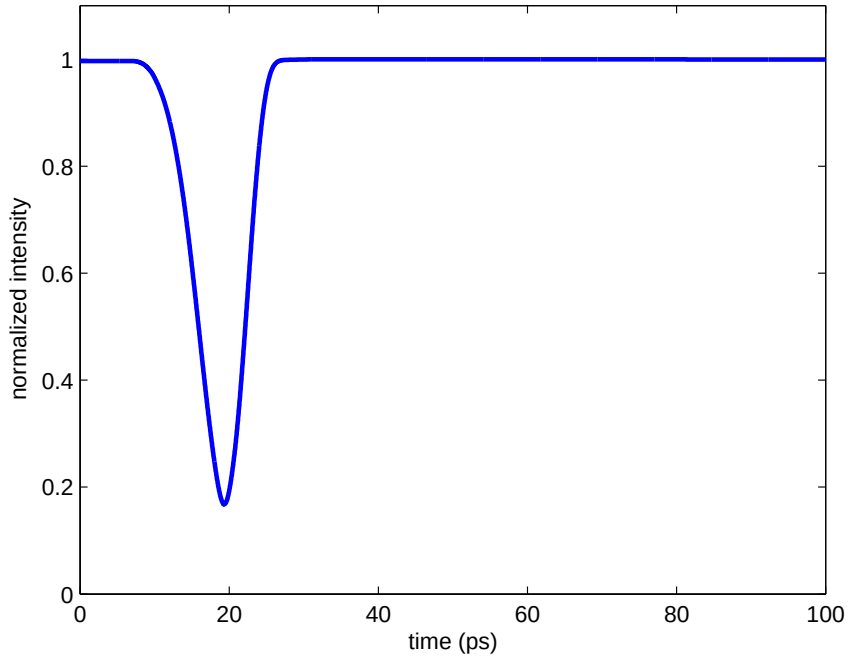

Figure 5.21: Simulated CW signal output modulated by XGM in a segmented SOA.

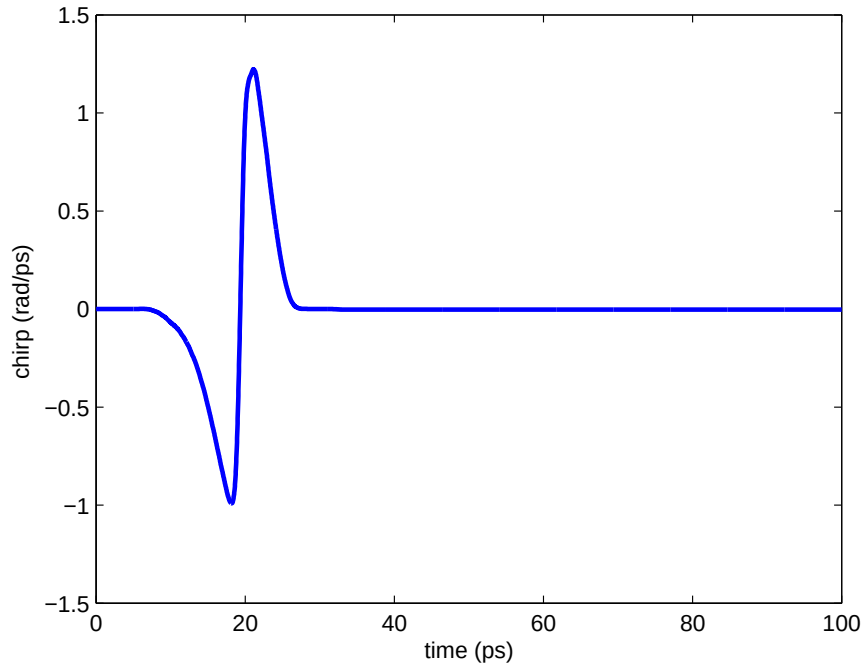

Figure 5.22: Simulated chirp of the CW signal by XPM in a segmented SOA.

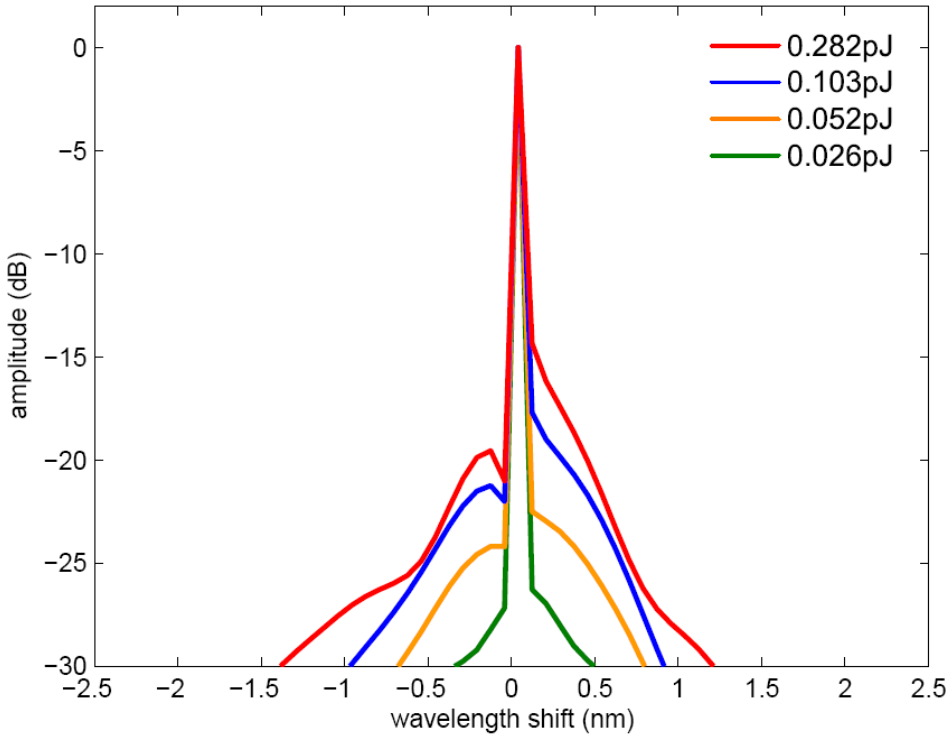

Figure 5.23: Simulated broadening of the CW signal spectrum by the XPM induced frequency shift in a segmented SOA.

data in Fig. 5.13.

The switching window is simulated by filtering the output with a bandpass filter (assuming a Gaussian shaped filter with 3 dB bandwidth of 1.5 nm). The pump pulse energy is 0.3 pJ. The result of the filtered output with the filter shifted -2.2 nm from the center of the spectrum is shown in Fig. 5.24 together with the unfiltered output and the corresponding chirp. It can be seen that a clear switching window $\sim$ 6.5 ps is obtained by placing the filter in the blue shifted part of the spectrum. The window corresponds to the loss saturation/positive chirp part of the unfiltered output, which is expected since the filter only select the blue shifted part of the signal. The switching window again is limited by the transit time through

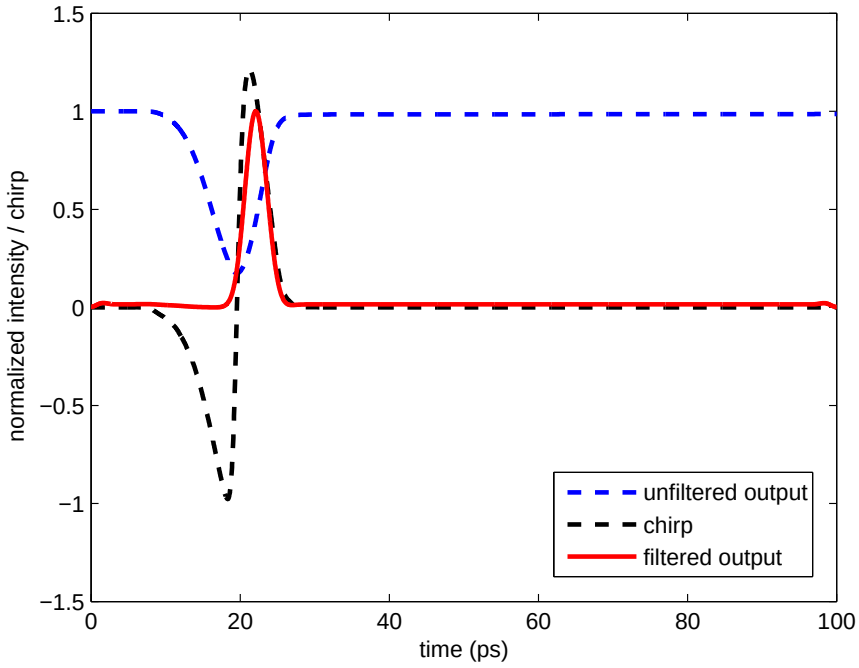

Figure 5.24: Simulated switching window by the XPM induced frequency shift in a segmented SOA.

the loss segment of the SOA.

To further investigate the effect of the length of loss segment on the switching performance, the switching window is simulated by varying the loss segment length while keeping the total device length, the gain, and the loss constant. The control pulse is a Gaussian pulse with FWHM of 2 ps, and the pulse energy is 0.3 pJ. The bandpass filter is a Gaussian shaped filter with 3 dB bandwidth of 1.5 nm detuned 2.2 nm to the blue side of the spectrum. Loss segment lengths of 50 μm, 100 μm, 300 μm, and 500 μm are simulated. The results are shown in Fig. 5.25. For the 50 μm and 100 μm loss segments, the transit time is shorter than the pulse width of 2 ps, the window is approximately twice the pulse width of the control signal. For longer loss segments, the switching window grows linearly with the transit time. While the

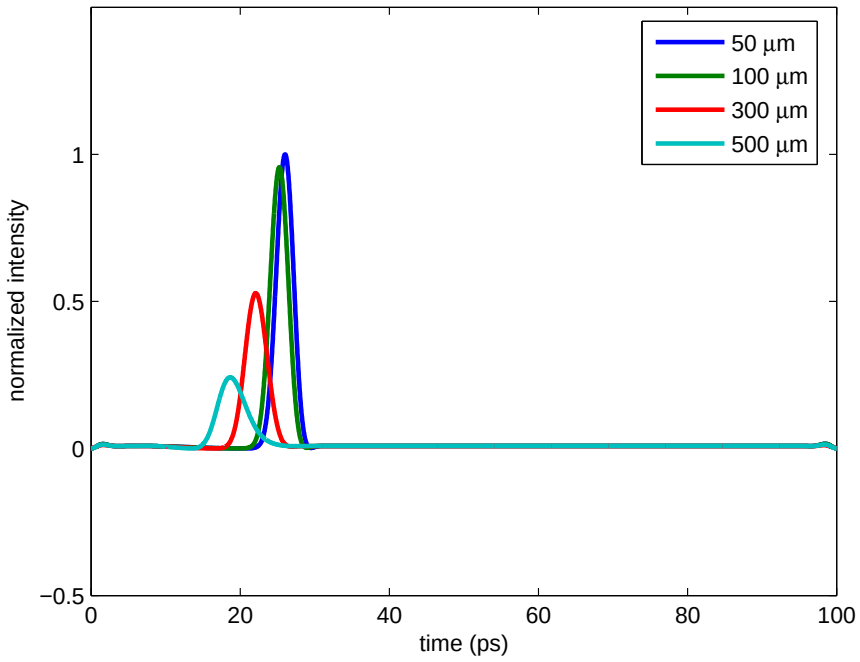

Figure 5.25: Simulated switching windows by the XPM induced frequency shift in segmented SOA with different loss segment lengths.

gain and loss are the same in all four cases, shorter segments lead to larger positive chirp, as a result, more energy is transmitted through the blue shifted filter. The simulation verifies the limit on switching window by both the segment length and the pulse width.

Various control pulse widths are also simulated with varying segment length. The simulated FWHM of the resulting switching window are shown in Fig. 5.26. The simulation results provide a guideline for optimizing switch design for high speed applications. It can be seen that with a loss segment of 200 μm, $\leq$ 6 ps switching window can be obtained with $\leq$ 2 ps control pulses, which allows demultiplexing of 160 Gbps data steams.

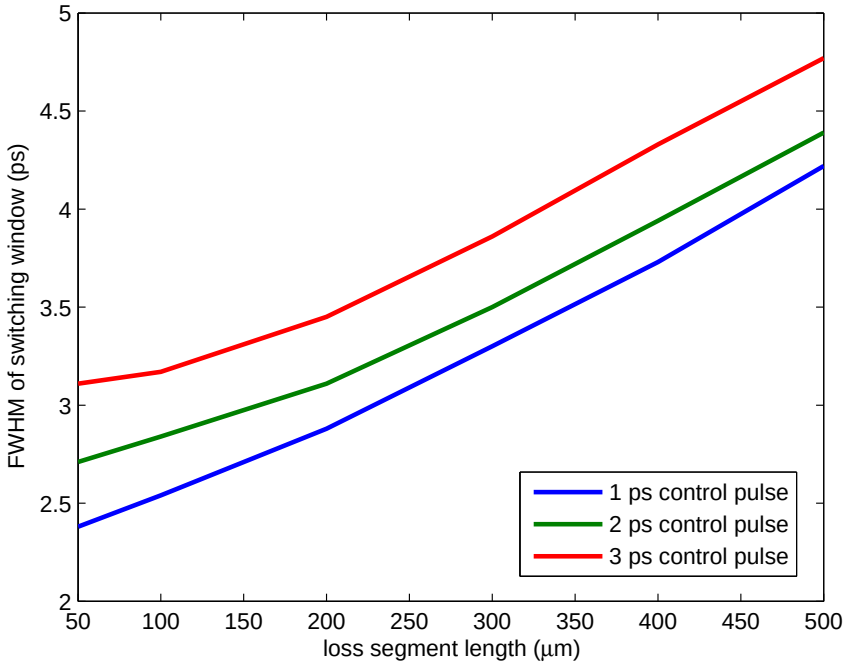

Figure 5.26: Simulated FWHM of switching windows for various control pulse widths with different loss segment lengths for the counter-propagating geometry.

5.6 Conclusion

The concept of optical switching using XPM in SOAs is investigated. Using a commercial SOA, the spectral broadening from XPM in SOA is measured, which agrees well with the theoretical model. For more efficient switching performance, a segmented SOA with gain and loss segment is proposed. The gain segment lowers the required switching power, and a short loss segment provides a short switching window. Experimental results with a prototype segmented devices agree well with theoretical prediction. A model is developed to analyze the switching performance of the device. The simulations show that a 6 ps or less switching window can be obtained with loss segment smaller than 200 μm in a counter-propagation geometry.

Chapter 6

Conclusion

6.1 Accomplishments

We set out to investigate the feasibility of integrated linear optical signal processing using holograms in multimode waveguides. We demonstrated, for the first time, that using multimode waveguide hologram (MWH), arbitrary unitary transformations can be implemented efficiently without the need of integrated waveguide lenses. We also developed a recipe for MWH design using the beam propagation method (BPM).

For the development of nonlinear components for optical signal processing, we developed a simple optical setup for characterization of the complex $\chi^{(3)}$ of nonlinear materials based on an imaged 2-D phase grating. This technique provides a reliable way to measure $\chi^{(3)}$ as new materials are constantly being developed.

Also, we proposed and demonstrated the operation principle of an optical switch based on segmented SOAs. It allows the implementation of counter-propagation geometry in the switch, and avoids the problem of parasitic oscillations in switches using high gain SOAs.

The following section provides a brief summary of this thesis.

6.2 Summary

In order to implement useful signal processing operations, it is necessary to develop novel linear and nonlinear integrated optical components. The different aspects of linear and nonlinear optical signal processing investigated in this work are summarized in this section.

Implementation of arbitrary unitary transformation using MWH is presented in this thesis. We take advantage of the parallelism of optics and perform linear operations using MWHs. In chapter 2, it is proven that arbitrary unitary transformations can be performed by holograms in multimode waveguides. The general design principle of unitary mode transformation and unitary matrix-vector multiplier using MWH devices is presented. A special design case using the self-imaging property of multimode waveguide is also identified. It is also shown that the design method using the self-imaging property is equivalent to the general design principle.

In chapter 3, a WA-BPM model using Padé (3,3) approximant operator is developed to simulate and design MWH devices. A mode-order converter, a Hadamard transformer, and a optical pattern generator/correlator are designed and simulated. The model shows good agreement with the theory. 3-bit optical pattern generators are designed using the WA-BPM model and fabricated using polymer waveguides. Characterization of the fabricated devices verifies the theory and model. The model is used to investigate the bandwidth and fabrication tolerances of MWH devices. It is shown that devices with larger than 8 ports will be difficult to fabricate with current technology. For applications to pattern recognition, the degradation in BER

due to device imperfection is analyzed. The device performance is shown to be closely related to bandwidth and fabrication tolerances.

Unfortunately, none of the existing nonlinear polymers are adequate for integrated nonlinear processing. Since new materials are being made available to us through the DARPA's MORPH program, we constructed a simple and reliable setup for characterization of complex $\chi^{(3)}$. In chapter 4, a simple optical setup for characterizing the complex $\chi^{(3)}$ of nonlinear materials using DFWM with a imaged 2-D phase grating is presented. The absolute value of $|\chi^{(3)}|$ is obtained by comparing the diffraction efficiency of the nonlinear sample to that of the reference fused silica sample. By passive phase stabilization with the 2-D phase grating, coherent detection of the DFWM signal is performed using the same setup. By changing the phase of the reference beam, the phase of $\chi^{(3)}$ is obtained. A polyacetylene sample is measured with this setup. Its nonlinearity is 7.0×10^{-11} esu with a phase of $21.0°$.

Although we do not have nonlinear polymers with sufficiently large $\chi^{(3)}$ for integrated optical switches, the large carrier dependent index change in SOAs allows us to implement optical switching with available material. In chapter 5, ultrafast optical switching using XPM in SOAs is investigated. The operating principle is first experimentally verified with a commercial SOA with high gain. Switches with high gain would lead to parasitic oscillations in the system. As an alternative, a segmented SOA with a long amplifier section and a short saturable absorber section is proposed. This configuration allows counter-propagation of the signal and control pulses; and parasitic oscillations can be avoided since the whole device doesn't have to be operated at high gain. The concept of counter-propagation in segmented SOA

is presented. A prototype device is characterized using optical sampling technique to demonstrate the principle. A model is developed to obtain optimum parameters for future devices.

6.3 Discussions and future work

Discrete unitary transformations have many applications in signal processing. Discrete Fourier transform (DFT), the discrete Hartley transform (DHT) are very useful for 1-D and 2-D signal processing applications. The discrete cosine transform (DCT) is the most efficient transform for compression of speech and image data. Many algorithms have been developed for efficient computation of the DFT, DHT, and the DCT [74] by breaking the transformation of long patterns into multiple transformations of smaller patterns. The importance of these transformations leads to the development of dedicated electronic chips designed for matrix-vector multiplication. However, the speed of these chips are still limited. An example given in ref [75] is a 16×16 analog matrix-vector multiplier with a operating frequency of 500 kHz.

All of the aforementioned transformations can be implemented with a single MWH using parallel processing in integrated optics. The processing speed of the MWH processors is basically limited by the bandwidth of the multimode waveguides as shown in our simulations. Recent work [76] shows that the bandwidth still exceeds 1 GHz when the port number is 128 when assuming no fabrication error. Our simulations also indicate the inverse proportionality between the port number

and the bandwidth/fabrication tolerance. Although the size of the MWH processors is limited by the fabrication technology, it is obvious that an optical processor using MWH offer tremendous bandwidth advantage over electronic processors. Future work would involve identifying suitable algorithms to implement long pattern unitary transformations using multiple transformations of smaller pattern with integrated MWH processors.

Possible implementation of programmable matrix using electro-optic materials can also be considered. In particular, new electro-optic polymers with high $\chi^{(2)}$ are under development, which could make implementation of programmable MWH devices possible. Future development of high $\chi^{(3)}$ materials could allow us to replace the SOAs, which would dramatically reduce power consumption of future processors.

Appendix A

Effective Index Method

Here, we discuss the effective index method, which allows the analysis of 3-D step index optical waveguides using 2-D slab optical waveguides.

The scalar wave equation (2.15) is

$$\nabla_{\perp}^2 \phi + k_0^2 (n^2(x,y) - n_{eff}^2)\phi = 0, \tag{A.1}$$

where n_{eff} is the effective index to be determined. Assuming there is no or little interactions between the x and y field components, the wave function $\phi(x,y)$ can be written by variable separation as

$$\phi(x,y) = f(x)g(y). \tag{A.2}$$

Substituting (A.2) into (A.1) and dividing through by $\phi(x,y)$, we obtain

$$\frac{1}{f(x)}\frac{\mathrm{d}^2 f(x)}{\mathrm{d}x^2} + \frac{1}{g(y)}\frac{\mathrm{d}^2 g(y)}{\mathrm{d}y^2} + k_0^2(n^2(x,y) - n_{eff}^2) = 0. \tag{A.3}$$

Let

$$\frac{1}{g(y)}\frac{\mathrm{d}^2 g(y)}{\mathrm{d}y^2} + k_0^2 n^2(x,y) = k_0^2 N^2(x), \tag{A.4}$$

we have

$$\frac{1}{f(x)}\frac{\mathrm{d}^2 f(x)}{\mathrm{d}x^2} - k_0^2 n_{eff}^2 = -k_0^2 N^2(x). \tag{A.5}$$

The two equations above can be rewritten as

$$\frac{1}{g(y)}\frac{\mathrm{d}^2 g(y)}{\mathrm{d}y^2} + k_0^2[n^2(x,y)N^2(x)] = 0, \tag{A.6}$$

we have

$$\frac{1}{f(x)}\frac{\mathrm{d}^2 f(x)}{\mathrm{d}x^2} + k_0^2[N^2(x) - n_{eff}^2] = 0. \tag{A.7}$$

Equation (A.6) describes the first step of the effective index calculation. First, we replace the 3-D structure Fig. A.1(a) with a combination of 2-D slab waveguides as in Fig. A.1(b). For each slab waveguides, the effective index N along the y axis is calculated.

Then, the effective index profile $N(x)$ calculated using (A.6) is used to model the 3-D waveguide using the 2-D slab waveguide in Fig. A.1(c). The beam propagation is solved by using the effective index profile in the 2-D wave equation (A.7).

Appendix B

Programming of the WA-FD-BPM using Padé (3,3) approximate operator

The theory of the multistep WA-FD-BPM using Padé approximations is described in section 3.2. Here, we describe the FD expression of the algorithm.

First, the x and z coordinates are discretized as follows,

$$x = p\Delta x, \tag{B.1}$$

$$z = m\Delta z, \tag{B.2}$$

where p and m are integers. The corresponding discretized wave function $\phi(x, z)$

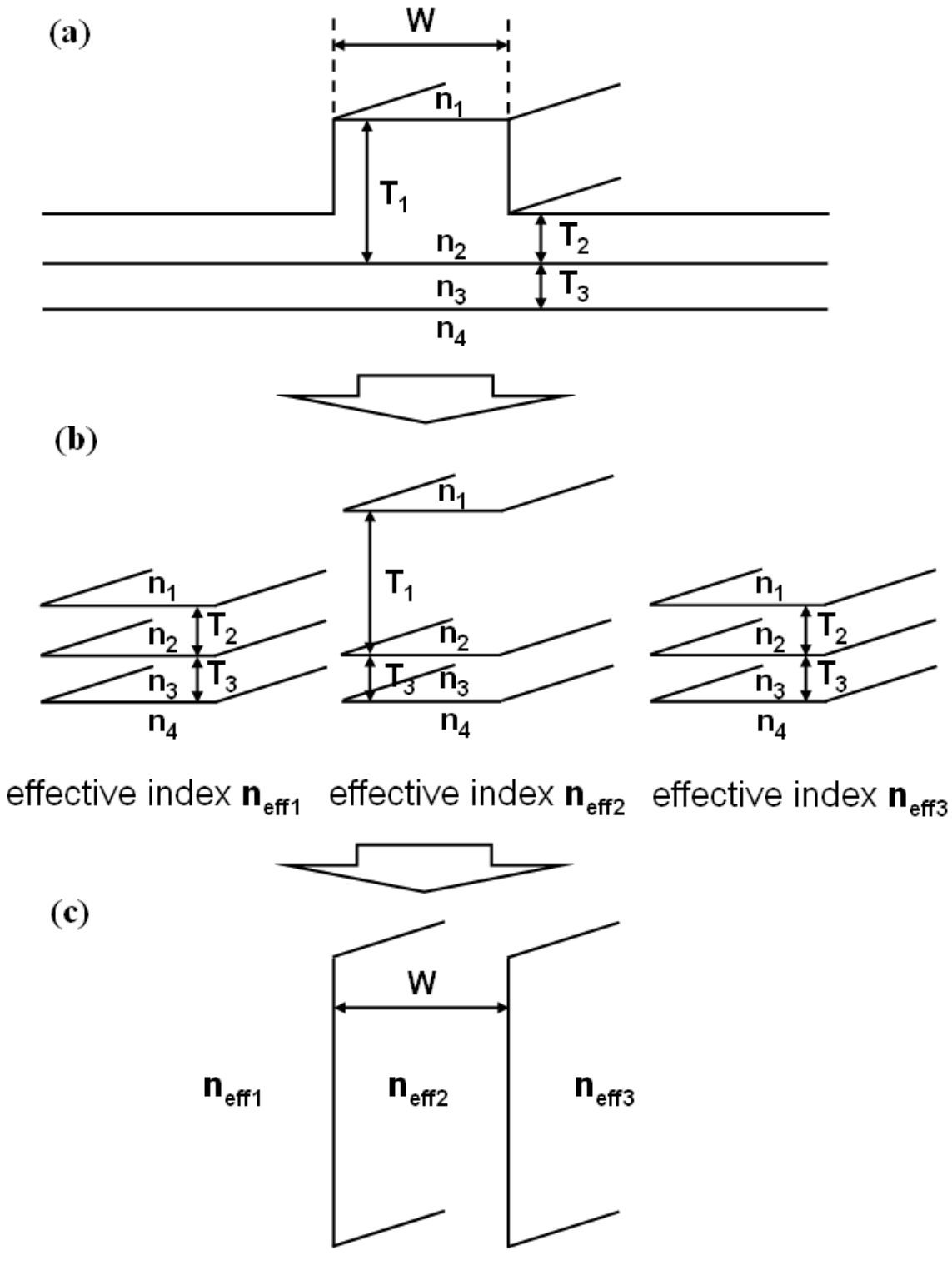

Figure A.1: Concept of the effective index method.

and index profile $n(x,z)$ are

$$\phi(x,z) \rightarrow \phi_p^m, \tag{B.3}$$

$$n(x,z) \rightarrow n_p^m. \tag{B.4}$$

The next step is to discretize the propagator (3.19), which is repeated here

$$\phi^{m+\frac{i}{n}} = \frac{(1+a_i P)}{(1+a_i^* P)} \phi^{m+\frac{i-1}{n}}. \tag{B.5}$$

The operator P in the propagator is

$$P = \nabla_\perp^2 + k_0^2(n^2 - n_{ref}^2). \tag{B.6}$$

The two terms of $P\phi_p$ are expressed as

$$\begin{aligned} \frac{\partial^2 \phi_p}{\partial x^2} &= \frac{1}{\Delta x}\left(\frac{\phi_{p+1}-\phi_p}{\Delta x} - \frac{\phi_p - \phi_{p-1}}{\Delta x}\right) \\ &= \frac{\phi_{p+1} - 2\phi_p + \phi_{p-1}}{(\Delta x)^2}, \end{aligned} \tag{B.7}$$

and

$$k_0^2(n^2 - n_{eff}^2)\phi_p = k_0^2[n_p^2 - n_{eff}^2]\phi_p. \tag{B.8}$$

So, the operator can be calculated using the following expression,

$$P\phi_p = \frac{\phi_{p+1} - 2\phi_p + \phi_{p-1}}{(\Delta x)^2} + k_0^2[n_p^2 - n_{eff}^2]\phi_p. \tag{B.9}$$

With the expression for $P\phi_p$, the algorithm simply involves applying the propagator on ϕ^m multiple times to obtain ϕ^{m+1} as described by (3.19).

BIBLIOGRAPHY

[1] B. G. Boone, *Signal Processing using Optics* (Oxford, New York, 1998).

[2] F. T. S. Yu and S. Jutamulia, *Optical Signal Processing, Computing, and Neural Networks* (Wiley, New York, 1992).

[3] T. J. Xia, Y. Liang, K. H. Ahu, J. W. Lou, O. Boyraz, Y. -H. Kao, X. D. Cao, S. Chaikamnerd, J. K. Anderson, and M. N. Islam, "All-optical packet-drop demonstration using 100-Gb/s words by integrating fiber-based components," IEEE Photon. Technol. Lett. 10, 153-155 (1998).

[4] Y. S. Bai, W. R. Babbit, N. W. Carlson, and T. W. Mossberg, "Real-time otpical waveform convolver/cross correlator," Appl. Phys. Lett. 45, 714-716 (1984).

[5] J. S. Wey, D. L. Butler,N. W. Rush, G. L. Burdge, and J. Goldhar, "Optical bit-pattern recognition by use of dynamic gratings in erbium-doped fiber," Opt. Lett. 22, 1757-1759 (1997).

[6] J. D. Shin, S. H. Paek, H. Y. Kim, K. J. Kim, and C. S. Kang, P"acket error analysis of an all-optical packet switching node using a fiber-optical delay line matched filter as an optical packet address processor," IEEE Photon. Technol. Lett. 9, 1637-1639 (1997).

[7] H.-Y. Yu, "High-Bit-Rate Optical Signal Processing Using Nonlinear Effects in Semiconductor Optical Amplifiers," Ph.D. dissertation (University of Maryland, College Park, USA, 1999).

[8] P. V. Petruzzi, "Optical Pattern Recognition using a Segmented Semiconductor Optical Amplifier," Ph.D. dissertation (University of Maryland, College Park, USA, 2003).

[9] A. Vanderlugt, *Optical Signal Processing* (Wiley, New York, 1992).

[10] P. Hariharan, *Optical Holography: Principles, techniques, and applications* (Cambridge, 1996).

[11] T. W. Mossberg, "Planar holographic optical processing devices," Opt. Lett. 26, 414-416 (2001).

[12] C. Greiner, D. Iazikov, and T. W. Mossberg, "Lithographically Fabricated Planar Holographic Bragg Reflectors," J. Lightwave Technol. 22, 136-145 (2004).

[13] S.-Y. Tseng, Y. Kim, C. Richardson, and J. Goldhar, "Optical Processor using Waveguide Holograms in Multimode Interference (MMI) Couplers," in *Conference on Lasers and Electrooptics on CD-ROM* (The Optical Society of America, Washington, DC, 2005), JTuC70.

[14] S.-Y. Tseng, Y. Kim, C. J. K. Richardson, and J. Goldhar, "Implementation of discrete unitary transformations by multimode waveguide holograms," to appear in Appl. Opt.

[15] N. J. Doran and D. Wood, "Nonlinear-optical loop mirror," Opt. Lett. 13, 56-58 (1988).

[16] J. D. Merlier, G. Mothier, S. Verstuyft, T. Van Caenegen, I. Moerman, P. Van Daele, and R. Baets, "Experimental demonstration of all-optical regeneration using an MMI-SOA," IEEE Photon. Technol. Lett. 14, 660-662 (2002).

[17] D. M. Marom, D. Panasenko, P.-C. Sun, Y. T. Mazurenko, Y. Fainman, "Real-time spatial-temporal signal processing with optical nonlinearities," IEEE J. Sel. Topics in Quantum Electron. 7, 683-693 (2001).

[18] G. P. Agrawal and N. A. Olsson, "Self-Phase Modulation and Spectral Broadening of Optical Pulses in Semiconductor Laser Amplifiers," IEEE J. Quantum Electron. 25, 2297-2306 (1989).

[19] R.W. Boyd, *Nonlinear Optics* (Academic Press, San Diego, CA, 1992).

[20] G.P. Agrawal, *Nonlinear Fiber Optics* (Academic Press, San Diego, CA, 1995).

[21] S.-Y. Tseng, W. Cao, L. Lucas, Y. Kim, V. Yun, Y. Leng, C. H. Lee, W. N. Herman, and J. Goldhar "A Technique for Measuring Complex $\chi^{(3)}$ Using DFWM with an Imaged 2-D Phase Grating," to appear in *Conference on Lasers and Electrooptics on CD-ROM* (The Optical Society of America, Washington, DC, 2006), CThQ3.

[22] J. W. Goodman, *Introduction to Fourier Optics* (McGraw-Hill, New York, 1996).

[23] T. Jannson, "Information capacity of Bragg holograms in planar optics," J. Opt. Soc. Am. 71, 342-347 (1981).

[24] M. E. Marhic, "Discrete Fourier transforms by single-mode star networks," Opt. Lett. 12, 63-65 (1987).

[25] A. E. Siegman, "Fiber Fourier optics," Opt. Lett. 26, 1215-1217 (2001).

[26] A. R. Gupta, K. Tsutsumi, and J. Nakayama, "Synthesis of Hadamard transformers by use of multimode interference optical waveguides," Appl. Opt. 15, 2730-2738 (2003).

[27] M. Reck and A. Zeilinger, "Experimental Realization of Any Discrete Unitary Operator," Phys. Rev. Lett. 73, 58-61 (1994).

[28] D. J. Brady and D. Psaltis, "Holographic interconnections in photorefractive waveguides," Appl. Opt. 30, 2324-2333 (1991).

[29] T. Morioka, K. Mori, and M. Saruwatari, "Ultrafast polarisation-independent optical demultiplexer using optical carrier frequency shift through crossphase modulation," Electron. Lett. 28, 1070-1072 (1992).

[30] B.-E. Olsson and D. J. Blumenthal, "All-Optical Demultiplexing Using Fiber Cross-Phase Modulation (XPM) and Optical Filtering," IEEE Photon. Technol. Lett.,13, 875877 (2001).

[31] R. Salem, A. M. Lenihan, G. M. Carter and T. E. Murphy, "80 Gb/s Polarization-Independent Optical Demultiplexing in Highly Nonlinear Bismuth-Oxide Fiber," to appear in *Conference on Lasers and Electrooptics on CD-ROM* (The Optical Society of America, Washington, DC, 2006), CMT3.

[32] G. M. Carter, "Excited state dynamics and temporally resolved nonresonant nonlinear-optical processes in polydiacetylene," J. Opt. Soc. Am. B 4, 1018-1024 (1987).

[33] H.-Y. Yu, D. Mahgerefteh, P. S. Cho, and J. Goldhar, "Optimization of the frequency response of a semiconductor optical amplifier wavelength converter using a fiber Bragg grating," J. Lightwave Technol. 17, 308-315 (1999).

[34] S. Nakamura and K. Tajima, "Ultrafast all-optical gate switch based on frequency shift accompanied by semiconductor band-filling effect," Appl. Phys. Lett. 70, 3498-3500 (1997).

[35] M. L. Nielsen and J. Mørk "Increasing the modulation bandwidth of semiconductor-optical-amplifier-based switches by using optical filtering," J. Opt. Soc. Am. B. 21, 1606-1619 (2004).

[36] Y. Liu, E. Tangdiongga, Z. Li, S, Zhang, H. de Waardt, G. D. Khoe, and H. J. S. Dorren, "Error-Free All-Optical Wavelength Conversion at 160 Gb/s Using a Semiconductor Optical Amplifier and an Optical Bandpass Filter," J. Lightwave Technol. 24, 230-236 (2006).

[37] A. Yariv, "Coupled-Mode Theory for Guided-Wave Optics," IEEE J. Quantum Electron. 9, 919-933 (1973).

[38] L. B. Soldano and E. C. M. Pennings, "Optical Multi-Mode Interference Devices Based on Self-Imaging: Principles and Applications," J. Lightwave Technol. 13, 615-627 (1995).

[39] K. Kawano and T. Kiton, *Introduction to Optical Waveguide Analysis* (Wiley, New York, 2001).

[40] B. E. A. Saleh and M. C. Teich, *Fundamentals of Photonics* (Wiley, New York, 1991).

[41] H. F. Talbot, "Facts relating to optical science. No IV," Philos. Mag. 9, 401-407 (1836).

[42] M. Bachmann, P. A. Besse, and H. Melchior, "General self-imaging properties in $N \times N$ multi-mode interference couplers including phase relations," Appl. Opt. 33, 3905-3911 (1994).

[43] J. M. Heaton, R. M. Jenkins, D. R. Wright, J. T. Parker, J. C. H. Birbeck, and K. P. Hilton, "Novel 1-to$N$ way integrated optical beam splitters using symmetric mode mixing in GaAs/AlGaAs multimode waveguides," Appl. Phys. Lett. 61, 1754-1756 (1992).

[44] P. A. Besse, E. Gini, M. Bachmann, and H. Melchior, "New 2×2 and 1×3 Multimode Interference Couplers with Free Selection of Power Splitting Ratios," J. Lightwave Technol. 14, 2286-2293 (1996).

[45] T. E. Murphy, *Optical mode solver*. Retrieved June 04, 2004, from http://www.photonics.umd.edu/software/index.html

[46] J. M. Heaton and R. M. Jenkins, "General Matrix Theory of Self-Imaging in Multimode Interference (MMI) couplers," IEEE Photon. Technol. Lett. 11, 212-214 (1999).

[47] Y. Chung and N. Dagli, "An Assessment of Finite Difference Beam Propagation Method," IEEE J. Quantum Electron. 26, 1335-1339 (1990).

[48] G. R. Hadley, "Wide-angle beam propagation using Pade approximant operators," Opt. Lett 17, 1426-1428 (1992).

[49] G. R. Hadley, "Multistep method for wide-angle beam propagation," Opt. Lett 17, 1743-1745 (1992).

[50] B.-T. Lee and S.-Y. Shin, "Mode-order converter in a multimode waveguide," Opt. Lett. 28, 1660-1662 (2003).

[51] O. Moriwaki, T. Kitoh, T. Sakamoto, and A. Okada, "Novel PLC-Based Optical Correlator for Multiple Phase-Mudulated Labels," IEEE Photon. Technol. Lett. 17, 489-491 (2005).

[52] A. Yariv, *Optical Electronics in Modern Communications* (Oxford, New York, 1997).

[53] A. M. Vengsarker, P. J. Lemaire, J. B. Judkins, V. Bhatia, T. Erdogan, and J. E. Sipe, "Long-Period Fiber Gratings as Band-Rejection Filters," J. Lightwave Technol. 14, 58-65 (1996).

[54] T. Erdogan, "Cladding-mode resonances in short- and long- period fiber grating filters," J. Opt. Soc. Am. A 14, 1760-1773 (1997).

[55] P. A. Besse, M. Bachmann, H. Nelchior, L. B. Soldano, and M. K. Smit, "Optical Bandwidth and Fabrication Tolerances of Multimode Interference Couplers," J. Lightwave Technol. 12, 1004-1009 (1994).

[56] G. Keiser, *Optical Fiber Communications* (McGraw-Hill, Boston, 2000).

[57] M. Sheik-Bahae, A. A. Said, T.-H. Wei, D. J. Hagan, and E. W. Van Stryland, "Sensitive measurement of optical nonlinearities using a single beam," IEEE J. Quantum Electron. 26, 760-769 (1990).

[58] F. P. Strohkendl, L. R. Dalton, R. W. Hellwarth, H. W. Sarkas, and Z. H. Kafafi, "Phase-mismatched degenerate four-wave mixing: complex third-order susceptibility tensor elements of C_{60} at 768nm," J. Opt. Soc. Am. B. 14, 92-98 (1997).

[59] J. A. Shirley, R. J. Hall, and A. C. Eckbreth, "Folded BOXCARS for rotational Raman studies," Opt. Lett. 5, 380-382 (1980).

[60] H. J. Eichler, P. Gnter, and D. W. Pohl, *Laser-induced dynamic gratings* (Springer-Verlag 1986).

[61] A. A. Maznev, K. A. Nelson, and J. A. Rogers, "Optical heterodyne detection of laser- induced gratings," Opt. Lett. 23, 1319-1321 (1998).

[62] G. D. Goodno, G. Dadusc, and R. J. D. Miller, "Ultrafast heterodyne-detected transient-grating spectroscopy using diffractive optics," J. Opt. Soc. Am. B 15, 1791-1794 (1998).

[63] Q.-H. Xu, Y.-Z. Ma, I. V. Stiopkin, and G. R. Fleming, "Wavelength-dependent resonant homodyne and heterodyne transient grating spectroscopy with a diffractive optics method: solvent effect on the third-order signal," J. Chem. Phys. 116, 9333-9340 (2002).

[64] D. Milam, "Review and assessments of measured values of the nonlinear refractive-index coefficient of fused silica," Appl. Opt. 37, 546-550 (1998).

[65] T. Kato, Y. Suetsugu, N. Takagi, E. Sasaoka, and M. Nishimura, "Measurement of the nonlinear refractive index in optical fiber by the croo-phase-modulation method with depolarized pump light," Opt. Lett. 20, 988-990 (1995).

[66] W. N. Herman and M. J. Roberts, "The sense of chromophore orientation in films made by alternating polyelectrolyte deposition," Adv. Mater. 13, 744-746 (2001).

[67] M. Samoc, A. Samoc, B. Luther-Davies, Z. Bao, L. Yu, B. Hsieh, and U. Scherf, "Femtosecond Z-scan and degenerate four-wave mixing measurements of real and imaginary parts of the third-order nonlinearity of soluble conjugated polymers," J. Opt. Soc. Am. B 15, 817-825 (1998).

[68] D. Marcenac and A. Mecozzi, "Switches and Frequency Converters Based on Cross-Gain Modulation in Semiconductor Optical Amplifiers," IEEE Photon. Technol. Lett. 9, 749-75 (1997).

[69] N. Calabretta, Y. Liu, F. M. Huijskens, M. T. Hill, H. de Waardt, G. D. Khoe, and H. J. S. Dorren, "Optical Signal Processing Based on Self-Induced Polar-

ization Rotation in a Semiconductor Optical Amplifier," J. Lightwave Technol. 22, 372-381 (2004).

[70] Y. Ueno, S. Nakamura, and K. Tajima, "Nonlinear phase shifts induced by semiconductor optical amplifiers with control pulses at repetition frequencies in the 40-160-GHz grange for use in ultrahigh-speed all-optical signal processing," J. Opt. Soc. Am. B 19, 2573-2589 (2002).

[71] J. Mørk and A. Mecozzi, "Theory of the ultrafast optical response of active semiconductor waveguides," J. Opt. Soc. Am. B 13, 1803-1816 (1996).

[72] A. Siegman, *Lasers* (University Science Books, Sausalito, 1986).

[73] L. M. Zhang, S. F. Yu, M. C. Nowell, D. D. Marcenac, J. E. Carrol, and R. G. S. Plumb, "Dynamic Analysis of Radiation and Side-Mode Suppression in a Second-Order DFB Laser Using Time-Domain Large-Signal Travelling Wave Model," IEEE J. Quantum Electron. 30, 1389-1395 (1994).

[74] S. S. Nayak and P. K. Meher, "High Throughput VLSI Implementation of Discrete Orthogonal Transforms Using Bit-Level Vector-Matrix Multiplier," IEEE Trans. Circuits Syst. , 46, 655-658 (1999).

[75] A. Aslam-Siddiqi, W. Brockherde, and B. J. Hosticka, "A 16 $\times$ 16 Nonvolatile Programmable Analog Vector-Matrix Multiplier," IEEE J. Solid-State Circuits, 33, 1502-1509 (1998).

[76] H. Wei, J. Yu, Z. Liu, X. Zhang, W. Shi, and C. Fang, "Signal Bandwidth of General N × N Multimode Interference Couplers," J. Lightwave Technol. 19, 739-745 (2001).